Università degli Studi di Napoli *Federico II*

DOTTORATO DI RICERCA IN FISICA

Ciclo 35°

Coordinatore: Prof. Vincenzo Canale

Laser induced periodic surface structures: influence of materials and processing conditions

Settore Scientifico Disciplinare FIS/01

Dottorando
Meilin Hu

Tutore
Prof. Salvatore Amoruso
Dr. Jijil JJ Nivas

Anni 2019 / 2022

Introduction

The research on the micro-nano structures formed on the surface of a target irradiated by laser beams has been an evergreen scientific topic. Research on the micro-nano structures formed on a laser-irradiated target has been a topic of constant interest for the past few decades. The non-contact nature of laser processing along with its high energy localization make it widely applicable to manufacturing, tribology, biomedicine, chemistry, as well as several other disciplines.

After T. H. Maiman *et al*. made the breakthrough with the first pulsed laser in 1960, laser technology continued to develop rapidly, strengthening the field of laser materials processing. In the last decades, interest in laser-solid irradiation has gradually shifted toward ultrashort light pulses. Due to the ultrashort duration, femtosecond (fs) lasers pulses have the ability to induce a considerably less heat-affected zone, which in turn provides a greater spatial resolution in material processing. This makes the fs laser a precise and versatile tool for micro- and nano-fabrication. Since many surface properties of solids are closely related to their morphology, the possibility to modify and tailor the material surface can have a great impact on various features, such as the optical, wetting, mechanical responses, etc. Further applications of laser processing include the creation of microfluidic channels for biological applications and optical integrated circuits for quantum applications.

The formation of laser-induced periodic surface structures (LIPSS) is a phenomenon that is almost ubiquitous to any material. The aim of this work is to experimentally analyze the role of various processing parameters (e.g. laser repetition rate, wavelength, scanning speed, etc.) taking also into account the materials properties by selecting few different targets. In this thesis, the LIPSS generated on various targets like silicon, copper, semiconductive films and topological insulators are investigated by a combination of different microscopy characterization techniques (i.e. Optical Microscopy, Scanning Electron Microscopy, Atomic Force Microscopy) and image processing analyses (*ImageJ, Gwyddion*) in different experimental configurations such as static spots, dynamic lines as well as large areas processing. We found that the morphological characteristics of LIPSS can be controlled by the influence of various experimental parameters, e.g., laser pulse wavelength, fluence, pulse repetition rate, beam or target scanning speed, processing ambient, etc. The characteristics can be illustrated by the periods and shapes of the ripples, and the strength of the nanoparticles.

This thesis is composed of six chapters. Chapter 1 mainly introduces the characteristics of LIPSS, related applications and generation mechanisms, which provide a theoretical basis for the research in the subsequent chapters. In Chapter 2, the laser systems used and the image processing methods are reported in detail. The description of circular and elliptical craters generated by focusing Gaussian beams with different lenses is also theoretically analyzed. The specific study of fs laser surface properties on silicon targets is presented in Chapter 3. First, we find that in the dynamic configuration, the scanning speed and laser pulse energy have a great influence on the properties of subwavelength ripples. We also compare laser ablation of silicon samples in air and vacuum at high repetition rates, addressing the very interesting aspect that the influence of plume shielding is negligible in vacuum but becomes important in air at repetition rates larger than about 10 kHz. Large-area irradiation of copper is presented in Chapter 4, where the ripples generated at different laser intensities are analyzed in detail. The different zones of the spatial distribution of the laser intensity will have a different degree of overlap of the Gaussian laser intensity distribution, resulting in different morphological characteristics in each zone. We report in Chapter 5 that the ripples orientation follows the local direction of the laser polarization in a semiconductor polymer PH3T and a fullerene derivative $PC_{71}BM$. Chapter 6 mainly summarizes the formation of periodic ripples on a topological insulator, Bi_2Te_3, induced by fs laser ablation.

This work is devoted to the morphological characterization of laser-induced surface structures on various types of materials with different laser parameters. These challenging studies provide valuable and interesting results that contribute to a deeper understanding and greater control of laser-induced surface structures.

Contents

Chapter 1

Laser-induced periodic surface structures

Laser-induced periodic surface structures (LIPSS) are formed during the interaction between laser pulses and a solid sample surface. The exploitation of ultrashort laser pulses leads to the generation of special micro-nano structures on any material with a spatial period below the laser light wavelength. The typical length of LIPSS can be several micrometers, but surface structures with sizes as low as 100 nm can also be formed. Moreover, the specific orientation of the surface structures depends on the laser polarization and material properties. This chapter briefly illustrates the classical theory of LIPSS formation, and the mechanisms involved. The LIPSS are typically visualized by scanning electron microscopy (SEM) analysis and some examples will be shown hereafter. Finally, some typical applications of LIPSS in the fields of surface structure coloration and water wetting response are illustrated.

1.1 Introduction

In the past years, the research on the effects of ultra-short laser pulses on materials has been a hot topic, thanks to the advantages of minimal thermal effect and capability of processing almost any solid material. The generation of LIPSS, generally termed as ripples, is a common phenomenon that occurs in almost any solid material exposed to strong linearly polarized coherent electromagnetic radiation [1]. The first observation that regular structures form on the surface of a Ge target irradiated by laser radiation was reported by Birnbaum very early after the invention of the ruby laser [2]. Since then, the formation of self-organized LIPSS represents an interesting physical process and the mechanisms involved in their generation are still actively discussed and under investigation [3-7], especially for femtosecond (fs) laser pulse irradiation. The classical theory of LIPSS formation considers their generation as the result of the interaction between incident light and surface scattered waves [8-9].

The typical length of LIPSS can be several micrometers, but surface structures with sizes as low as 100 nm can also be formed. Moreover, the specific orientation of the surface structures depends on the laser polarization. LIPSS are generally classified according to their spatial period, Λ, at normal incidence, as Low Spatial Frequency LIPSS (LSFL) for $\lambda/2 <$

$\Lambda < \lambda$ and High Spatial Frequency LIPSS (HSFL) for $\Lambda < \lambda/2$ [3,10,11], where λ is the laser wavelength. The specific classification of LIPSS is as follows:

• LSFL ($\lambda/2 < \Lambda < \lambda$).

1. LSFL-I: These structures are typical for metals and semiconductors and are characterized by $\Lambda_{\mathrm{LSFL}} \sim \lambda$ and orientated perpendicular to the laser beam polarization.

2. LSFL-II: These structures are typical for materials with large band gap and are characterized by $\Lambda_{\mathrm{LSFL}} \sim \lambda/n$, with n being the refractive index of the material, and are usually orientated parallel to the laser beam polarization [3,11].

• HSFL ($\Lambda < \lambda/2$), with A as the depth-to-period aspect ratio.

1. HSFL-I: with A > 1, typically observed for semiconductors and dielectrics;

2. HSFL-II: with A < 1, typically observed for metals [11].

In addition to subwavelength ripples, the formation of ordered surface structures characterized by a supra-wavelength period, not yet included in the previous classification and generally indicated as "grooves", has been also observed on different materials and remains still less investigated than more standard LIPSS [12]. The laser irradiation can easily induce the morphological structures of subwavelength ripples that show many potential applications, like surface coloring [13], light enhancement of light-emitting diodes [14] and hydrophobic behavior of the material surfaces [15].

The chapter is organized as follows: sections 1.2 and 1.3 present the different features of LIPSS, whereas section 1.4 briefly discusses some typical applications. Finally, section 1.5 illustrates the mechanisms underlying the LIPSS formation.

1.2 Characteristics of LIPSS

LIPSS show nanoscale characteristic features and microscale periodic surface patterns, which make them very interesting for applications. Some examples of LIPSS formed on steel (100Cr6, 1.3505) by fs laser irradiation are displayed in Fig. 1.1. Besides the LSFL characterized by a period close to the wavelength of the laser light, in 1994 Heitz *et al.* observed a new LIPSS-excited structure with a period much smaller than the laser wavelength, i.e. HSFL [16], also called deep sub-wavelength grating [17], that only forms when the target surface is irradiated by ultrashort laser pulses. An example of these HSFL is shown in Fig.

1.1(a), in which the ripples are oriented preferentially along the laser polarization and display a period of 160 nm. In contrast to the HSFL, the typical LSFL ripples shown in Fig. 1.1(b), present an orientation that is generally perpendicular to the polarization of the laser beam.

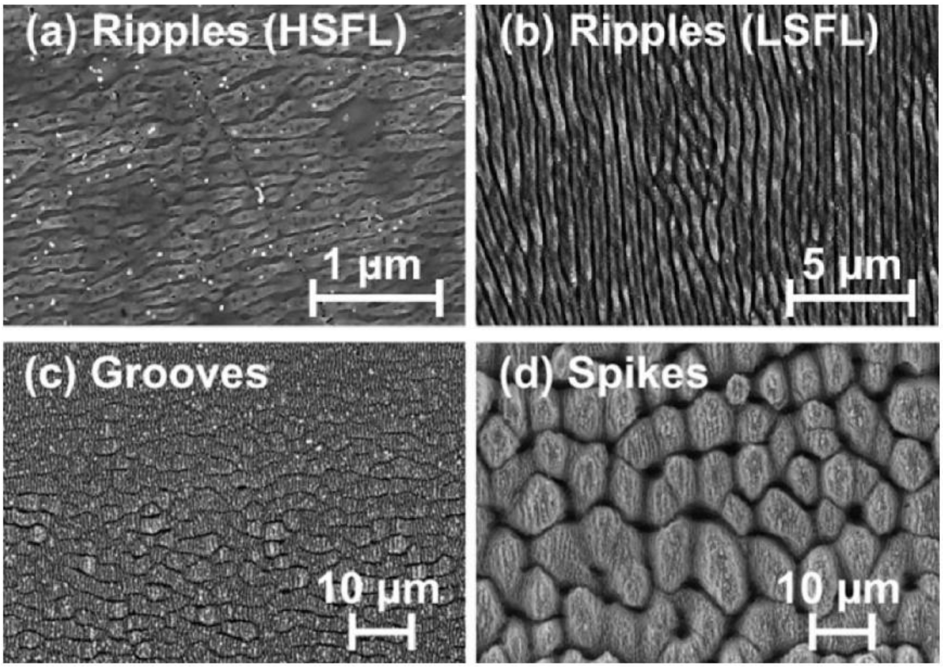

Fig. 1.1 Top-view scanning electron micrographs of characteristic surface morphologies [(a) ripples (HSFL); (b) ripples (LSFL); (c) grooves; (d) spikes] formed on alloyed steel (100Cr6, 1.3505) surfaces upon fs-laser processing in air at different irradiation parameters [λ=790 nm, τ=30 fs, f= 1 kHz]; (a) F_p= 0.25 J/cm^2, N_{eff}= 20; (b) F_p= 0.5 J/cm^2, N_{eff} = 40; (c) F_p = 2.5 J/cm^2, N_{eff} = 100; (d) F_p= 3.0 J/cm^2, N_{eff} =400]. Note the different magnifications used. The scan direction and the laser beam polarization are both horizontal. (Cited from Bonse *et al.* 2018 [18])

In addition to ripples, other surface microstructures, such as grooves (panel (c)) and spikes (panel (d)), can be observed in Fig. 1.1 [19]. The grooves are usually parallel to the polarization direction and display a supra-wavelength period of a few micrometers, while the spikes are more irregular, with a typical period of a few micrometers and a weaker correlation with the laser beam polarization. The LIPSS features depend on various processing parameters, the peak fluence, F_p, and the number of laser pulses, N, being the most important. In fact, they can determine the type of LIPSS (HSFL or LSFL) and influence the value of their spatial period. In both LSFL and HSFL, laser polarization and wavelength, λ, are other key parameters for the spatial arrangement of the surface structures, controlling their period and spatial orientation. Furthermore, the processing environment, e.g. air [20], vacuum [21] or liquid [22] ambient, can also play a significant role in defining the generation of LIPSS and their characteristics.

An interesting aspect of LIPSS resides in the possibility of extending their formation to large portions of the target surface by suitably moving the laser beam or the sample [23-25], which is particularly relevant for industrial demands of laser processing over large area. Hence, two typical experimental conditions exist for the generation and characterization of the features of the LIPSS. In the first one, static irradiation is used to generate a spot on the target surface decorated with LIPSS; in the second case, the laser beam is moved at a fixed speed on the target in a dynamic configuration producing a line decorated with LIPSS. This last mode can be extended to a two-dimensional area by further scanning along a direction perpendicular to the line formed with a predefined hatch distance. In both configurations, the LIPSS are generated in a given range of the values of the experimental parameters, namely the laser pulse fluence and number of overlapped laser shots.

Example are shown in the bottom panels of Fig. 1.2 that report top-view SEM images of the surface of a silicon target (resistivity>200 Ω cm, thickness≈400 μm), irradiated in static and dynamic conditions by a laser beam with Gaussian spatial profile, a wavelength of λ=1030 nm and a pulse duration of ≈180 fs obtained in the course of this thesis work. The pulse energy is $E \sim 10\ \mu J$ and the beam waist is estimated to be $\omega_0 = (25 \pm 1)\ \mu m$. The corresponding peak fluence of the Gaussian beam is $F_p = \frac{2E}{\pi\omega_0^2}$ and the spatial distribution of the fluence is given by $F(r) = F_p \cdot e^{\frac{-2r^2}{\omega_0^2}}$, where r is the radial distance from the position of the peak. The circular crater in panel (a) was produced on a static target by a sequence of N=200 pulses, whereas the shallow line in panel (b) was generated on a scanning target moving at a velocity V_s=0.25 mm/s, for an effective number of pulses $N_{eff} = 2\omega_0 \frac{RR}{V_s} = 200$ (RR is the repetition rate and V_s, the scanning velocity).

From the experimental data, it is possible to estimate the threshold fluences for the formation of the crater and the generation of the grooves as depicted in Fig. 1.2. In panel (a) of Fig. 1.2, the horizontal lines at $F_{th-LIPSS}$, $F_{th-Grooves}$ and $F_{th-Spikes}$ identify the values of the laser threshold fluences for crater/ripples formation and for the transition to the other surface structures generated in the inner, high-fluence region. The concentric regions of surface structures covering the shallow crater are separated by a very thin annulus where ripples and rudiments of the surface structures of the central area coexist. In our experiments, we deal with ablative LIPSS formed as a consequence of material removal from the target surface. In such a case the threshold for ripples formation corresponds to that of the production of a shallow crater, whereas grooves are generated in the inner part at higher fluence being characterized by a larger threshold fluence.

Thus, the values of the threshold fluences can be estimated by considering the Gaussian spatial beam profile with a $1/e^2$ beam waist ω_0. Prior to such an analysis, the reliability of this assumption can be verified by measuring the radius r of the two regions as a function of the laser pulse energy, E, observing in all cases the expected dependence $r^2 = (\omega_0^2/2)\ln(E/E_{th})$, E_{th} being the threshold energy [18,19,26-28]. As can be seen from Fig. 1.2, the different surface structures (LIPSS, grooves, spikes) have different threshold fluences that can be estimated by the radius of the corresponding region observed in the SEM image and the Gaussian beam profile.

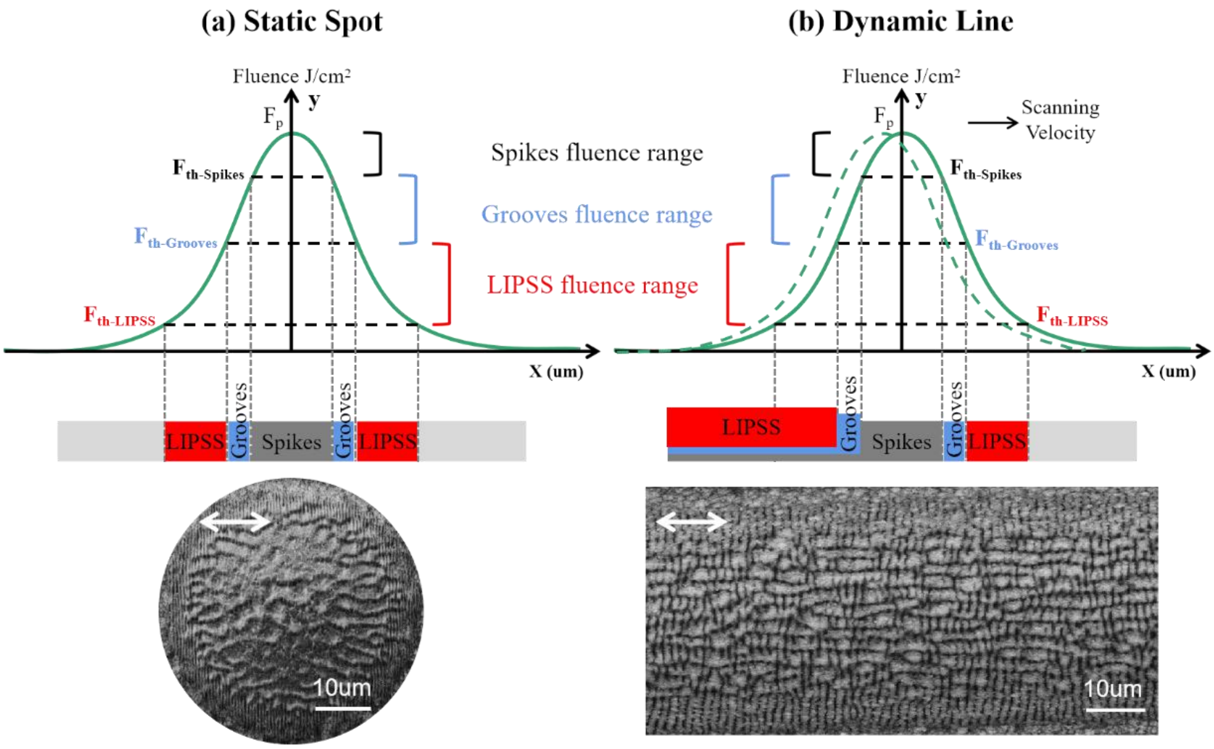

Fig. 1.2 Dependence of different surface morphologies (spikes, grooves and LIPSS) of static spot (a) and dynamic line (b) on different laser fluence under a spatial Gaussian femtosecond laser beam. The following two figures are the SEM images of the static spot (N=200, E=10 uJ, λ=1030 nm) and dynamic line (N_{eff}=100, V_s=0.25 mm/s, E=10 uJ, λ=1030 nm) of Silicon [100] target. The double-headed arrows illustrate the laser polarization direction.

Contrary to the static configuration, for the line scanning (panel (b)), each location of the surface is covered by an energy density that initially increases and subsequently decreases, and multiple exposures to the high-fluence portion of the central beam may result in the formation of spikes or grooves, creating layered micro/nano structures on the surface. Moreover, some differences in the finer morphological features of the grooves generated in the dynamic case are discernable in comparison to the static one. In fact, a more granular character of the grooves makes recognizable a clear pattern of underlying ripples, which is typical of grooves generated in the dynamic irradiation mode. Through scanning, the structure of these samples can exhibit specific surface properties, generating favorable drives for technology and life.

1.3 LIPSS in different materials

Fig. 1.3 shows SEM images of LIPSS generated on three different kinds of samples by laser irradiation, in air. One can observe a consistent deposition of nanoparticle debris due to the deposition on the sample surface of the ablated material induced by the confinement effect of the ambient atmospheric pressure. Panels (a) and (b) refer to shallow craters obtained by focusing the laser beam with a spherical lens (plano-convex lens), while panel (c) displays the long strip obtained by the laser beam after focusing with a cylindrical lens. One can observe that orientation of the ripples is all the same, because the direction of the laser polarization is horizontal in all three cases, inducing ripples directed along the vertical direction. Instead, the central region irradiated by the part of the beam at higher fluence displays coarser surface structures preferentially oriented along the direction parallel to the laser polarization, that are especially evident in the case of the silicon sample (Fig. 1.3 (a)).

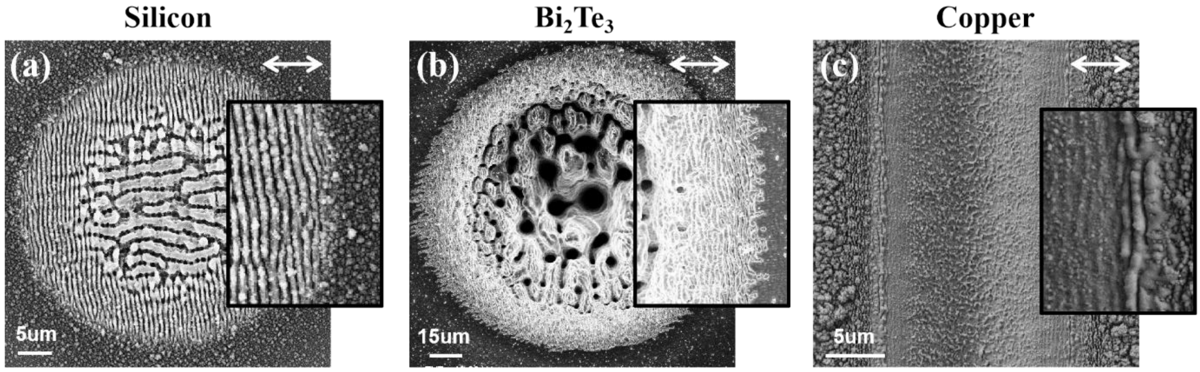

Fig. 1.3 SEM images of LIPSS on different materials. (a) LIPSS on Silicon [100] in air with $\lambda = 1050$nm, E=17μJ, N=200. (b) LIPSS on topological insulator (Bi_2Te_3) in air with λ=800 nm, N=500, E=60 μJ. (c) LIPSS on copper with cylindrical lens, λ=515 nm, RR=5 kHz, E=197 μJ and N=200. The insets show zoomed views of ripples surface modulation. The double headed arrows in the three panels mark the laser beam polarization direction.

1.4 Applications of LIPSS

LIPSS have broad application prospects in sensors, solar power generation, photocatalysis and has in-depth exploration in surface processing, optical response and machinery, because of its nano-scale characteristic structure and self-repeating micro-scale arrangement pattern.

Currently, the applications of LIPSS-covered surfaces have been extensively studied in various fields. Examples include controlled coloration induced by LIPSS diffraction, effect of LIPSS on biofilm growth [29], hydrophobic/hydrophilic behavior of sample surfaces [15], and applications to reduce friction and wear on material surfaces [30-32]. Most of these applications require uniform processing of LIPSS over a large surface area, which is usually accomplished by linearly scanning of a focused laser beam across the sample surface. To avoid thermal accumulation effects, sufficiently fast scanning techniques, such as high-energy ultrashort laser pulses with multiple MHz pulse repetition rates, have been developed on the market for the generation of micro-nano surface textures in industrial applications [33]. In terms of scanning speed, it can also be as high as 25 m/s to 90 m/s [11].

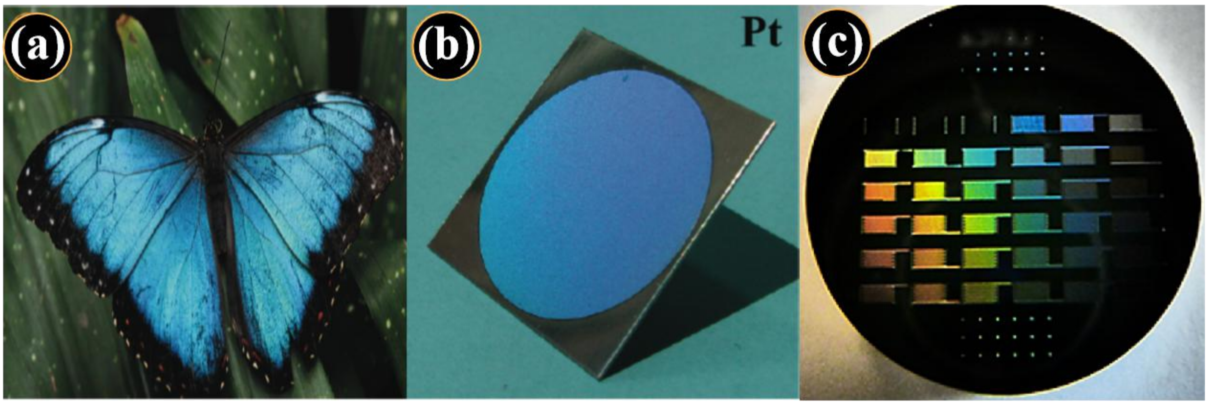

Fig. 1.4 Structural color by laser. (a) Colorful blue of butterfly wings due to periodic microstructures. (b) Colorful blue of platinum sample with LIPSS textured surface. (c) Different color presentation of steel samples (100Cr6) under different laser peak fluence F_p (30 fs, 800 nm,1 kHz) (Cited from Vorobyev *et al*. 2012 [13], Bonse *et al*. 2017 [11])

A promising application of LIPSS is their use as diffraction gratings to produce structural colors. A good example of how surface structures affect the color is represented by the butterfly wings (Fig. 1.4(a)) showing various iridescent colors that are not produced by pigments but are due to the interference and diffraction of light on complex periodic microstructures [13]. These kinds of colors can be also produced by the optical diffraction of ambient light on a LSFL. Since the fs laser can change the nano/micro structure of the sample surface, dye-free structure coloring can be realized, which is an effective method to obtain metal structure coloring [34-35].

Panel (b) of Fig. 1.4 displays a platinum sample with a laser-induced surface texture showing a blue iridescent color similar to the structure of butterfly wings, due to the surface micro-nano structures produced by the fs laser irradiation. Same with the butterfly wings, the color of LIPSS surface structure of metals exhibits distinct blue with different viewing angles. The presence of different structural colors on the steel surface with varying laser fluence and effective pulse number N_{eff} in reported in panel (c). The scanning speed, beam wavelength, laser fluence, and effective pulse number can eventually generate different surface structures giving rise to different colors.

As early as 2008, Vorobyev and Guo took the lead in using fs lasers to modify the optical properties of aluminum, gold and platinum [34]. Later, LIPSS induced structural colors on other different types of metals, such as steel [35-37] and copper [38-39], followed by the study of structural colors on semiconductors [40]. Dusser *et al*. also systematically studied the influence of critical laser parameters such as pulse energy, light polarization, and spot size on the sample ripples and the optical properties generated on the sample. With this colorimetric calibration, the nanostructure of the sample can be predefined so that the color of the samples can meet the needs of the users [41].

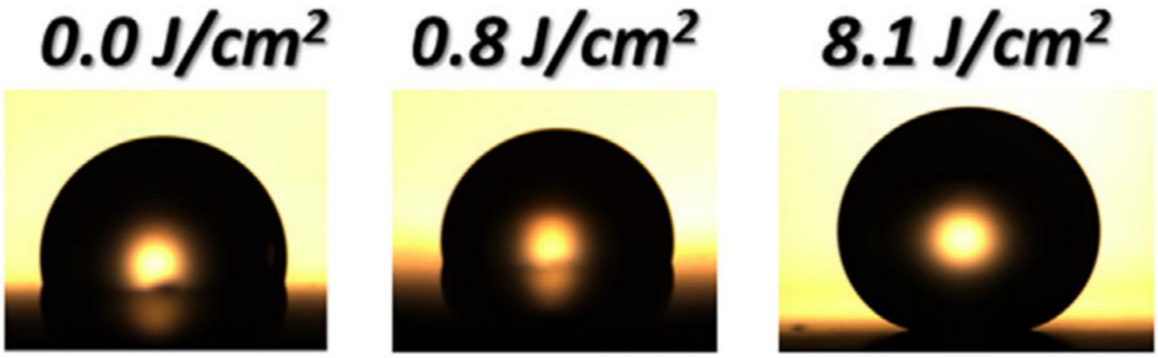

Fig.1.5 Photograph of water droplets on a copper surface at three different values of laser peak fluence. (Cited from Allahyari *et al*. 2019 [15])

The wetting response of a surface is another interesting application. The water wetting response is decided by the contact angle of the water droplet with the material. If the contact angle is less than 90 degrees, the material is hydrophilic, which means that water easily wets the surface, whereas if the contact angle is greater than 90 degrees, the material is hydrophobic, which means that water cannot wet the material, so it stays like drop, making minimum contact area with the material. As an example, Fig. 1.5 shows the wetting response of copper samples. In fact, it can be seen that the increase of the laser fluence induces an increment of the water contact angle. This indicates that the surface texture produced by the laser affects the surface wettability of the copper samples [15,42]. Therefore, laser surface structuring can enhance wetting characteristics of the material making it super-hydrophobic or super-hydrophilic.

1.5 Mechanisms of LIPSS formation

Because of the difference in the temporal regime within which LIPSS are formed, two theoretical mechanisms are considered by the current scientific community:

• **Electromagnetic theories**: the generation of LIPSS is directly related to the deposition of light energy into solids during laser irradiation; the light absorption and the formation of LIPSS are studied using double fs pulses [3,43].

• **Matter reorganization theories**: LIPSS form after laser irradiation (from hundred of ps to tens of ms) and this may involve hydrodynamic effects along with material instabilities, erosion effects and creation of defects; time-resolved spectroscopy (e.g. pump-probe) is used to study the ultra-fast dynamics of the LIPSS [11].

1.5.1 Electromagnetic theories

1.5.1.1 SPP model

LSFL is believed to be formed under conditions of high laser fluence and few pulses. Currently, the most accepted mechanism for the formation of LSFL-I is the interference of the incident laser beam with surface electromagnetic wave (SEW) generated on the rough surface [43-44]. Initially, we can imagine that the incident, linearly polarized laser beam generates a defect on the material, which acts as a scattering center. Consequently, a wave propagating along the surface through scattering effects is produced. This wave, known as SEW, interacts in turn with the incident laser beam and creates an interference pattern which modulates the spatial energy distribution deposited onto the sample.

In order to explain the formation of LSFL under the condition of high laser fluence and low number of pulses, some researchers proposed the surface plasmon polariton (SPP) theory. For example, in 2009, Huang *et al*. systematically described the generation and principle of the surface periodic structure [17], considering the effect of SPP, the periodic structure was transferred from the scattering model to the effect of plasma.

The process of fs laser-induced photoionization providing free carrier changes to the dielectric function is equivalent to instantaneous doping. Therefore, it is possible for incident light to couple with surface plasmons. The SPP theory points out that the polarized wave of propagating surface plasmon and the incident laser interfere at the silicon-dielectric interface, forming a ripple periodicity on the silicon surface in a highly excited state.

Taking the example of ablating a sample of metal in air, their permittivities meet specific conditions that [53]:

$$\mathrm{Re}\{\epsilon_{\mathrm{air}}\}\mathrm{Re}\{\epsilon_{\mathrm{sample}}\} <- \mathrm{Im}\{\epsilon_{\mathrm{air}}\}\mathrm{Im}\{\epsilon_{\mathrm{sample}}\}. \tag{1}$$

The SPPs are excited if the dielectric permittivity $\epsilon_{\mathrm{metal}}$ reaches the condition:

$$\mathrm{Re}\{\epsilon_{\mathrm{metal}}\} <-1. \tag{2}$$

Referring to the SPP standard model of LIPSS, the spatial period of LSFL-I $\Lambda_{\mathrm{LSFL-I}}$ is linked to the spatial period of the modulated electromagnetic field Λ_{SPP} through the relation reported in Eq. (3) for a plane air-metal interface,

$$\Lambda_{\mathrm{LSFL-I}} = \Lambda_{\mathrm{SPP}} = \lambda \mathrm{Re}\left\{\sqrt{\frac{\epsilon_{\mathrm{metal}}+1}{\epsilon_{\mathrm{metal}}}}\right\}, \tag{3}$$

where λ is the wavelength of laser radiation, which is valid for experiments employing few pulses and for not too deep LIPSS relief [3,45].

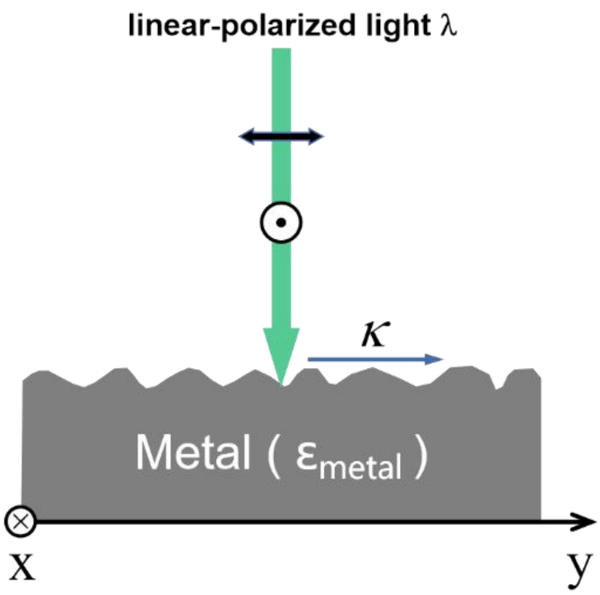

Fig. 1.6 Geometry of the laser beam incidence to a rough metal surface with linear polarized laser at the surface wave vector κ and wavelength λ.

Fig. 1.6 is the schematic diagram of the laser beam incidence to a rough metal surface with linearly polarized laser light. Let us assume that the surface of the x-y plane is exposed to fs laser pulses in air environment. As mentioned, if the condition in Eq. (2) is satisfied, SPPs excitation can occur [54]. Hence SPPs waves propagate along the surface of the material with a wave number given by

$$k = \pm \frac{\omega}{c}\sqrt{\frac{\epsilon_{air}\epsilon_{metal}}{\epsilon_{air}+\epsilon_{metal}}}, \tag{4}$$

where ω is the angular frequency of the waves. Since SPPs spread across the metal surface, some energy could be lost due to the absorption. From this point of view, a parameter which takes into account these absorption phenomena is introduced: the propagation length (or mean free path) L_{SPP}. L_{SPP} is defined as the distance beyond which SPPs intensity decays by a factor equal to 1/e, and it is calculated as follow:

$$L_{SPP} = \frac{1}{2\mathrm{Im}\{k\}}. \tag{5}$$

From the above equation one can prove that the mean free path L_{SPP} of metal is related to the regularity of periodic structure. Then we can make the following classification [55]:

1. Metals with L_{SPP} ranging from 0.05 μm which manifest high regular periodic structures (HR-LIPSS);

2. Metals with $L_{SPP} \gtrsim 50$ μm for which periodic structures appear in a not so regular way.

1.5.1.2 Sipe-Drude theory

At present, it is largely believed that the most acceptable model to explain the formation mechanism of LIPSS features is the surface scattering wave model, which comes from the research of Sipe *et al.* [46]. In recent years, the Sipe-Drude method has been used to explain the fine morphological structures of ripples and grooves produced by fs laser irradiation of silicon surfaces with Gaussian intensity distribution, such as bending and crossing phenomena [54]. Considering the influence of the change of dielectric constant ε_{metal} induced by fs laser irradiation on the metal surface, the LSFL-II is formed on the rough metal surface due to the inhomogeneous deposition of energy caused by the coupling of incident beams and surface waves. It is worth mentioning that the silicon surface irradiated by intense ultrashort laser pulses suddenly transits into a metallic state.

The Sipe-Drude theory expounds the formation mechanism of the LIPSS on the silicon surface excited by fs lasers pulses, which is based on the interference theory between incident light and the electromagnetic field scattered by the surface. Namely, the scattering of fs laser light wave on surface defect or surface roughness forms non-resonant excitation. Therefore, uneven absorption under the rough surface of the material leads to the formation of LIPSS.

The advantage of Sipe theory is the ability to predict inhomogeneous energy deposition on the silicon surface in the spatial frequency domain, which is further quantified by a scalar function called the efficacy factor η (where $\eta(k)$ is the efficacy factor at the spatial frequency k of inhomogeneous energy deposition caused by the surface roughness), b(k) represents the Fourier amplitude component of the surface roughness at k position. Thus, the mathematical expression of Sipe theory is $\eta(k)|b(k)|$. Since b(k) is a slow-changing function, being negligible, the local maximum at k determines the periodicity of the LIPSS.

1.5.2 Matter reorganization theory

The theory of matter reorganization is another of the most widely accepted thoughts in the scientific community besides electromagnetic theories. After being irradiated by an ultrafast laser pulse, the material exhibits a molten phase, which then cools and solidifies. During this process, transport effects occur and cause the material to redistribute, remodeling in periodic structural patterns. A range of theories consistent with the above events, such as hydrodynamic effects [47], material instability [48], and microscopic packing [49], has been proposed. Here, we briefly discuss two of these theories: the theory of fluid mechanics [50,51] and the theory of self-organization [52].

1.5.2.1 Hydrodynamic theory

The hydrodynamic theory mainly involves the effect of a gradient of surface tension to stretch the molten layer into a solid state during the transition phase. Navier-stokes equations [50-51] are usually used to deal with the dynamics of the molten layer:

$$\frac{\partial u}{\partial t} - \nu \Delta u + (u \cdot \nabla) u + \nabla p = f. \tag{6}$$

It describes the motion of a continuous fluid with volume force f with pressure p and dynamic viscosity u. In this case, the possible participation of thermo-elastically generated surface acoustic waves (SAWs) and capillary waves cannot be ignored. In particular, when the absorbed energy is deposited in a thin layer of the material and the SAW is excited at the appropriate spatial frequency with the contribution of the heat flow, it appears as a result of the capillary force during the convective motion of the fluid (Marangoni effect [3]).

1.5.2.2 Self-organization theory

The theory of self-organization is based on the formation of defects (vacancies, displacements, voids) after intense fs laser irradiation. These defects are trapped in a layer of thickness h of the host material, causing it to become unstable, manifesting as thermal nonequilibrium. Therefore, a mechanism to restore thermal equilibrium is required. This fact leads to the temporal evolution of the elastic thin layer h and leads to self-assembled quasi-periodic structures [52].

1.6 Conclusions

In summary, we mainly illustrated the basic characteristics of LIPSS and their current classification. The effect of the laser fluence spatial distribution on the location of the surface structures and the corresponding threshold fluence for their formation were illustrated for the static spot and dynamic line configurations. Moreover, examples of the LIPSS generated on various materials and for different laser beam focusing conditions (e.g. spherical and cylindrical lenses) were also illustrated. Some examples of the functional features imparted to the material such as structural colors and wetting response were also briefly discussed to evidence the wide interest for applications. Finally, the current theoretical interpretations of the mechanisms of LIPSS formation were briefly addressed.

Bibliography

[1] H. M. van Driel, J. E. Sipe, J. F. Young. Laser-induced periodic surface structure on solids: a universal phenomenon. Phys. Rev. Lett. 49 (1982) 1955. https://doi.org/10.1103/PhysRevLett.49.1955.

[2] M. Birnbaum. Semiconductor Surface Damage Produced by Ruby Lasers. J. Appl. Phys. 35 (1965) 3688-3689. https://doi.org/10.1063/1.1703071.

[3] J. Bonse, S. Gräf. Maxwell Meets Marangoni—A Review of Theories on Laser-Induced Periodic Surface Structures. Laser Photonics Rev. 14 (2020) 2000215. https://doi.org/10.1002/lpor.202000215.

[4] J. Bonse, S. Gräf. Ten Open Questions about Laser-Induced Periodic Surface Structures. Nanomaterials 11 (2021) 3326. https://doi.org/10.3390/nano11123326.

[5] D. Zhang, X. Li, Y. Fu, Q. Yao, Z. Li, K. Sugioka. Liquid vortexes and flows induced by femtosecond laser ablation in liquid governing formation of circular and crisscross LIPSS. Opto-Electronic Advances 5 (2022) 210061-210066. https://doi.org/10.29026/oea.2022.210066.

[6] D. Zhang, B. Ranjan, T. Tanaka, K. Sugioka. Carbonized Hybrid Micro/Nanostructured Metasurfaces Produced by Femtosecond Laser Ablation in Organic Solvents for Biomimetic Antireflective Surfaces. ACS Appl. Nano Mater. 3 (2020) 1855-1871. https://doi.org/10.1021/acsanm.9b02520.

[7] D. Zhang, R. Liu, Z. Li. Irregular LIPSS produced on metals by single linearly polarized femtosecond laser. Int. J. Extrem. Manuf. 4 (2021) 15102. https://doi.org/10.1088/2631-7990/ac376c.

[8] J. E. Sipe, J. F. Young, J. S. Preston, H. M. van Driel. Laser-induced periodic surface structure. I. Theory. Phys. Rev. B 27 (1983) 1141-1154. https://doi.org/10.1103/PhysRevB.27.1141.

[9] J. Bonse, J. Krüger. Pulse number dependence of laser-induced periodic surface structures for femtosecond laser irradiation of silicon. J. Appl. Phys. 108 (2010) 34903. https://doi.org/10.1063/1.3456501.

[10] D. Dufft, A. Rosenfeld, S. K. Das, R. Grunwald, J. Bonse. Femtosecond laser-induced periodic surface structures revisited: A comparative study on ZnO. J. Appl. Phys. 105 (2009) 34908. https://doi.org/10.1063/1.3074106.

[11] J. Bonse, S. Höhm, S.V. Kirner, A. Rosenfeld, J. Krüger. Laser-Induced Periodic Surface Structures-A Scientific Evergreen, IEEE J. Sel. Top. Quant. 23 (2017) 9000615. https://doi.org/10.1109/JSTQE.2016.2614183.

[12] J. JJ. Nivas, S. Amoruso. Generation of Supra-Wavelength Grooves in Femtosecond Laser Surface Structuring of Silicon. Nanomaterials 11 (2021) 174. https://doi.org/10.3390/nano11010174.

[13] A. Y. Vorobyev, C. Guo. Direct femtosecond laser surface nano/microstructuring and its applications. Laser Photonics Rev. 7 (2013) 385-407. https://doi.org/10.1002/lpor.201200017.

[14] J. T. Chen, W. C. Lai, Y. J. Kao, Y. Y. Yang, J. K. Sheu. Laser-induced periodic structures for light extraction efficiency enhancement of GaN-based light emitting diodes. Opt. Express 20 (2012) 5689-5695. https://doi.org/10.1364/OE.20.005689.

[15] E. Allahyari, J. JJ. Nivas, S. L. Oscurato, M. Salvatore, G. Ausanio, A. Vecchione, R. Fittipaldi, P. Maddalena, R. Bruzzese, S. Amoruso. Laser surface texturing of copper and variation of the wetting response with the laser pulse fluence. Appl. Surf. Sci. 470 (2019) 817-824. https://doi.org/10.1016/J.APSUSC.2018.11.202.

[16] J. Heitz, E. Arenholz, D. Bäuerle, R. Sauerbrey, H. M. Phillips. Femtosecond excimer-laser-induced structure formation on polymers. Appl. Phys. A 59 (1994) 289-293.https://doi.org/10.1007/BF00348232.

[17] M. Huang, F. Zhao, Y. Cheng, N. Xu, Z. Xu. Origin of laser-induced near-subwavelength ripples: interference between surface plasmons and incident laser. ACS Nano. 3 (2009) 4062-4070. https://doi.org/10.1021/nn900654v.

[18] J. Bonse, S. V. Kirner, M. Griepentrog, D. Spaltmann, J. Krüger. Femtosecond laser texturing of surfaces for tribological applications. Materials 11 (2018) 801. https://doi.org/10.3390/ma11050801.

[19] J. Bonse, M. Munz, H. Sturm. Structure formation on the surface of indium phosphide irradiated by femtosecond laser pulses. J. Appl. Phys. 97 (2005) 13538. https://doi.org/10.1063/1.1827919.

[20] Y. Zhang, Q. Jiang, M. Long, R. Han, K. Cao, S. Zhang, D. Feng, T. Jia, Z. Sun, J. Qiu, H. Xu. Femtosecond laser-induced periodic structures: mechanisms, techniques, and applications. Opto-Electronic Science 1 (2022) 220005. https://doi.org/10.29026/oes.2022.220005.

[21] F. Gesuele, J. JJ. Nivas, R. Fittipaldi, C. Altucci, R. Bruzzese, P. Maddalena, S. Amoruso. Analysis of nascent silicon phase-change gratings induced by femtosecond laser irradiation in vacuum. Sci. Rep. 8 (2018) 12498. https://doi.org/10.1038/s41598-018-30269-0.

[22] S. Maragkaki, A. Elkalash, E. L. Gurevich. Orientation of ripples induced by ultrafast laser pulses on copper in different liquids. Appl. Phys. A 123 (2017) 721. https://doi.org/10.1007/s00339-017-1336-0.

[23] M. Malinauskas, A. Žukauskas, S. Hasegawa, Y. Hayasaki, V. Mizeikis, R. Buividas, S. Juodkazis. Ultrafast laser processing of materials: from science to industry. Light Sci. Appl. 5 (2016) e16133. https://doi.org/10.1038/lsa.2016.133.

[24] L. Hong, Rusli, X. C. Wang, H. Y. Zheng, H. Wang, H. Y. Yu. Femtosecond laser fabrication of large-area periodic surface ripple structure on Si substrate. Appl. Surf. Sci. 297 (2014) 134-138.

https://doi.org/10.1016/j.apsusc.2014.01.100.

[25] R. le Harzic, D. Dörr, D. Sauer, M. Neumeier, M. Epple, H. Zimmermann, F. Stracke. Large-area, uniform, high-spatial-frequency ripples generated on silicon using a nanojoule-femtosecond laser at high repetition rate. Opt. Lett. 36 (2011) 229. https://doi.org/10.1364/ol.36.000229.

[26] J. M. Liu. Simple technique for measurements of pulsed Gaussian-beam spot sizes. Opt. Lett. 7 (1982) 196-198. https://doi.org/10.1364/OL.7.000196.

[27] E. Allahyari, J. JJ. Nivas, F. Cardano, R. Bruzzese, R. Fittipaldi, L. Marrucci, D. Paparo, A. Rubano, A. Vecchione, S. Amoruso. Simple method for the characterization of intense Laguerre-Gauss vector vortex beams. Appl. Phys. Lett. 112 (2018) 211103. https://doi.org/10.1063/1.5027661.

[28] D. Bouilly, D. Perez, L. J. Lewis. Damage in materials following ablation by ultrashort laser pulses: A molecular-dynamics study. Phys. Rev. B 76 (2007) 184119. https://doi.org/10.1103/PhysRevB.76.184119.

[29] N. Epperlein, F. Menzel, K. Schwibbert, R. Koter, J. Bonse, J. Sameith, J. Krüger, J. Toepel. Influence of femtosecond laser produced nanostructures on biofilm growth on steel. Appl. Surf. Sci. 418 (2017) 420-424. https://doi.org/10.1016/j.apsusc.2017.02.174.

[30] J. Bonse, S. Höhm, R. Koter, M. Hartelt, D. Spaltmann, S. Pentzien, A. Rosenfeld, J. Krüger. Tribological performance of sub-100-nm femtosecond laser-induced periodic surface structures on titanium. Appl. Surf. Sci. 374 (2016) 190-196. https://doi.org/10.1016/j.apsusc.2015.11.019.

[31] Z. Wang, Q. Zhao, C. Wang. Reduction of friction of metals using laser-induced periodic surface nanostructures. Micromachines (Basel). 6 (2015) 1606-1616. https://doi.org/10.3390/mi6111444.

[32] J. Eichstät, G. R. B. E. Römer, A. J. Huis in't Veld. Towards friction control using laser-induced periodic Surface Structures. Physics Procedia12 (2011) 7-15. https://doi.org/10.1016/j.phpro.2011.03.099.

[33] F. Fraggelakis, G. Mincuzzi, J. Lopez, I. Manek-Hönninger, R. Kling. Texturing metal surface with MHz ultra-short laser pulses. Opt. Express 25 (2017) 18131. https://doi.org/10.1364/OE.25.018131.

[34] A. Y. Vorobyev, C. Guo. Colorizing metals with femtosecond laser pulses. Appl. Phys. Lett. 92 (2008) 41914. https://doi.org/10.1063/1.2834902.

[35] A. Y. Vorobyev, C. Guo. Spectral and polarization responses of femtosecond laser-induced periodic surface structures on metals. J. Appl. Phys. 103 (2008) 043513. https://doi.org/10.1063/1.2842403.

[36] J. Yao, C. Zhang, H. Liu, Q. Dai, L. Wu, S. Lan, A. V. Gopal, V. A. Trofimov, T. M. Lysak. Selective appearance of several laser-induced periodic surface structure patterns on a metal surface using structural colors produced by femtosecond laser pulses. Appl. Surf. Sci. 258 (2012) 7625-7632. https://doi.org/10.1016/j.apsusc.2012.04.105.

[37] M. S. Ahsan, F. Ahmed, Y. G. Kim, M. S. Lee, M. B. G. Jun. Colorizing stainless steel surface by femtosecond laser induced micro/nano-structures. Appl. Surf. Sci. 257 (2011) 7771-7777. https://doi.org/10.1016/j.apsusc.2011.04.027.

[38] Z. Ou, M. Huang, F. Zhao. Colorizing pure copper surface by ultrafast laser-induced near-subwavelength ripples. Opt. Express 22 (2014) 17254. https://doi.org/10.1364/oe.22.017254.

[39] J. Long, P. Fan, M. Zhong, H. Zhang, Y. Xie, C. Lin. Superhydrophobic and colorful copper surfaces fabricated by picosecond laser induced periodic nanostructures. Appl. Surf. Sci. 311 (2014) 461-467. https://doi.org/10.1016/j.apsusc.2014.05.090.

[40] A. A. Ionin, S. I. Kudryashov, S. V. Makarov, L. V. Seleznev, D. V. Sinitsyn, E. V. Golosov, O. A. Golosova, Y. R. Kolobov, A. E. Ligachev. Femtosecond laser color marking of metal and semiconductor surfaces. Appl. Phys. A 107 (2012) 301-305. https://doi.org/10.1007/s00339-012-6849-y.

[41] B. Dusser, Z. Sagan, H. Soder, N. Faure, J. P. Colombier, M. Jourlin, E. Audouard. Controlled nanostructrures formation by ultra fast laser pulses for color marking. Opt. Express 18 (2010) 2913-2924. https://doi.org/10.1364/OE.18.002913.

[42] V. Zorba, E. Stratakis, M. Barberoglou, E. Spanakis, P. Tzanetakis, C. Fotakis. Tailoring the wetting response of silicon surfaces via fs laser structuring. Appl. Phys. A 93 (2008) 819-825. https://doi.org/10.1007/s00339-008-4757-y.

[43] Y. Fuentes-Edfuf, J. A. Sánchez-Gil, C. Florian, V. Giannini, J. Solis, J. Siegel. Surface Plasmon Polaritons on Rough Metal Surfaces: Role in the Formation of Laser-Induced Periodic Surface Structures. ACS Omega 4 (2019) 6939-6946. https://doi.org/10.1021/acsomega.9b00546.

[44] J. Bonse, A. Rosenfeld, J. Krüger. On the role of surface plasmon polaritons in the formation of laser-induced periodic surface structures upon irradiation of silicon by femtosecond-laser pulses. J. Appl. Phys. 106 (2009) 104910. https://doi.org/10.1063/1.3261734.

[45] J. Bonse, S. V. Kirner, S. Höhm, N. Epperlein, D. Spaltmann, A. Rosenfeld, J. Krüger. Applications of laser-induced periodic surface structures (LIPSS). Proc. SPIE 10092, Laser-Based Micro- and Nanoprocessing XI. (2017) 100920. https://doi.org/https://doi.org/10.1117/12.2250919.

[46] J. F. Young, J. E. Sipe, H. M. van Driel. Laser-induced periodic surface structure. III. Fluence regimes, the role of feedback, and details of the induced topography in germanium. Phys. Rev. B 30 (1984) 2001-2015. https://doi.org/10.1103/PhysRevB.30.2001.

[47] J. P. Colombier, F. Garrelie, P. Brunet, A. Bruyère, F. Pigeon, R. Stoian, O. Parriaux. Plasmonic and Hydrodynamic Effects in Ultrafast Laser-Induced Periodic Surface Structures on Metals.Journal of Laser Micro/Nanoengineering. 7 (2012) 362-368. https://doi.org/10.2961/jlmn/2012.03.0023.ujm-00751462.

[48] E. L. Gurevich. Mechanisms of femtosecond LIPSS formation induced by periodic surface temperature modulation. Appl. Surf. Sci. 374 (2016) 56-60. https://doi.org/10.1016/j.apsusc.2015.09.091.

[49] T. Karkantonis, A. Gaddam, T. L. See, S. S. Joshi, S. Dimov. Femtosecond laser-induced sub-micron and multi-scale topographies for durable lubricant impregnated surfaces for food packaging applications. Surf. Coat. Technol. 399 (2020) 126166. https://doi.org/10.1016/j.surfcoat.2020.126166.

[50] I. Kukavica, M. Ziane. Navier-Stokes equations with regularity in one direction. J. Math. Phys. 48 (2007) 065203. https://doi.org/10.1063/1.2395919.

[51] M. Marion, R. Temam, P. G. Ciarlet, J. L. Lions. Navier-Stokes Equations: Theory and Approximation Handb. Numer. Anal. 6 (1998) 503-689. https://doi.org/10.1016/S1570-8659(98)80010-0.

[52] J. Bonse. Quo vadis LIPSS?—recent and future trends on laser-induced periodic surface structures. Nanomaterials 10 (2020) 1950. https://doi.org/10.3390/nano10101950.

[53] I. Gnilitskyi, T. J. Y. Derrien, Y. Levy, N. M. Bulgakova, T. Mocek, L. Orazi. High-speed manufacturing of highly regular femtosecond laser-induced periodic surface structures: physical origin of regularity. Sci. Rep. 7 (2017) 8485. https://doi.org/10.1038/s41598-017-08788-z.

[54] Z. Li, X. Wang, J. Nie. Formation of periodic ripples on silicon surface ablated by femtosecond laser. Acta Physica Sinica 66 (2017) 105201. https://doi.org/10.7498/aps.66.105201.

[55] C. Li, R. Stoian, G. Cheng. Laser-induced periodic surface structures with ultrashort laser pulse. Chinese Optics 11 (2018) 1-17. https://doi.org/10.3788/co.20181101.0001.

Chapter 2

Experimental Methods

This chapter illustrates the experimental methods employed in this thesis work presenting briefly the types of femtosecond (fs) laser sources used in the surface structuring experiments and the main instrumental methods used for their characterization: the optical microscope (OM), the scanning electron microscope (SEM)) and atomic force microscope (AFM). The images of the samples surface have been mainly analyzed by using *ImageJ* and *Gwyddion* softwares and exploiting two-dimensional fast Fourier transform (2D-FFT) and two-dimensional inverse fast Fourier transform (2D-IFFT) processing. Finally, the analysis of craters generated by Gaussian laser beams focused by spherical and cylindrical lenses is discussed for the determination of the laser spot size on the target surface and the threshold fluence F_{th} for the formation of the various surface structures is discussed.

2.1 Introduction

Femtosecond (fs) lasers have gradually become a new tool for convenient and effective processing of materials receiving extensive research attention in the past decades thanks to the many advantages offered by the ultrashort pulse duration [1-3]. Due to an ultra-short pulse duration and an ultra-strong peak power, fs laser pulses can allow high-quality surface processing of almost any material, fundamentally limiting the problem of damages caused by thermal melting effects associated to traditional long-pulse laser processing. In the process of fs laser interaction with a solid target, surface periodic micro-nano structures can be generated, whose characteristic sizes are usually in the subwavelength range or even reach nanoscale in specific situations. At present, these surface micro-nano structures have been widely used in different fields of physics, biology and chemistry.

Gaussian laser beams, i.e. beams characterized by a Gaussian spatial intensity profile, are generally applied and focused on the target surface [4]. Here we will illustrate how they can be applied in the field of fs laser processing, especially in the formation of micro/nano surface structures [5-6].

The chapter is organized as follows: section 2.2 presents the experimental setup for fs laser surface structuring, whereas section 2.3 briefly discusses the determination of the characteristics of the Gaussian beam and target response.

2.2 General experimental setup for fs laser surface structuring

The equipment used in the experiments and data analysis carried out in my PhD research work can be schematically divided into the following three parts:

1. The laser system and accessories for surface processing providing an integrated optical system for surface structuring of the target through the laser control and the scanning of the sample.

2. The optical (OM), scanning electron (SEM) and atomic force (AFM) microscopes allowing the analysis of the morphological features of the processed samples.

3. The softwares *ImageJ* and *Gwyddion* exploited to perform image processing on the specific morphological images in order to get specific data for process characterization and analysis.

2.2.1 The laser system and accessories for surface processing

Nowadays, the research on laser induced periodic surface structures (LIPSS) of materials are very extensive, but the number of laser systems and optical devices has become rather typical [2]. Generally, research of fs laser surface structuring involves the use of solid-state fs laser sources based on Chirped Pulse Amplification (CPA) [7-8].

Fig. 2.1 shows a typical experimental setup used for LIPSS generation. The laser system can generate laser pulses characterized by a fundamental wavelength at a specific pulse duration at a given repetition rate (RR). The intense fs laser pulses used in laser processing experiments are obtained through amplification in a regenerative amplifier (RA) that can work at a determined RR; moreover, at a fixed power (P) the higher RR the lower the energy per pulse E (E=P/RR). Other wavelengths can be generated through appropriate nonlinear crystals. Once the laser beam is selected, it is transported through an optical system and eventually focused on the sample. The sample is located on an appropriate holder and can be processed in air at atmospheric pressure or in a vacuum chamber.

The experiments carried out in the frame of this thesis namely exploited a diode pumped CPA Yb:KGW laser system (Pharos, Light Conversion) delivering fs laser pulses with a duration of ≈180 fs at a fundamental wavelength of ≈1030 nm. The maximum value of the RR is 200 kHz and the maximum optical power is ≈ 6 W. At RR below 3 kHz, the maximum pulse energy is of ≈ 2 mJ. In addition, a Titanium: Sapphire laser system (Legend, Coherent

Inc.) was also used in some experiments. This system can generate a maximum power of 4 W emitting ≈35 fs pulses at 800 nm fundamental wavelength and at 1 kHz repetition rate. In the processing of some samples, we also used the nanosecond Gaussian beams provided by a Quantel Brilliant-b Nd:YAG laser at 1064 nm, frequency doubled to 532 nm, 5 ns FWHM, at a RR of 20 Hz.

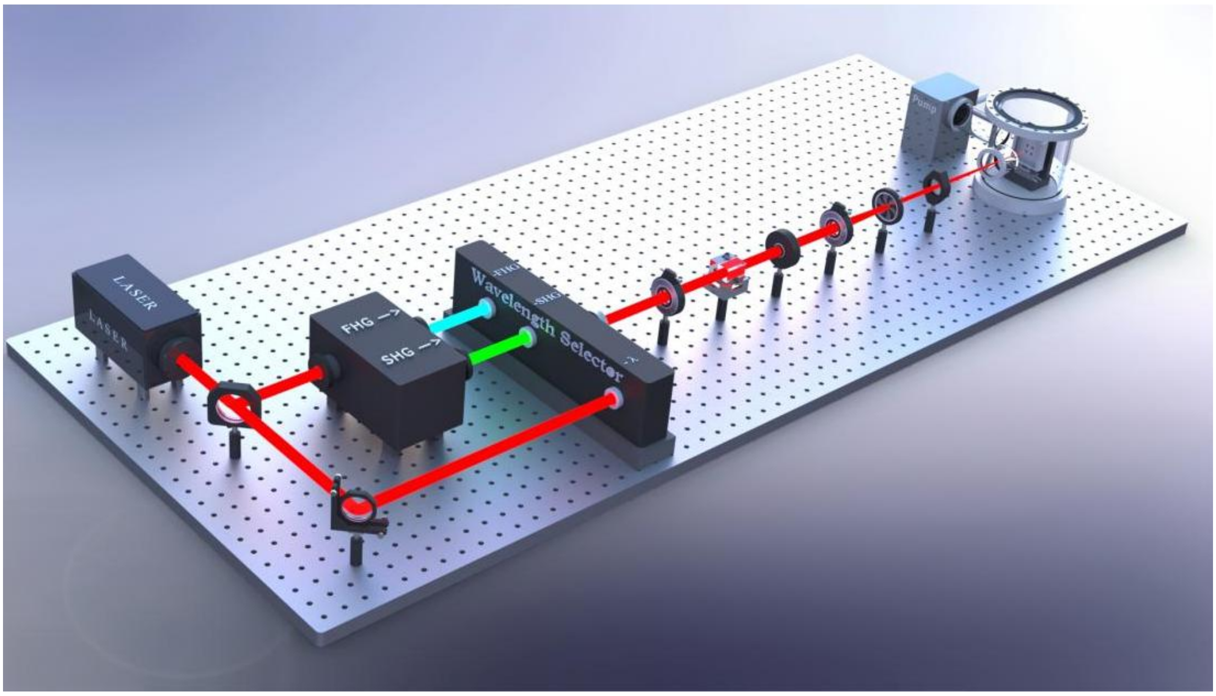

Fig. 2.1 Typical experimental setup for femtosecond laser surface structuring.

As said, other wavelengths can also be generated. Taking the Yb:KGW laser as an example, its fundamental output is at 1030 nm, but also visible and ultraviolet light pulses at 515 nm and 257 nm can be obtained through a harmonic generator system exploiting second and fourth harmonic nonlinear crystals (HIRO, Light Conversion). Generally, the combination of half-wave plate and polarizer is used to control the energy of the laser pulses, but for some laser systems the pulse energy can be also controlled directly by internal software. An electromechanical shutter fixes the number of pulses for generating spots at a fixed location of the target surface (static configuration) or for blocking the laser beam in raster scanning during the texturing of large areas (dynamic configuration). The laser pulse is focused through a lens on the surface of the sample, which is positioned perpendicular to the laser beam and mounted on a computer-controlled translation stage that allows moving it along the x, y, and z directions. In some experiments, the sample scanning system is located into a vacuum chamber in order to carry out experiments in vacuum or in other gas environment (e.g.

nitrogen) at a given pressure. Wave plates and iris are generally used to control laser polarization and remove possible laser distortion at the beam edges, respectively. A power meter is used to monitor the energy of the laser beam reaching the target surface.

2.2.2 Sample morphological analysis by optical, scanning electron and atomic force microscopes

The sample surface is typically analyzed by means of optical, scanning electron and atomic force microscopes. The optical microscope (OM) allows enlarging images of tiny objects that could not be resolved by human eyes, thus permitting to gain information on fine structures [9]. In this study, a Zeiss Axio A1 microscope (Fig. 2.2(b)) was used to observe and analyze the sample surface morphological characteristics induced by the laser processing. The microscope can operate both with transmitted and reflected light configurations. In the microscopic observation of solid, non-transparent samples, the system basically works under brightfield, irradiating the sample with strong light and collecting the light through the objective lens (reflected light microscope). The microscope is equipped with 4 objective lenses with magnifications of 5×, 10×, 20× and 50×, various illumination sources including a 100 W halogen bulb, a high-resolution camera and the Zeiss Axio Vision imaging software allowing to acquire and store optical images and make measurements for the data analysis.

Panels (b) and (c) in Fig. 2.2 reports OM images of the modifications induced by fs laser pulses at $\lambda = 1030\ nm$ on a copper target leading to the generation of circular (panel (b) - spherical lens with a focal length f ~200 mm) and elliptical (panel (c) - cylindrical lens with f~150mm) craters. Panel (b) displays OM images of craters formed at three different RRs (namely, 5 kHz, 10 kHz and 25 kHz) at a pulse energy E = 55 μJ. It can be observed that the different RRs do not cause substantial changes in the general features of the crater structure on the copper sample, thus suggesting that the copper surface is not affected by heat accumulation and plume shielding effects in these experimental conditions. These phenomena are common in experiments carried out at high repetition rates (from kHz to several MHz). Panel (c) displays elliptical craters obtained by laser focusing using a cylindrical lens. The OM images were obtained at 6 different pulse energies (namely 506 μJ, 492 μJ, 469 μJ, 436 μJ, 392 μJ, 356 μJ) and allowed the observation that the higher the energy the longer and clearer the generated craters. Hence, OM can be used to timely observe the features of the ablated craters, lines or areas for the selection of the experimental settings and crater analysis.

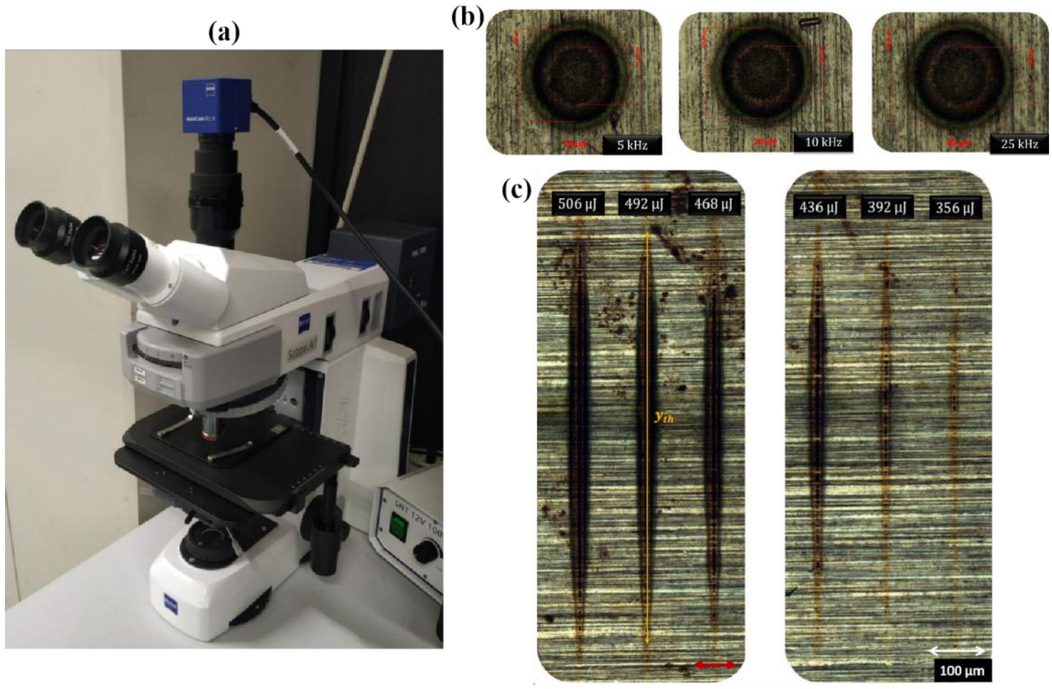

Fig. 2.2 (a) Photo of the Zeiss Axio Scope A1 employed in our research. (b) OM images of craters generated on a copper sample by focusing with the spherical lens (f ~200 mm) a train of N = 200 pulses at λ = 1030 nm, at variable repetition rate RR (5 kHz, 10 kHz and 25 kHz). (c) OM images of craters generated on copper at 1030 nm with a cylindrical lens (f~150mm) for different laser pulse energies. The red arrow in the left panel (c) represents the laser beam polarization, while the long yellow arrow indicates how the major axis of the elliptical craters was measured.

Scanning electron microscopy (SEM) allows sample observation at a resolution much larger than optical microscopy. It uses a narrow focused high-energy electron beam to scan the sample, stimulates various physical information through the interaction between the beam and the materials, and collects, amplifies and re-images this information to achieve the purpose of characterizing the microscopic morphology of the material. The spatial resolution of SEM can reach about 1 nm; the magnification can reach 300,000 times and continuous adjustment can be performed by exploiting the good depth of field, field of vision and imaging stereo effects. In addition, the combination of SEM and other analytical instruments can be used to observe the microscopic morphology and simultaneously carry out the analysis of the micro-area composition of the material. SEM is widely used in the study of geotechnical, graphite, ceramics and nanomaterials playing an important role in the field of scientific research [10].

The morphological characterization of the irradiate surface samples is carried out by using a field emission scanning electron microscope (FE-SEM - Zeiss Σigma), as shown in Fig. 2.3(a). The SEM is equipped with a specimen holder supporting up to nine targets. The system is equipped with two detectors: one for the collection of backscattered electrons placed perpendicular to the sample and one for the detection of secondary electrons positioned at 45 degrees with respect to the normal to the sample. The latter is an Everhart - Thornley (ET) detector, the former is an In-Lens (IL) detector located inside the electron column of the microscope and it is usually used to register SEM images at high contrast. The IL detector provides images more sensitive to the surface properties since it effectively collects the secondary electrons (SE) scattered by the very surface of the sample, meanwhile the images of the ET detector are formed by SE returning to the surface after several inelastic scattering events in the sample providing morphological features mainly related to topographical properties.

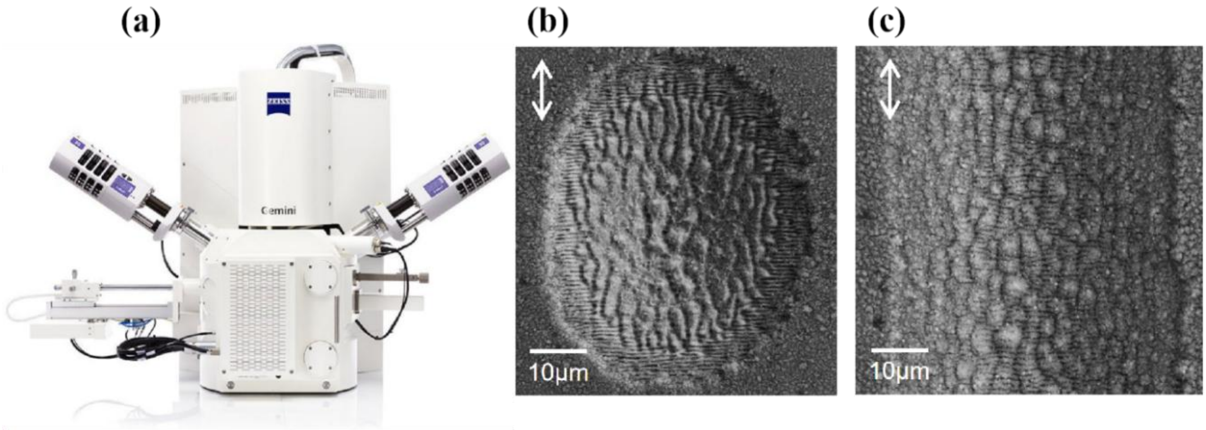

Fig. 2.3 (a) Picture of a field emission scanning electron microscope (FE-SEM – Zeiss Σigma) (image taken from Zeiss website [11]). Panels (b) and (c) report two SEM images of a silicon target surface after static and dynamic irradiations at a pulse energy E~10 μJ. The circular crater in panel (b) was produced on a static target with a sequence of N=200 pulses, whereas the shallow line in panel (c) was generated on a scanning target moving at a velocity V_s= 0.25 mm/s, for an effective number of pulses N_{eff} = 200. The double-headed arrows illustrate the laser pulse polarization direction.

Panels (b) and (c) in Fig. 2.3 display two exemplificative images of a silicon sample irradiated at the same pulse energy E~10 μJ for a static spot (N=200) and a dynamic line (effective pulse number N_{eff}=200), respectively. The double-headed arrow in the SEM images identify the direction of the laser pulse polarization. Different kind of surface structures can be recognized in the irradiated areas, such as ripples perpendicular to the laser polarization and grooves parallel to the laser polarization both in the static and dynamic configuration. At high laser energy a deep hole is typically formed on the target surface in the positions hit by the high-energy, central part of the laser beam spot.

The integrated system WITEC - Alpha300 RAS can be switched at will between AFM and confocal micro-Raman configurations [16], allowing a combined topographical and spectral characterization of a specified microregion of the sample under analysis. Exploiting the optical "pre-observation" by various lighting and sensing techniques (e.g. bright-field, dark-field, polarization, fluorescence, etc.), the area of interest for the measurements, can be accurately determined. The sample topographies can be studied by AFM in ac or contact modes. For the micro-Raman analysis, laser beams at different wavelengths can be used as excitation light source. The beam is focused onto the sample surface by means of a 50x microscope objective (numerical aperture of 0.75) working in epi-illumination mode, ensuring a diffraction-limited focused spot in the objective focal plane with a full width at half-maximum (FWHM) of approximately 320 nm. The light backscattered from the sample is collected by the same objective and sent to the spectrograph through a confocal optical collection path using an optical fiber whose core diameter can be selected among 25-50-100 μm.

2.2.3 Image processing

Digital image processing consists in the use of computer algorithms and programs to modify, repair, filter or decrypt digital images. The advent and development of image processing can be attributed to three factors: the development of computers, the improvement of mathematical theory, and the increase in demand in the various sectors: environmental, military, industrial, medical and scientific. The ability of computers is to collect large number of details that could escape to the human eyes. For example, a program can identify the differences between two images, thus distinguishing a fake from an original. In the following, the procedures for the analysis of the sample's images obtained by the scanning electron microscope are briefly addressed. Two different software were used for this purpose: *ImageJ* [12] and *Gwyddion* [13]. A brief description of the functions offered by the two softwares and used in the frame of this PhD thesis is reported hereafter.

With the *ImageJ* program it was possible to carry out repeated measurements of the area of the craters and the thickness of the lines produced. After performing the calibration, the program shows in a window the value of the quantity chosen with the appropriate selection tools. If the measurement is repeated several times, it is possible to quickly obtain the average value and the standard deviation of specific surface features. In particular, it allows measuring the periods of the LIPSS, when these are well developed and sufficiently distinguishable. A direct analysis of the surface structures period is carried out with the *ImageJ* program, which is capable of measuring the distance between the peaks characterized by different intensity in gray scale that corresponds to the spatial separation between two successive LIPSS, and therefore allows gaining an estimate of the period. The other method used to measure the period consists in the use of two-dimensional Fast Fourier Transform (2D-FFT), as illustrated below in detail.

Fast Fourier Transform (FFT) is a useful algorithm for computing the discrete Fourier transform, or its inverse [14]. It can be clearly defined in multiple dimensions: hence as digital images are two-dimensional, 2D-FFT is used in the image processing. Applying 2D-FFT to an image leads from the spatial domain to the frequency domain, in which periodic patterns present within the image are easily recognized. This technique allows a detailed analysis of the distribution of spatial frequencies of the LIPSS from the SEM images.

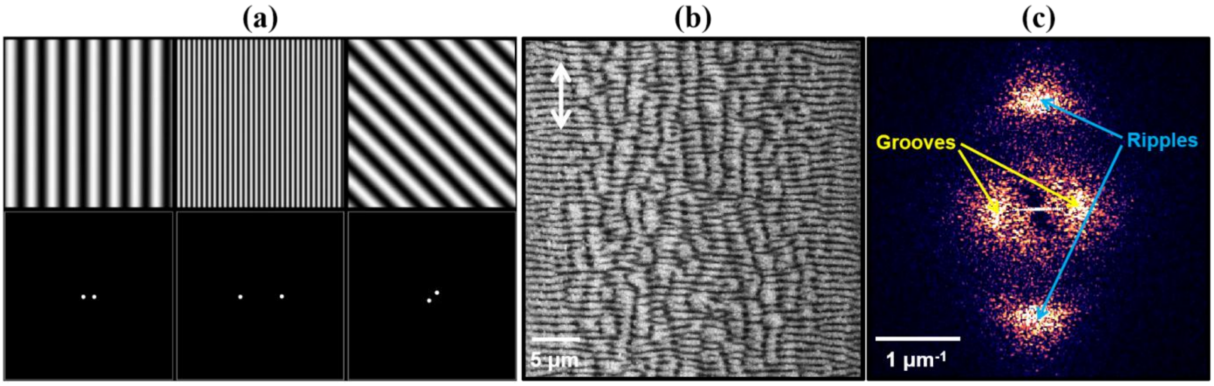

Fig. 2.4 (a) Examples of images with regular spatial patterns (upper panels) and corresponding 2D-FFT images in the frequency domain (lower panels). (b) SEM image of a silicon target showing surface structures produced by laser pulses with E=6.1 μJ at a scanning velocity V_s=0.35 mm/s. The double-headed arrow indicates the incident laser pulse polarization. Panel (c) is the 2D-FFT map of the SEM image of panel (b).

Suppose to have images in two dimensions with perfect periodic patterns as shown in the upper panels of Fig. 2.4(a). Applying the 2D-FFT algorithm to these images, two points are observed in the frequency space, oriented according to the direction of the spatial pattern, as observed in the lower panels of Fig. 2.4(a). The separation of the points increases if the spatial period decreases, and therefore the frequency increases. The white points therefore indicate the reciprocal of the period of the patterns in the starting images. Applying this technique to surfaces with periodic structures induced by laser pulses can help not only for a more detailed morphological analysis, but also to consolidate the model that supports their formation. In this thesis, the *Gwyddion* program is used to generate and evaluate the 2D-FFT of the SEM images, that is, the structured regions of the samples. In the SEM images of Fig. 2.4(b), for example, we can distinguish a distribution of horizontally oriented ripples, and a vertical component of grooves still under development. The LIPSS in this case do not constitute a perfect pattern, but their period presents a dispersion around an average value. In the corresponding space of the spatial frequencies, the points are replaced by more extended characteristic regions in the shape of a sickle. Their direction confirms the different orientation of the LIPSS with respect to the polarization of the laser beam. The spectrum of the FFT is also influenced by the presence of nanoparticles on the sample surface.

A direct analysis of the periods is carried out again with the *ImageJ* program, capable of generating a two-dimensional graph of the intensity of the pixels along the selected yellow lines, as reported in Fig. 2.5. An easier visualization of such effects can be gained by using the 2D inverse FFT (2D-IFFT) of the spectral frequency peaks of any specific surface structure. 2D-IFFT maps were generated by using the filtering method offered by *Gwyddion* software. The reconstructed maps of the surface spatial modulation corresponding to ripples and grooves are separately displayed in panels (b) and (e) of Fig. 2.5, respectively. The 2D-IFFT analysis allows a more direct visualization of the individual surface features associated to the intense peaks of the Fourier spectra reported in panels (c) and (f).

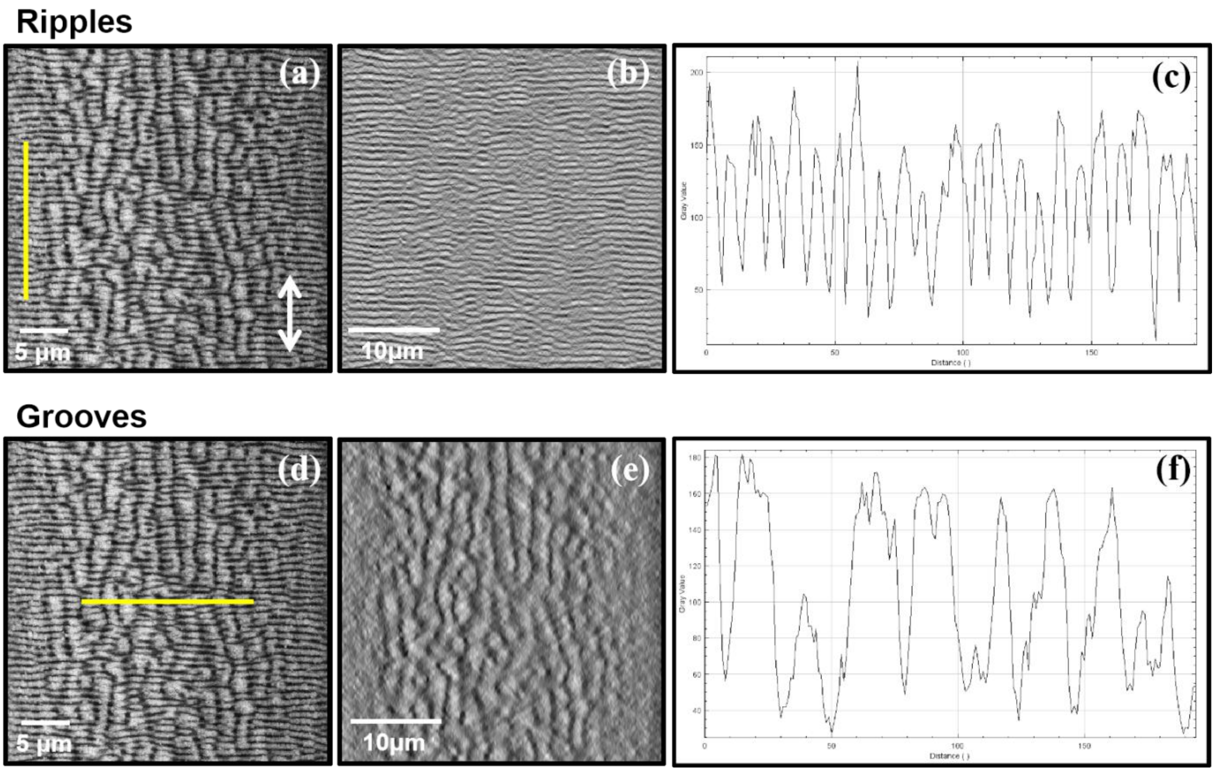

Fig. 2.5 Panels (a) and (d) display SEM images of a portion of the linear shallow craters produced with V_s=0.35 mm/s and E=6.1 μJ. The double headed arrow in panel (a) marks the laser beam polarization direction. Panel (b) are morphology maps in the real space generated through 2D-IFFT by selecting only the spectral frequency features associated to ripples, whereas panel (e) are morphology maps in the real space generated through 2D-IFFT by selecting only the spectral frequency features associated to grooves. Panels (c) and (f) are the graphs of the intensity of the pixels of the yellow selection in (a) and (d).

2.3 Analysis of the surface features for a Gaussian beam

In this chapter, irradiation with a Gaussian beam [5] is taken as case to illustrate the determination of the characteristic threshold fluence for specific processes (such as ablation, structure formation, surface modification, etc.). The procedure can also allow determining the laser spot size on the sample surface and has also been shown to be effective for beams with more complex spatial shapes, such as vector vortex beams carrying orbital angular momentum [15].

The plano-convex spherical lens and plano-convex cylindrical lens are mainly used to focus the Gaussian beam on the material surface in my research work. The plano-convex spherical lens is a converging lens characterized by a spherical surface on one side and a plane surface on the other, which is commonly used in optical systems. In my study, it is used to focus the laser beam, placing the sample in the focal plane and the spherical surface facing the incoming beam (the infinite conjugate plane) to reduce the effects of aberrations. In some experiments, a plano-convex cylindrical lens was also used to produce elliptical spots.

Hereafter, we will explore the specific theoretical formulas for the determination of threshold fluences of the features formed on the sample surface, such as ablated circular (plano-convex spherical lens) and elliptical craters (plano-convex cylindrical lens) under the Gaussian beam model.

2.3.1 Characterization of circular craters

The laser beam with wavelength λ emitted by the fs laser can form a circular crater on the sample through a spherical lens, as shown in Fig. 2.6(a). In an attempt to further characterize the aspect of circular craters, the threshold fluences are estimated for the formation of the ripples $\mathrm{F_{th-Ripples}}$ and grooves $\mathrm{F_{th-Grooves}}$ in the irradiated spot, as depicted in Fig. 2.6(b). The two concentric regions of surface structures covering the shallow crater are separated by a very thin annulus where ripples and grooves coexist. The spot size was also estimated by producing shallow circular craters on a target and analyzing the energy variation of the crater areas [5]. The results were consistent with a Gaussian beam profile and the estimated laser beam radius, at $1/e^2$ of the maximum intensity was estimated.

Considering a Gaussian spatial profile produced by a spherical lens on the target surface, the threshold fluence for the production of LIPSS is estimated by studying the variation of the areas covered by these structures, when changing the energy values of the laser pulses. The fluence profile of the Gaussian beam is described by Eq. (1):

$$\mathrm{F(r)} = \int_{-\infty}^{\infty} \mathrm{I(r,t)dt} = \mathrm{F_p} e^{\frac{-2r^2}{\omega_0^2}}\ ,\ \text{with}\ \ \mathrm{F_p} = \frac{2\mathrm{E}}{\pi\omega_0^2}\,, \tag{1}$$

where r is the radial distance from the beam axis, F_p is the peak value of the fluence, E is the energy of the laser pulse and ω_0 the beam waist. When observing a crater of radius r_{th}, the fluence for ablation F_{th} is formed at the points as shown in panel (b) of Fig. 2.6. The value of the fluence on the edge of the crater is therefore named the threshold fluence F_{th}:

$$F_{th} = F(r_{th}) = F_p e^{\frac{-2r_{th}^2}{\omega_0^2}}\ . \tag{2}$$

F_{th} corresponds to the peak value of the fluence $\mathrm{F_p}$ which would lead to induce the ablation process only in one point on the beam axis, as indicated in Fig. 2.6. Therefore, the value of F_{th} is linked to a threshold energy E_{th} by the relationship:

$$F_{th} = \frac{2\mathrm{E}_{th}}{\pi\omega_0^2}\,,\ \text{where}\ \ E_{th} = Ee^{\frac{-2r_{th}^2}{\omega_0^2}}\ . \tag{3}$$

The functional dependence of r_{th} on E_{th} can be expressed by inverting Eq. (2)

$$r_{th}^2 = \frac{\omega_0^2}{2}\ln\frac{F_p}{F_{th}} = \frac{\omega_0^2}{2}\ln\frac{E}{E_{th}} = \frac{\omega_0^2}{2}(\ln E - \ln E_{th})\ . \tag{4}$$

For the following analysis the radius of the craters r_{th} was measured, in an almost circular approximation. By making a linear fit between radius squared r_{th} and $\ln E$: $r_{th}^2 = a\ln E + b$, the beam waist can be obtained

$$\omega_0 = \sqrt{2a}, \tag{5}$$

with the corresponding error

$$\Delta\omega_0 = \frac{\Delta a}{\sqrt{2a}}\ . \tag{6}$$

Besides, the threshold energy and its standard deviations are

$$E_{th} = e^{-\frac{b}{a}}\,, \tag{7}$$

$$\Delta E_{th} = \sqrt{\left(\frac{\partial E_{th}}{\partial a}\right)^2 \Delta a^2 + \left(\frac{\partial E_{th}}{\partial b}\right)^2 \Delta b^2 + 2\left(\frac{\partial E_{th}}{\partial a}\right)\left(\frac{\partial E_{th}}{\partial b}\right) cov(a,b)}$$

$$= \sqrt{\left(\frac{e^{-\frac{b}{a}} * b}{a^2}\right)^2 \Delta a^2 + \left(\frac{-e^{-\frac{b}{a}}}{a}\right)^2 \Delta b^2 + 2\left(\frac{e^{-\frac{b}{a}} * b}{a^2}\right)\left(\frac{-e^{-\frac{b}{a}}}{a}\right) cov(a,b)}\ . \tag{8}$$

It ends with the estimate of the threshold fluence for ablation

$$F_{th} = \frac{2E_{th}}{\pi\omega_0^2}\,, \qquad \Delta F_{th} = \frac{F_{th}}{E_{th}}\Delta E_{th}\ . \tag{9}$$

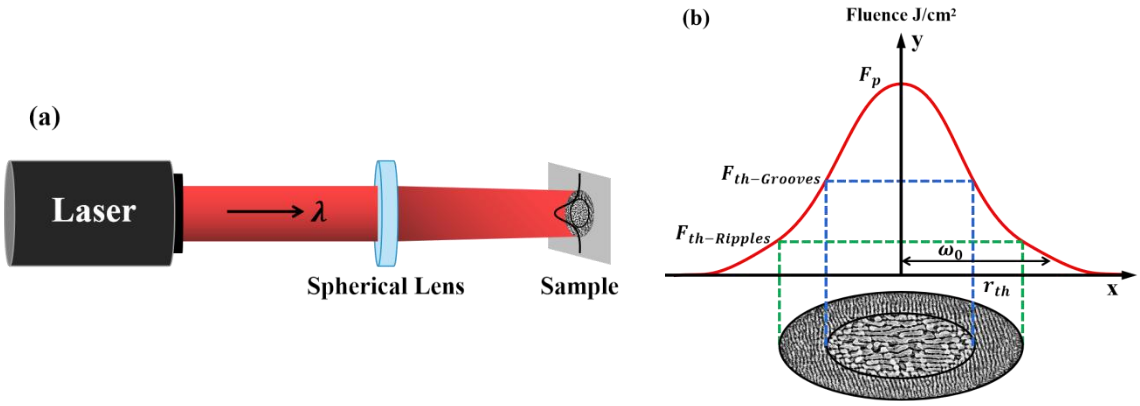

Fig. 2.6 (a) The Gaussian profile after spherical lens along the sample surface. (b) Portion of a SEM micrograph of the silicon target surface and the corresponding Gaussian spatial profile of the laser beam. The horizontal lines at $F_{th-Ripples}$ and $F_{th-Grooves}$ identify the values of the laser threshold fluences for ripples and grooves formation, respectively. The SEM image refers to N=300, F_p=0.47 J/cm^2, ω_0 = 30 μm in air.

2.3.2 Characterization of elliptical craters

In the following, we generalize the Gaussian beam model extending it to the case of elliptical craters obtained by focusing with a plano-convex cylindrical lens along a line on the sample surface (Fig. 2.7(a)). The reason for choosing a cylindrical lens is that it achieves larger area textures in less time than a spherical lens. As mentioned before, the distribution of the laser beam along the sample surface is still Gaussian. But because the ellipse has different dimensions in the x and y directions, as shown in the Fig. 2.7(b), in the x direction, due to the focusing of the cylindrical lens, a narrower structure is formed, so that the overall sample surface displays a characteristic elliptically shaped crater.

We assume that the spatial intensity distribution of the beam on the target will result in different Gaussian widths $\omega_{0,x}$ and $\omega_{0,y}$, thus the fluence profile for an elliptical crater is described as

$$F(x,y) = F_p e^{\frac{-2x^2}{\omega_{0,x}^2}} e^{\frac{-2y^2}{\omega_{0,y}^2}} \quad \text{with} \quad F_p = \frac{2E}{\pi\, \omega_{0,x}\, \omega_{0,y}} = \frac{2E}{S}. \tag{10}$$

Here the fluence profile can be separated along the x and y directions with the following two equations

$$F(x) = F_{p,x} e^{\frac{-2x^2}{\omega_{0,x}^2}}, \qquad F(y) = F_{p,y} e^{\frac{-2y^2}{\omega_{0,y}^2}}. \tag{11}$$

In the same way where F_p is the peak value of fluence, E is the energy of the laser pulse and ω_0 the beam waist. Considering that the discussion in the x-direction and the y-direction is consistent, here we mainly expand the Gaussian function on the x-axis. The value of the threshold fluence F_{th} on the x-axis is

$$\mathrm{F_{th,x}} = \mathrm{F(r_{th,x})} = \mathrm{F_{p,x}} e^{\frac{-2\mathrm{r_{th,x}^2}}{\omega_{0,x}^2}} = \frac{2\mathrm{E}}{\pi\,\omega_{0,x}^2} e^{\frac{-2\mathrm{r_{th,x}^2}}{\omega_{0,x}^2}} = \frac{2E_{th,x}}{\pi\omega_{0,x}^2}, \text{ with } E_{th,x} = Ee^{\frac{-2r_{th,x}^2}{\omega_{0,x}^2}}. \quad (12)$$

Then, the functional dependence of r_{th} on E_{th} can be expressed by inverting Eq. (12),

$$r_{th,x}^2 = \frac{\omega_{0,x}^2}{2} \ln \frac{E}{E_{th,x}} = \frac{\omega_{0,x}^2}{2} (\ln E - \ln E_{th,x}). \quad (13)$$

After performing the analysis on x-axis and y-axis, the consistency between $E_{th,x}$ and $E_{th,y}$ can be obtained and the energy threshold $\mathrm{E_{th}}$ is eventually estimated as

$$E_{th} = \frac{E_{th,x}+E_{th,y}}{2}, \text{ with errors } \Delta\mathrm{E_{th}} = \frac{\sqrt{\Delta\mathrm{E_{th,x}^2} + \Delta\mathrm{E_{th,y}^2}}}{2}. \quad (14)$$

Besides, the total spot S is

$$S = \pi\,\omega_{0,x}\,\omega_{0,y}, \text{ with error } \Delta S = \sqrt{\left(\frac{\partial S}{\partial\omega_{0,x}}\right)^2 (\Delta\omega_{0,x})^2 + \left(\frac{\partial S}{\partial\omega_{0,y}}\right)^2 (\Delta\omega_{0,y})^2}. \quad (15)$$

Finally the threshold fluence and its standard deviations are estimated as:

$$F_{th} = \frac{2E_{th}}{\pi\,\omega_{0,x}\,\omega_{0,y}} = \frac{2\mathrm{E}}{\mathrm{S}}, \text{ with } \Delta F_{th} = \sqrt{\left(\frac{\partial F_{th}}{\partial E_{th}}\right)^2 (\Delta E_{th})^2 + \left(\frac{\partial F_{th}}{\partial S}\right)^2 (\Delta S)^2}. \quad (16)$$

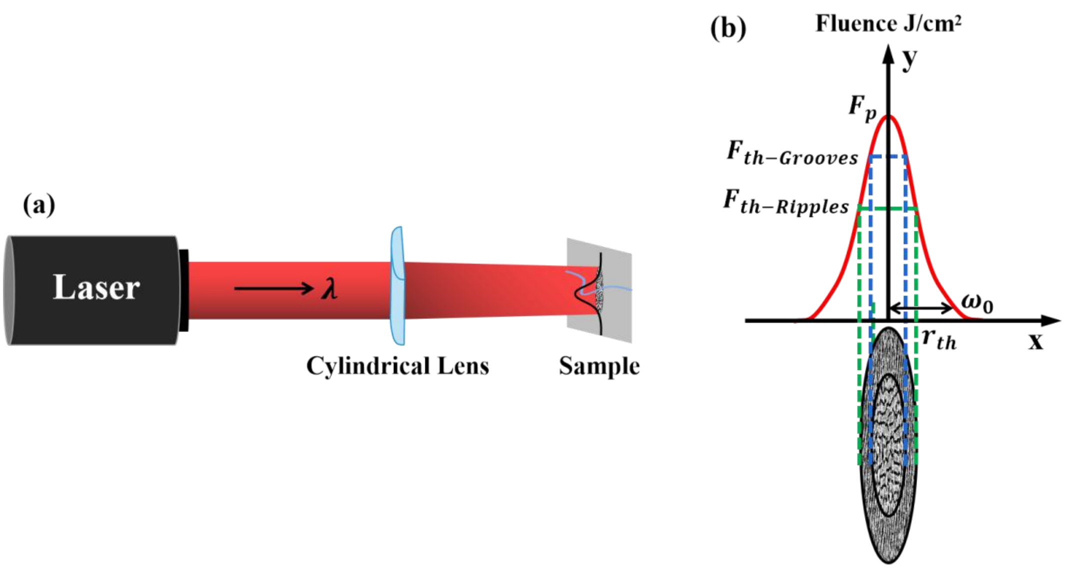

Fig. 2.7 (a) Representation of the Gaussian distribution along the surface of the sample with a laser beam focused by a cylindrical lens. (b) Schematic representation of the fluence of a Gaussian laser beam with a cylindrical lens; in particular, two different fluences were marked for the two different regions visible on a crater produced by a laser beam on the surface of a silicon sample.

2.4 Conclusions

This chapter mainly reports a summary of the experimental methods and equipments, including a brief description of the laser systems and accessories, the methods of using optical, scanning electron and atomic force microscopes, and the instructions of the related software for image processing. A theoretical analysis of the relationship between the features of shallow craters formed on the sample surface and the fluence spatial profile of the beam after focusing with spherical and cylindrical lenses was also illustrated to obtain the formulas and methods to estimated process parameters like, beam waist, threshold energy and threshold fluence.

Bibliography

[1] C. Momma, S. Nolte, B. N. Chichkov, F. Alvensleben, A. Tünnermann. Precise laser ablation with ultrashort pulses. Appl. Surf. Sci. 109 (1997) 15-19. https://doi.org/10.1016/S0169-4332(96)00613-7.

[2] A. Y. Vorobyev, C. Guo. Direct femtosecond laser surface nano/microstructuring and its applications. Laser Photonics Rev. 7 (2013) 385-407. https://doi.org/10.1002/lpor.201200017.

[3] M. Domke, V. Matylitsky, S. Stroj. Surface ablation efficiency and quality of fs lasers in single-pulse mode, fs lasers in burst mode, and ns lasers. Appl. Surf. Sci. 505 (2020). https://doi.org/10.1016/j.apsusc.2019.144594.

[4] F. Courvoisier, J. Zhang, M. K. Bhuyan, M. Jacquot, J. M. Dudley. Applications of femtosecond Bessel beams to laser ablation. Appl. Phys. A: Mater. Sci. Process. 112 (2013) 29-34. https://doi.org/10.1007/s00339-012-7201-2.

[5] J. M. Liu. Simple technique for measurements of pulsed Gaussian-beam spot sizes. Opt. Lett. 7 (1982) 196-198. https://doi.org/10.1364/OL.7.000196.

[6] J. JJ. Nivas, S. He, Z. Song, A. Rubano, A. Vecchione, D. Paparo, L. Marrucci, R. Bruzzese, S. Amoruso. Femtosecond laser surface structuring of silicon with Gaussian and optical vortex beams. Appl. Surf. Sci. 418 (2017) 565-571. https://doi.org/10.1016/j.apsusc.2016.10.162.

[7] U. Keller. Ultrafast Lasers - A Comprehensive Introduction to Fundamental Principles with Practical Applications. Springer (2021). https://doi.org/10.1007/978-3-030-82532-4_5.

[8] C. Rullière. Femtosecond Laser Pulses - Principles and Experiments. Springer (2005).

[9] D. B. Murphy. Fundamentals of light microscopy and electronic imaging. John Wiley & Sons (2002).

[10] Y. Leng. Materials characterization: introduction to microscopic and spectro-scopic methods. John Wiley & Sons (2008).

[11] ZEISS Sigma FE-SEM for High-Quality Imaging & Advanced Analytical Microscopy. https://www.zeiss.com/microscopy/en/products/sem-fib-sem/sem/sigma.html.

[12] ImageJ - Image processing and analysis in Java. https://imagej.nih.gov/ij/.

[13] Gwyddion - A modular program for SPM (scanning probe microscopy) data visualization and analysis. http://gwyddion.net/.

[14] J. Bonse, S. V. Kirner, J. Krüger. Laser-Induced Periodic Surface Structures (LIPSS). Handbook of Laser Micro- and Nano-Engineering (2020). https://doi.org/10.1007/978-3-319-69537-2_17-2.

[15] J. JJ. Nivas, S. He, A. Rubano, A. Vecchione, D. Paparo, L. Marrucci, R. Bruzzese, S. Amoruso. Direct Femtosecond Laser Surface Structuring with Optical Vortex Beams Generated by a q-plate. Sci. Rep. 5 (2015) 17929. https://doi.org/10.1038/srep17929.

[16] Atomic Force Microscopy (WITEC - Alpha300 RAS). https://raman.oxinst.com/products/correlative-microscopes/raman-afm-alpha300ra.

Chapter 3

Femtosecond laser surface structuring of silicon

This chapter deals with femtosecond (fs) laser surface structuring of a silicon target surface exploring in detail the following two aspects: i) features of the surface structures generated on a target moving at different scanning velocities (dynamic configuration) under the irradiation by a 1030 nm fs laser beam; ii) effects of repetition rate, in the range 0.01-200 kHz, on the surface structures generated in vacuum and in air, in static irradiation conditions. In the former case, our findings evidence clear trends of the morphological features of the surface structure on the effective number of laser pulses as well as the existence of interesting differences in their characteristics when processing occurs at the same value of the accumulated laser fluence dose achieved by appropriate selection of laser pulse energy and scanning speed. In the latter case, a clear difference in the morphology of the surface structures generated in vacuum and air is ascertained, addressing a change in the laser-target energy coupling at the higher pulse repetition rates.

Scanning electron microscopy (SEM) analysis of the shallow linear craters produced in different experimental conditions allows characterizing the dependence of threshold fluence for the formation of the surface structures (ripples and grooves) as well as the variation of their spatial period. Firstly, due to the choice of the high velocities, the dynamic lines are stable and uniform, but with low peak fluence compared to static spots even with the same number of effective pulses. In addition, a more granular character of the grooves makes recognizable a clear pattern of underlying ripples in dynamic configuration. The observed behavior is rationalized in terms of the effects induced by the presence of nanoparticles debris as well as of a plume shielding occurring at repetition rates larger than 10 kHz in air. Both such effects are, indeed, hindered for vacuum irradiation conditions. Hence, our experimental findings allow gaining clear evidence of the impact of plume shielding and nanoparticles coverage on the laser material processing in air at high repetition rates and of their rather scarce influence in vacuum. These observations, in turn, provide new useful insights in the field of fast laser processing essentially required in industrial applications.

3.1 Introduction

In the present experiments, silicon was selected because it represents a case study in the field of Laser-Induced Periodic Surface Structures (LIPSS) and for its wide significance in technological applications. In particular, we analyze in detail the following two interesting issues:

- The features of the surface structures generated on a target moving at different scanning velocities (dynamic configuration) under the irradiation by a 1030 nm fs laser beam [1-16]. The formation of ripples and grooves is investigated, addressing the variation of the threshold fluence for their formation as well as the dependence of their spatial period on two experimental parameters, namely the effective number of laser pulses and the laser fluence [17-18]. Moreover, we analyze the features of ripples and grooves generated with a similar accumulated laser fluence dose achieved by appropriate selection of the scanning speed and laser pulse energy. Our experimental findings indicate a behavior rather similar to that observed for static irradiation configurations for the threshold fluence and spatial periods dependence on the effective number of laser pulses, whereas interesting differences are evidenced for the degree of regularity of the surface structures generated at the same accumulated fluence dose.
- The effects of the laser pulse repetition rate, in the range 0.01-200 kHz, on the surface structures generated in vacuum and in air, in static irradiation conditions. Previous studies at high repetition rate suggested a possible role of thermal accumulation and plume shielding effects [19-25]. For instance, Fraggelakis *et al*. evidenced the role of thermal accumulation during laser texturing of stainless steel at repetition rates from 100 kHz up to 2 MHz [19], whereas Sedao *et al*. observed plume shielding during additive and subtractive laser structuring of metallic targets at 250 kHz [26]. Nonetheless, studies devoted to establishing the role of the physical processes at operation in fs laser surface structuring carried out at high repetition rates remain still scarce and the subject deserves further investigations. Hereafter, it will be shown that a clear difference occurs for processing at repetition rates larger than about 10 kHz in vacuum and air, which allow also addressing an interesting change in the laser-target energy coupling in the two cases.

In the following, we will first discuss the features of the structuring process in dynamic irradiation conditions in section 3.2; then, in section 3.3 the results of the processing in air and vacuum in static irradiation conditions will be presented.

3.2 Femtosecond laser surface structuring of silicon in dynamic irradiation conditions

Laser surface structuring of an intrinsic (100) silicon target, in air, was carried out by using a Yb:KGW laser source providing linearly polarized, ~180 fs pulses at a wavelength of λ~1030 nm with a repetition rate $\mathrm{RR} = 1\ \mathrm{kHz}$. The laser beam was focused on the target surface by a plano-convex lens with a nominal focal length $\mathrm{f} = 20\ \mathrm{cm}$. The target was attached to the linear translation stage that could be moved perpendicularly to the direction of the impinging laser beam. Target irradiation was carried by continuously translating the target at a fixed velocity $\mathrm{v_s}$.The laser polarization direction was parallel to the scanning direction. Morphological characterization of the irradiated surface was carried out by using the field emission scanning electron microscope (FE-SEM – Zeiss Σigma). Then, two-dimensional Fast Fourier Transform (2D-FFT) of the SEM images was carried out to gain information on the characteristic features of the surface structures [4, 17, 27].

The laser beam spot size on the target was obtained by analyzing the variation of the size of shallow linear craters produced on the target surface as a function of the laser pulse energy, as discussed in chapter 2. For the dynamic configuration used here, the energy variation of the width, ω, of lines produced at thirteen different values of the scan velocity, v_s, was analyzed by evaluating the slope of ω^2 on $ln\,(E)$. In addition, in some cases the spot size was also estimated by producing shallow circular craters on a static target and analyzing the energy variation of the crater area. In all cases, the results were consistent with a Gaussian beam profile and the estimated laser spot size, at $1/e^2$ of the maximum intensity, was $\omega_0 = (25 \pm 1)$ µm. In the experiments, the laser energy fluctuations were lower than 5%.

3.2.1 Role of the effective pulse number, N_{eff}, and the accumulated fluence dose, $\mathbf{F_d}$

For a laser beam with a Gaussian spatial intensity profile, the laser fluence distribution is

$$F(x,y) = F_p exp\left[-\,2(x^2{+}y^2)/\omega_0^2\right], \tag{1}$$

where $F_p = \frac{2E}{\pi\omega_0{}^2}$ is the peak fluence. As displayed in Fig. 3.1(a), in dynamic configuration the successive laser pulses partially overlap during the target scanning eventually producing a line of total length L. The corresponding total number of pulses per line is

$$N_{tot} = L\frac{RR}{v_s}, \quad (2)$$

where RR is the repetition rate and v_s the scan speed. In the experiments, L was set to 1 mm. In this configuration, the effective pulse number

$$N_{eff} = 2\omega_0\frac{RR}{v_s} \quad (3)$$

or the pulse-to-pulse overlap factor

$$O = \left(1 - \frac{1}{N_{eff}}\right) \quad (4)$$

are typically used as processing parameters. Therefore, each position (x, y) of the resulting linear crater receives an accumulated fluence dose

$$F_d(x,y) = F_p \sum_{k=1}^{N_{tot}} exp\left\{-2\left[\left(x-k\frac{V_s}{RR}\right)^2+y^2\right]\Big/\omega_0^2\right\} = \eta_O(x)F_p exp\left(-2\frac{y^2}{\omega_0^2}\right), \quad (5)$$

where (y=0 corresponds to the center of the linear crater). Hence, the spatial distribution of the accumulated fluence presents a Gaussian profile along the y-direction. This, in turn, explains why the energy variation of the width of the linear crater provides a reliable estimate of the Gaussian beam radius ω_0 on the target.

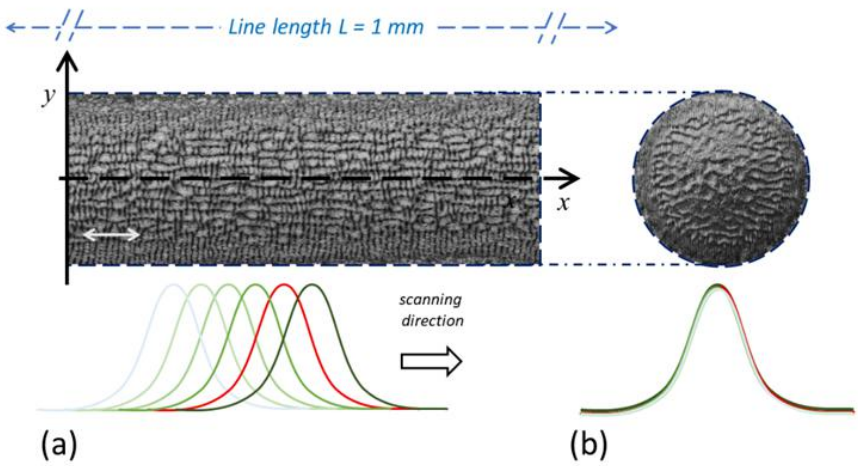

Fig. 3.1 The upper panels in parts (a) and (b) show two SEM images of the silicon target surface after irradiation in dynamic and static configuration with energy of the laser pulses E~10 μJ. The shallow line in panel (a) was generated on a scanning target moving at a velocity V_s=0.25 mm/s, for an effective number of pulses N_{eff} = 200, whereas the circular crater in panel (b) was produced on a static target by a sequence of N=200 pulses. The cartoons in the lower panels of part (a) and (b) sketch the laser profiles in the dynamic and static irradiation configurations, respectively. The double-headed arrow in panel (a) illustrates the laser pulse polarization direction.

The Gaussian spatial profile of the fluence dose along the y-direction, at $x = L/2$, normalized to its maximum value, is shown as a solid line in Fig. 3.2(a). It is worth comparing it with the one corresponding to static irradiation conditions with a number of pulses $N =$

N_{eff}, displayed as a dashed line in Fig. 3.2(a). In the static case, each position (x, y) of the target surface receives a total fluence dose equal to the number of pulses N times the local laser fluence $F(x, y)$. Fig. 3.2(a) shows that for $N = N_{eff}$ the peak value in the static case is about 1.6 times larger than that corresponding to a scanning target hit by the same number of effective pulses. The different fluence dose delivered leads to morphological differences of the target surface, as clearly observed in Fig. 3.1. As an example, Figs. 3.1(a) and 3.1(b) show the two SEM images corresponding to the dynamic and static irradiation conditions with N_{eff}=200 (V_s=0.25 mm/s) and N=200, respectively, for a pulse energy E=10 μJ. For static irradiation (panel (b)), the ripples are mainly confined at the craters edge whereas the grooves cover an area with a diameter equal to ~80% of that of the shallow crater. Instead, the line generated by target scanning is covered by grooves for a length that is ~55% of its width along the *y*-direction. This is coherent with the general features that grooves form in the region irradiated by larger fluence [17, 29-30]. Moreover, some differences are discernible in the finer morphological features of the grooves generated in the two cases. In fact, in the dynamic irradiation mode a more granular character of the grooves makes recognizable a clear pattern of underlying ripples. This effect is typical of grooves generated under dynamic configuration [31].

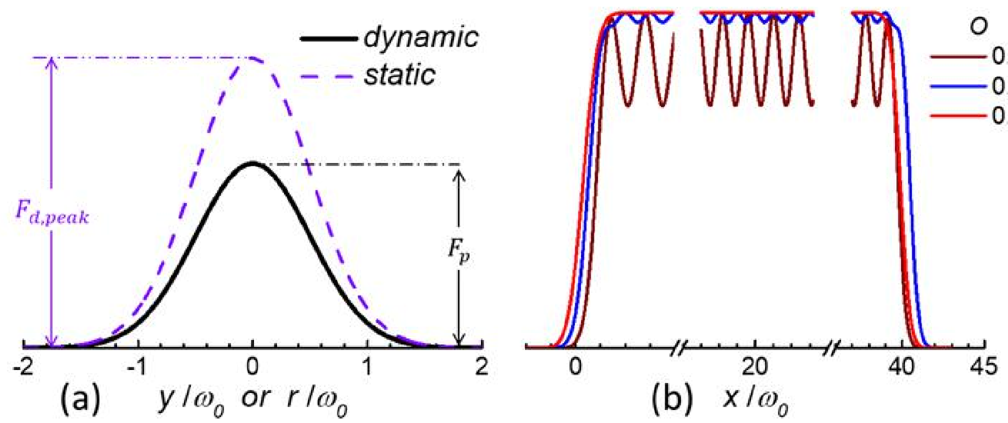

Fig. 3.2 Panel (a) shows the spatial profile of the fluence dose along the y-direction for dynamic irradiation (solid line) and along the diameter for static irradiation, respectively, addressing the larger value achieved in the static case. Panel (b) reports the profiles of $\eta_O(x)$ for various values of the overlap factor O; Each profile is normalized to its maximum value. The variables on the horizontal axis are normalized to the Gaussian beam radius ω_0.

The function $\eta_O(x)$ represents the profile of the fluence dose along the scanning direction and depends on the pulse overlap [31-33]. Fig. 3.2(b) reports some examples of $\eta_O(x)$ profiles, normalized to their maximum value, for three different values of the overlap factor O. In all cases, the profile reaches a steady state behavior after a scan length of few times ω_0. However, at low values of the overlap factor (O<0.5), $\eta_O(x)$ displays oscillations in the central region of the line, which progressively damp down as O increases. In our experiments, the minimum value of the overlap factor is $O_{min} = 0.98$, therefore the fluence dose is uniform along the produced line except for the regions very close to the initial and final edges of the scanned line. Accordingly, the morphology of the surface along the line is rather uniform, as observed in the SEM image of Fig. 3.1(a).

3.2.2 The variation of the threshold fluence and the period of the LIPSS in dynamic irradiation

The morphological features of the ripples and grooves generated at different values of the scanning velocity, V_s, were obtained by SEM measurements. The upper panels of Fig. 3.3 report exemplificative SEM images of a portion of the linear craters produced at three different beam scanning velocities, for a pulse energy of 6 μJ. The SEM images clearly evidence a different morphology of the periodic surface structures, at the same pulse energy, as a function of V_s that essentially determines the number of effective pulses N_{eff}. The lines in Fig. 3.3 were produced at V_s equal to 0.2 mm/s, 0.4 mm/s, and 1 mm/s and the corresponding values of N_{eff} are 250, 125 and 50, respectively. A significant difference in the ripples and grooves morphology can be observed in each case. At V_s=0.2 mm/s (see Fig. 3.3(a)), well-developed grooves cover the central part of the linear crater, whereas ripples are mostly confined at its edges. Moreover, a noticeable deposition of nanoparticles forms outside the shallow linear crater as seen in the inset of panel (a) displaying a zoomed view of the crater edge. The predominance of grooves can also be ascertained for V_s=0.4 mm/s, in panel (b). As the scanning speed increases to V_s=1 mm/s (see panel (c)), the laser irradiated track is mainly decorated with ripples and a soft presence of grooves is only recognizable towards the line center. Moreover, the presence of nanoparticles is considerably reduced at higher scanning speed and becomes minimal at V_s=1 mm/s, as can be seen from the zoomed view of the structured track edge in the inset of panel (c).

Fig. 3.3(d) reports the dependence of the threshold fluence, F_{th}, for the generation of ripples and grooves on the effective number of pulses, N_{eff}. A clear reduction of F_{th} with N_{eff} is observed for both ripples and grooves, with a F_{th} reduction of ~70% as N_{eff} passes from 50 to 250. The progressive decrease of the threshold fluence is typically indicated as incubation effect [34]. The incubation effect also implies a gradual increase of the width of the linear crater and a shift in the location of the LIPSS, with grooves decorating the center and ripples located towards the periphery. The shaded area between ripples and grooves threshold fluences identifies the fluence region for the formation of ripples at a given value of N_{eff}. Panel (e) of Fig. 3.3 reports the data in the form $ln[N_{eff}F_{th}(N_{eff})]$ vs $ln[N_{eff}]$ [5, 35] for ripples (circles) and grooves (squares). The solid lines in panel (d) display fit of the experimental data with the dependence $F_{th}(N_{eff}) = F_{th}(1)N_{eff}^{\xi-1}$, where ξ is the incubation factor. The coefficient ξ depicts the degree of incubation, with a value of 1 corresponding to a threshold fluence independent of the number of pulses, whereas a lower value characterizes the inter-pulse feedback effects involved in the formation of LIPSS by multi-pulse laser irradiation. The fitting procedure yields an incubation factor ξ=(0.78±0.04) for both ripples and grooves. Various values of the incubation factor for ripples and grooves have been reported for silicon samples irradiated with different laser pulses. Mezera *et al*. reported a value ξ=(0.75±0.02) for n-doped (100) crystalline silicon targets irradiated by pulses of 6.7 ps at a wavelength of ≈ 1030 nm, in static irradiation conditions. Moreover, Allahyari *et al*. observed ξ = (0.78±0.04) for ripples and ξ = (0.77±0.03) for grooves during irradiation of intrinsic (100) crystalline silicon samples by pulses of ~180 fs at ≈1030 nm. These values are very consistent with the ones estimated here for a scanning silicon target, hence suggesting that similar multi-pulse feedback effects are active in both static and dynamic irradiation conditions.

We turn now to the variation of the period Λ of ripples and grooves on the effective pulse number, N_{eff} , and accumulated fluence dose peak, $F_{d,peak} = max\,\{F_d(x,y\}$. $F_{d,peak}$ corresponds to the peak value of the Gaussian spatial profile along the *y*-direction shown in Fig. 3.2(a) as a solid curve. The values of Λ were obtained for three values of the pulse energy E, namely 6, 8 and 10 μJ. The period was estimated by applying 2D-FFT to the SEM images of a central portion of the linear craters produced at thirteen different values of the scan velocity V_s, namely 0.15, 0.2, 0.25, 0.3, 0.35, 0.4, 0.45, 0.5, 0.55, 0.57, 1 mm/s. From the measurement of the spatial frequency of the typical features observed in the reciprocal space [17, 36-37], the value of Λ and its uncertainty were estimated. The obtained results are displayed in Fig. 3.4.

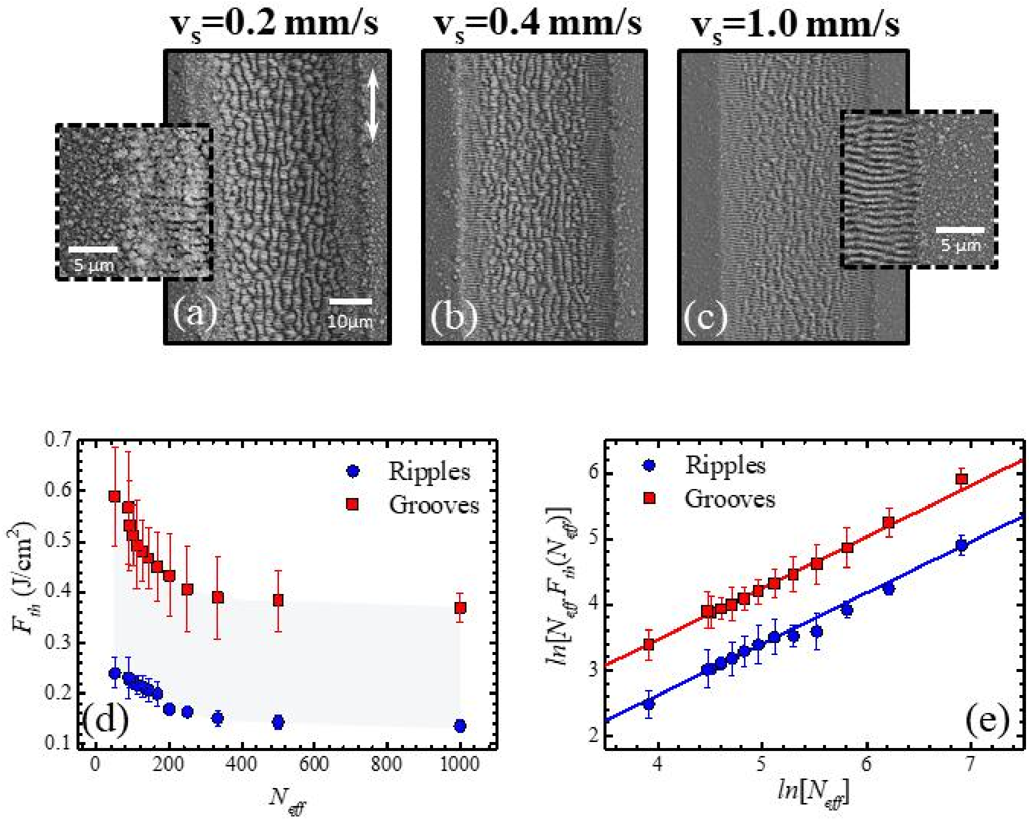

Fig. 3.3 Panels (a) reports three exemplificative SEM images for V_s equal to 0.2, 0.4 and 1 mm/s, respectively at a pulse energy E=6 μJ; the corresponding values of N_{eff} are (a) 250, (b) 125 and (c) 50, respectively. The insets of panels (a) and (c) display zoomed views of the crater edge. Panel (d) shows F_{th} vs N_{eff} for ripples (circles) and grooves (squares); the light-gray shaded region between ripples and grooves threshold fluences identifies the are for the formation of ripples, whose width remains almost unchanged as N_{eff} rises. Panel (e) reports $ln\left[N_{eff}F_{th}\left(N_{eff}\right)\right]$ vs $ln\left[N_{eff}\right]$ for ripples (circles) and grooves (squares); the lines are linear fit corresponding to an incubation factor of ξ=(0.78±0.04).

Considering first ripples, the experimental data of Fig. 3.4(a) clearly evidence a progressive reduction of Λ as a function of N_{eff}. Moreover, the change of the laser pulse energy E has negligible influence on the ripples period and the experimental data are all located within the narrow region highlighted in yellow in Fig. 3.4(a). This is in good agreement with both previous experimental observations and theoretical predictions on ripples formed on a silicon target surface under static irradiation conditions [31, 36, 38-40]. The progressive reduction with number of pulses is a general feature of ripples formation that is confirmed also in the dynamic irradiation conditions. This, in turn, suggests that N_{eff} is a reliable, empirical parameter for such an experimental situation [32-33], even if there is not yet a microscopic theory for LIPSS formation capable of including laser beam scanning effects [17, 31]. In particular, the decreasing tendency of the period on the pulse number has been originally rationalized by considering the interference between the impinging laser radiation and surface plasmon polaritons on the target surface [41], as discussed in chapter 1. In such an approach, the reduction of the period Λ is ascribed to a progressive shift towards lower values of the surface plasmon wavelength as the depth of the ripples increases with the pulse number [41]. However, this behavior was also confirmed by theoretical simulations taking into account hydrodynamics, molten material dynamics and resolidification effects [31, 40]. The scarce dependence on the pulse energy E was previously addressed in experiments carried out with both Gaussian and Vector Vortex laser beams [38-39, 42-43]. It can be ascribed to the fact that the range of fluence values for ripples formation, at a fixed N_{eff}, remains almost unchanged as shown in Fig. 3.3(d). As the pulse energy varies, the pulse peak fluence changes and the range of fluence values for ripples generation moves progressively towards the line periphery, as observed in panels (a-c) of Fig. 3.3, thus making the dependence of the period Λ on the pulse energy E almost negligible.

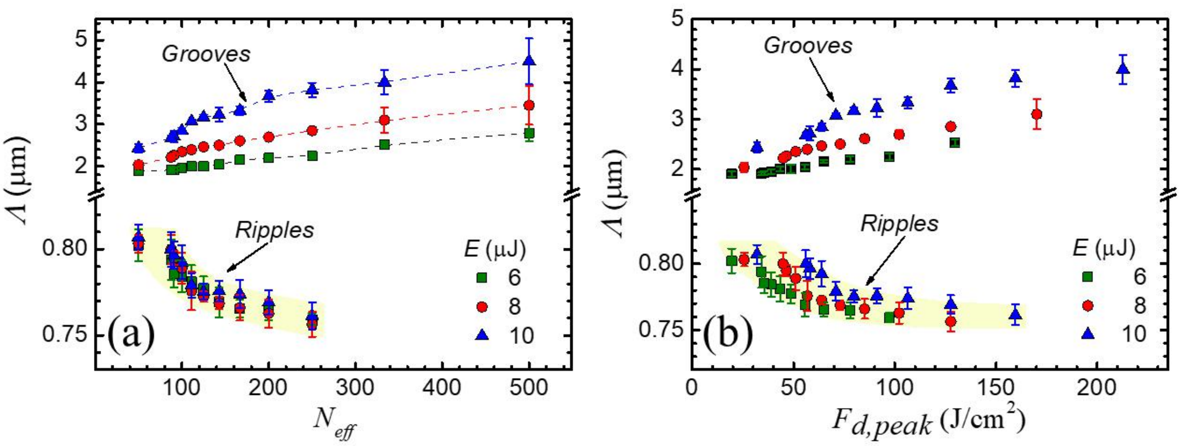

Fig. 3.4 Variation of the ripples and grooves period, Λ, as a function of the effective pulse number, N_{eff} (panel (a)), and accumulated fluence dose peak $F_{d,peak}$ (panel (b)), for three different values of the single pulse energy E, namely 6.1, 8 and 10 μJ; the. The vertical axes present a break that allow displaying both ripples and grooves period in the same panel.

For the grooves, the experimental data of Fig. 3.4(a) show a rather clear increasing trend of the period with N_{eff} and laser pulse energy E, again in agreement with previous observations obtained in static conditions. In fact, an increase of grooves period with pulse number was reported earlier both in experiments and simulations on silicon and steel irradiated by fs laser pulses [30-31, 38-39, 44]. Recently, this aspect has been corroborated by theoretical simulations addressing the role of hydrothermal waves in the process of grooves formation [31, 44]. Such a feature is also confirmed in silicon under dynamic irradiation conditions, even if the modeling of such an experimental situation has still not yet been developed [31].

The accumulated fluence dose represents another parameter not yet fully explored and assessed [17, 32-33]. Fig. 3.4(b) displays the dependence of the ripples and grooves periods on $F_{d,peak}$. Similar general trends of Λ on $F_{d,peak}$ are observed also in this case, but data points corresponding to the ripples period results more scattered even remaining comprised in a restricted region evidenced in yellow in Fig. 3.4(b). The grooves period still varies with the pulse energy at similar values of $F_{d,peak}$. This, in turn, seems to suggest that the final features of the surface structures do not depend only on the total fluence accumulated but on the effective way it is delivered to the target, thus addressing the relevant role of the multi-pulse feedback effects on grooves formation whose full clarification still deserve investigation. Such an aspect is further analyzed in the next section.

3.2.3 LIPSS generation at same accumulated fluence dose by optimizing of the scanning velocity and pulse energy

Linear craters were produced for three different experimental conditions resulting in the same accumulated fluence dose peak, within the uncertainty, namely $F_{d,peak}$=(56±1) J/cm^2. This was achieved by using the following couples of experimental parameters (v_s, E): (0.35 mm/s, 6.1 μJ), (0.45 mm/s, 8.0 μJ) and (0.57 mm/s, 10 μJ). SEM images of a portion of the linear shallow craters produced in these experimental conditions are shown in panels (a-c) of Fig. 3.5. The corresponding periods of ripples and grooves produced in these experimental conditions are summarized in Table 1. 2D-FFT of the SEM images of Fig. 3.5(a-c) were obtained by using *Gwyddion* image analysis software [45]. The spectral bi-dimensional images are shown in panels (d-f) and allow a direct visual comparison of the spectral modulation in frequency domain of the periods of ripples and grooves decorating the linear craters. The peaks corresponding to the spatial period of the two surface features are marked in the 2D-FFT images: the two sickle shaped regions at larger frequency aligned along the vertical axis are characteristic of the presence of ripples, whereas the two lobes disposed along the horizontal axis come from the surface modulation due to the grooves [17, 36, 46].

The 2D-FFT maps in panels (d-f) of Fig. 3.5 display rather similar features suggesting a comparable overall morphology of the surface. Nevertheless, some differences do exist. For example, the ripples signal in panel (d), corresponding to the case of larger scanning velocity and laser pulse energy, shows a higher angular spread of the spatial frequencies as marked in the 2D-FFT map. This frequency spreading progressively reduces going towards lower scanning velocity and pulse energy, as shown in panels (e) and (f) of Fig. 3.5. The spatial frequency angular spread gives an indication about the inherent bending and bifurcation of the ripples. Hence, it can be used as an evaluation of the degree of regularity or uniformity of the LIPSS [9, 17-18, 33, 37].

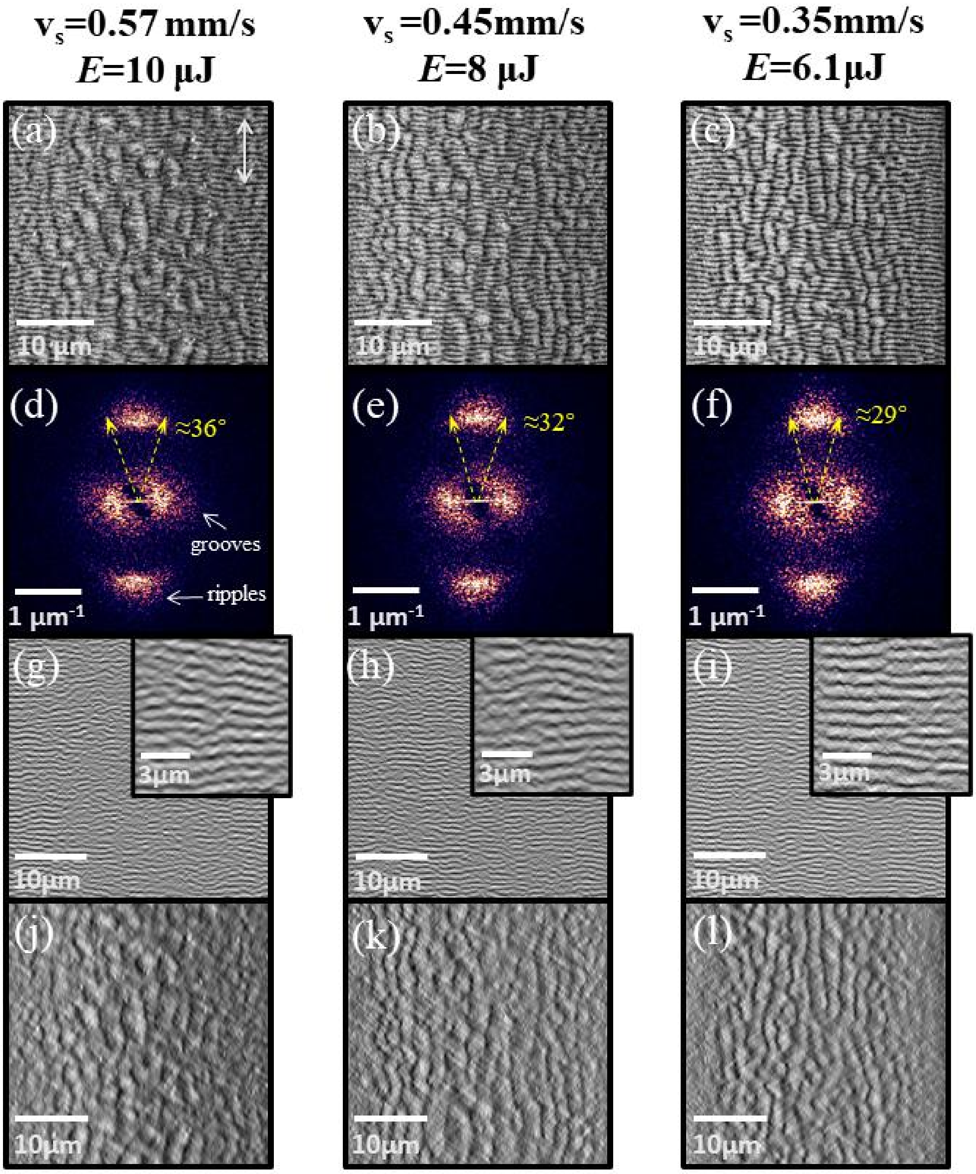

Fig. 3.5 Panels (a-c) display SEM images of a portion of the linear shallow craters produced with the same accumulated fluence dose peak $F_{d,peak}$=(56±1) J/cm^2. The double headed arrow in panel (a) marks the laser beam polarization direction. Panels (d-f) are 2D-FFT maps of the upper SEM images. Panels (g-i) are morphology maps in the real space generated through 2D-IFFT by selecting only the spectral frequency features associated to ripples. The insets show zoomed views of the ripples surface modulation. Panels (j-l) are morphology maps in the real space generated through 2D-IFFT by selecting only the spectral frequency features associated to grooves.

An easier visualization of such effects can be gained by using the 2D inverse FFT (2D-IFFT) of the spectral frequency peaks of any specific surface structure. 2D-IFFT maps were generated by using the filtering method offered by *Gwyddion* software [45]. The reconstructed maps of the surface spatial modulation corresponding to ripples and grooves are separately displayed in panels (g-i) and (j-l) of Fig. 3.5, respectively. The 2D-IFFT analysis allows a more direct visualization of the individual surface features associated to the intense peaks of the Fourier spectra reported in panels (d-f). As for ripples, the insets of panels (g-i) display zoomed views of their spatial modulation recovered from selective 2D-IFFT. A better regularity of the spatial modulation is seen in panel (i). This regularity progressively reduces passing to panel (h) and (g), suggesting the formation of more uniform ripples at lower pulse energy (6.1 μJ) and scanning speed (0.35 mm/s), for a comparable accumulated fluence dose peak value. As for the grooves, the 2D-IFFT map reported in panels (j-l) also show a tendency towards more defined grooves characterized by a better degree of alignment along the laser beam polarization direction and longer length without breaking. Consequently, at a fixed accumulated dose lower values of the scanning speed and laser energy seem to be beneficial to the degree of regularity of the produced LIPSS, within the limited statistics of the three cases analyzed here. Optimization methods have been mainly considered for ripples in previous studies [9-10, 32-33, 47]; however, grooves might also deserve further consideration.

Table 1. Period Λ of ripples and grooves generated in dynamic configurations with an accumulated fluence dose peak $F_{d,peak}$ =(56±1) J/cm^2 achieved by selecting three couples of scanning velocity V_s and pulse energy E values.

Parameters	Period Λ (μm)	
v_s (mm/s) ; E (μJ)	Ripples	Grooves
0.35 ; 6.1	0.77±0.01	2.04±0.04
0.45 ; 8	0.78±0.01	2.39±0.05
0.57 ; 10	0.80±0.03	2.67±0.06

The analysis reported above seems to indicate that even if a similar accumulated fluence dose provides rather comparable general features of the produced LIPSS, lower energy and scanning speed can be more beneficial to the degree of regularity of the ripples and grooves generated in multi-pulse laser surface structuring. This might seem in some contradiction with the results of Gnilitskyi *et al.*, who reported high regularity ripples produced on undoped, (111) silicon crystals in the strong ablation regime associated to the use of energetic infrared fs pulses (wavelength of 1030 nm, pulse duration of ~213 fs, single peak fluence of ~ 1.6 J/cm^2) with a small overlap factor (O~0.7, i.e. number of overlapped pulses of 3 or 4) at very high repetition rate (600 kHz) [10]. More generally, this might indicate the existence of different regimes associated to the wide playground due to the several experimental parameters involved in the process of laser surface structuring over a large area (e.g., scanning speed, laser fluence, repetition rate, pulse overlap, and so forth). This fact on the one hand offers the wide range of possibilities already demonstrated for fs laser surface structuring, on the other hand claims for an even deeper understanding of the various mechanisms involved in the formation of LIPSS for the diverse novel regimes achievable with the many laser sources available nowadays, also in view of the progressive transfer towards industrial fields of this fruitful material processing approach.

3.3 Ultrafast laser surface irradiation of silicon at high repetition rate in vacuum and air

The experiments illustrated hereafter were carried out by exploiting the Yb:KGW system (Pharos, Light Conversion) presented in chapter 2. It delivers laser pulses with a duration of ≈180 fs at a wavelength of ≈1030 nm with maximum values of the repetition rate of 200 kHz. The laser system is equipped with a pulse picker that allows selecting a sequence of N laser pulses, at a given energy E_p, for any value of the repetition rate between single shot and 200 kHz. This pulse selection method guarantees a good consistency of the features of the output laser beam during the whole experiment, within their typical statistical fluctuations, since the laser system is operated always at its maximum repetition rate. However, the maximum laser pulse energy E_p that can be used to address the role of the repetition rate in this experimental configuration cannot exceed the maximum value achievable at 200 kHz.

The target was a piece of intrinsic, (100) crystalline silicon cut from a wafer with a resistivity larger than 200 Ω cm and a thickness of ≈400 μm (Siltronix). The target was located in a vacuum chamber at a residual air pressure of $\approx 10^{-3}$ mbar. The sequence of N linearly polarized pulses was focused on the target, at normal incidence, by means of a plano-convex lens with a nominal focal length of 20 cm. An XY-translation stage was used to move the sample after each irradiation, thus obtaining a series of shallow craters generated by a given number of pulses N at a selected value of the repetition rate RR. The laser spot size was estimated by measuring the variation of the crater dimensions at different values of the pulse energy, as outlined in chapter 2, resulting for the various values of the repetition rate equal to $\omega_0 \approx 33\ \mu m$.

The general features of the irradiated sample surface were observed by optical microscopy and the morphological characteristics of selected spots were successively obtained by means of the field emission scanning electron microscopy FE-SEM. For the sake of comparison, a similar experiment was also carried inside the vacuum chamber but in ambient air pressure to keep the rest of experimental configuration unaltered.

The functionality of LIPSS in air is usually affected not only by the grating-like surface topography but also by its specific surface chemistry (e.g. oxidation), which depends on the types of LIPSS [48-49]. The LIPSS type considered in my research is mainly LSFL-I, generated from localized laser-induced melting and rapid solidification in an amorphous material state [50], which do not specifically rely on surface oxidation effects but may be accompanied by it upon laser-processing in an air environment.

3.3.1 Differences on surface structures for irradiation in vacuum and air, at high repetition rate

Fig. 3.6 reports an example of the SEM images of the silicon surface after irradiation with a sequence of N=100 laser pulses for two values of the repetition rate RR, namely 1 kHz and 200 kHz, for irradiation in vacuum (panels (a) and (b)) and ambient air (panels (c) and (d)). The pulse energy is $E_p \approx 14$ μJ, and the corresponding peak fluence is $F_p \approx 0.8$ J/cm^2.

We analyze first the morphological features of the target surface produced by irradiation in vacuum. The SEM images of panels (a) and (b) in Fig. 3.6 show the formation of a shallow crater, decorated with LIPSS, covering an area with a slightly elliptical spot of major axis ≈37 μm along the horizontal direction (polarization direction) and ≈33 μm along the vertical direction, for both values of the repetition rate. As can be seen from panel (a) and (b) of Fig. 3.6, the formation of elliptically shaped structured spot in silicon is a typical behavior when the laser processing takes place at reduced pressure and results from the enhancement of LIPSS formation along the direction of laser polarization in comparison to that of perpendicular direction [51-52]. Ripples with a subwavelength period (≈892±69 nm at 1 kHz and ≈887±59 nm at 200 kHz) and an orientation perpendicular to the laser polarization cover the major part of the generated crater. Instead, the central region irradiated by the part of the beam at higher fluence displays coarser surface structures characterized by a larger dimension ranging from few to several μm. The shape of the coarser surface structures and their preferential elongation might suggest their possible origin as related to the merging of two or more ripples induced by the larger values of the laser fluence in the central part of the irradiated area. These coarser elongated structures seem to be broken by a further modulation parallel to the laser polarization with a characteristic scale length of ≈3.5 μm, as indicated by the yellow dashed lines in panels (a) and (b) of Fig. 3.6. Finally, the observed morphological characteristics are rather similar for both repetition rates of 1 kHz and 200 kHz, after irradiation with N=100 pulses in vacuum.

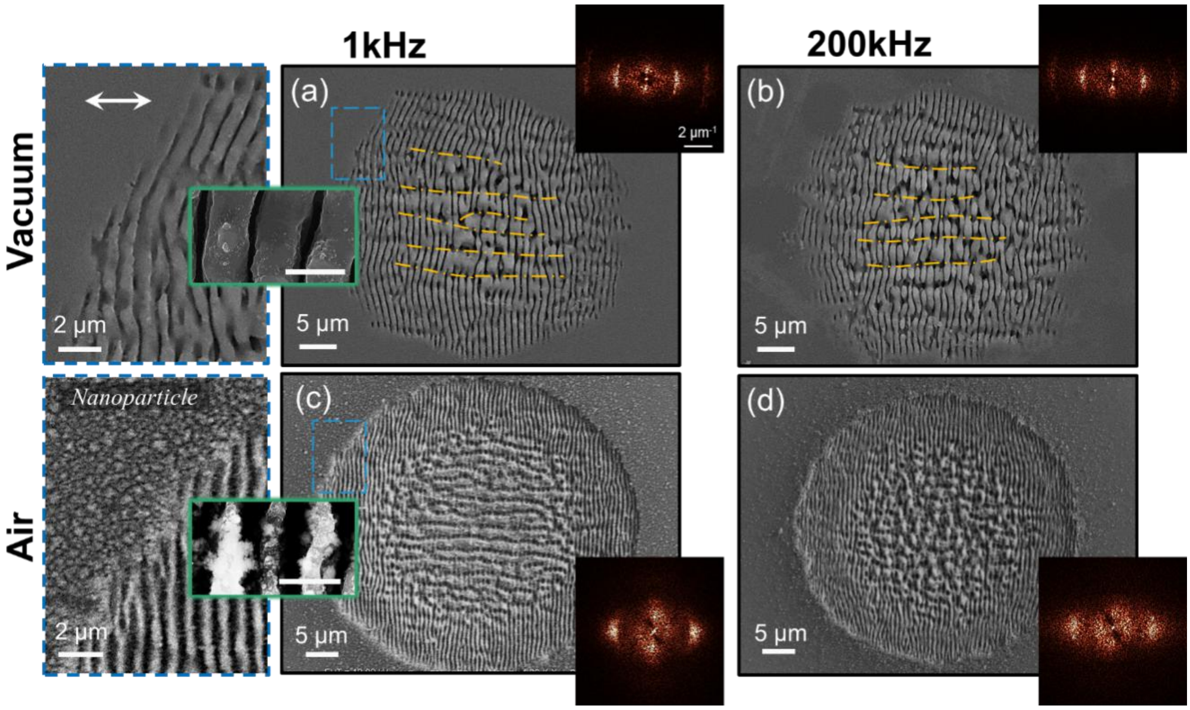

Fig. 3.6 SEM images of the Si target surface after irradiation with a sequence of N=100 pulses with a laser pulse fluence F_p≈0.8 J/cm^2. The upper panels refer to vacuum conditions for a repetition rate of (a) 1 kHz and (b) 200 kHz, respectively. Panels (c) and (d) refer to irradiation in air at (c) 1 kHz and (d) 200 kHz. The white double-headed arrow shows the incident laser pulse polarization. The dashed lines indicate the direction of a secondary modulation that seems to break the coarser surface structures covering the central region of the crater. The upper inset of panels (a-d) shows the 2D-FFT spectra generated from the corresponding SEM images giving a further indication about the surface features present in each case. The two panels of the left display zoomed views of the zones in the blue dashed boxes of panels (a) and (c), respectively. An image obtained at higher magnification showing fine morphological features of ripples formed in air and vacuum at 1 kHz are provided in between the extreme left panels and panels (a) and (d), highlighted in green color, in which the scale bar equals to 1 μm.

As for irradiation in air, we notice that the SEM images of the relatively circular craters displayed in panels (c) and (d)) of Fig. 3.6 evidence striking morphological variation with respect to those obtained in vacuum. A first difference is the significant presence of nanoparticle debris surrounding the shallow crater, as evidenced by the zoomed views of the target surface shown in the extreme left panels of Fig. 3.6. This debris is negligible for irradiation in vacuum; instead, in air, the nanoparticle debris is rather consistent due to the deposition on the sample surface of the ablated material induced by the confinement effect of the ambient atmospheric pressure [53-54]. The fine morphology of ripples in both conditions generated at 1 kHz are shown in the small panels highlighted in green color (in between the panels (a) and (c) and the corresponding two left panels), showcasing the presence of redeposited nanoparticle inside the crater. Two concentric regions covered by LIPSS can be identified within the shallow crater also for air. For both values of the repetition rate, a rippled region forming a ring extending from ≈15 μm to the crater periphery is observed. Instead, the central region (≈ 36% of the shallow crater area) displays some obvious changes with the repetition rate. The measured spatial period of ripples generated in the annular region of the spots shown in panel (c) and (d) are ≈726±46 nm, ≈736±51 nm, respectively. In fact, at 1 kHz well-defined supra-wavelength grooves with a spatial period of ≈ (2.0±0.2) μm and an orientation parallel to the laser polarization form in the central region hit by the most intense part of the beam, whereas at 200 kHz these surface structures are less differentiated and mostly replaced by more globular assemblies. In particular, the transition from rather well recognized grooves to the globular structures with only residual grooves-like remnants occurs at a repetition rate of about 20 kHz.

Analysis of surface structures shown in Fig. 3.6 are also carried out by means of 2D-FFT maps of the SEM images using *Gwyddion* software [45]. The 2D-FFT maps are provided as inset of the corresponding panels. The difference in the characteristic peaks in the 2D-FFT map, which are associated to the spatial period and preferential alignment of ripples and grooves in real space, shows the variation in the morphology of surface features generated in each irradiation condition. The peaks in the 2D-FFT map representing both surface structured are well-defined and confined in the case of a spot processed in vacuum due to the significantly reduced nanoparticles coverage present in this case for both pulse repetition rates.

Interestingly, even though peak fluence is the same, the diameter of the shallow crater in air is ≈50 μm, is about 30% larger than the average value of the spot diameter in vacuum. This suggests a more effective coupling of the laser energy for irradiation in air likely due to the enhancement of the absorption induced by the progressive covering with nanoparticle debris of the target surface [55-57]. Since the back-deposition of nanoparticles occurs both outside and within the nascent crater, one can expect an overall increase of the absorption, besides the contribution given by the surface structures, that can also enhance the light absorption efficiency through both variation of incidence angle and multiple reflections. A clear enhancement of the light absorbance of ≈70% is reported by Vorobyev *et al*. at 1055 nm in the case of silicon processed in air [57].

3.3.2 The variation of threshold fluence in air and vacuum

In an attempt to further characterize the aspect of the process above mentioned, we estimated the threshold fluences for the formation of the crater/ripples, F_{th}, and the generation of the surface structures decorating the central area of the irradiated spot, F^*_{th}, as depicted in Fig. 3.7. The two concentric regions of surface structures covering the shallow crater are separated by a very thin annulus where ripples and rudiments of the surface structures of the central area coexist. The values of the threshold fluence were estimated by considering the Gaussian spatial beam profile with a $1/e^2$ beam waist ω_0. Prior to such an analysis, the reliability of this assumption was verified by measuring the radius r of the two regions as a function of the laser pulse energy, E_p, for various values of the repetition rate in the range 0.1-200 kHz, observing in all cases the expected dependence $r^2 = (\omega_0^2/2)ln(E_p/E_{th})$, E_{th} being the threshold energy [28, 35, 58-60] as discussed in Chapter 2. Then, for each repetition rate the circle radii of the two regions were estimated and their uncertainty was obtained by considering the variability observed in repeated measurements by different individuals in our team. The corresponding threshold values and their uncertainties were, finally, obtained from the Gaussian beam profile for the corresponding values of the peak fluence F_p and beam spot dimension ω_0.

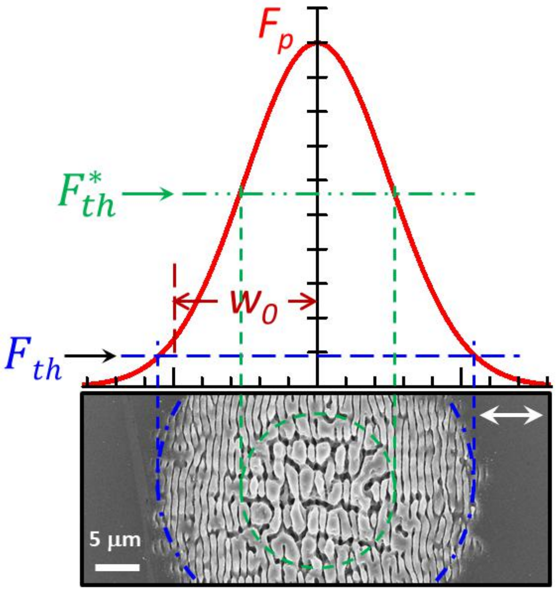

Fig. 3.7 Portion of a SEM micrograph of the Si target surface and the corresponding Gaussian spatial profile of the laser beam. The horizontal lines at F_{th} and F^*_{th} identify the values of the laser threshold fluences for crater/ripples formation and for the transition to the other surface structures generated in the inner, high-fluence region. The double-headed arrow indicates the incident laser pulse polarization. The SEM image refers to $N = 100$, $F_p \approx 0.84$ J/cm^2, $\omega_0 \approx 33$ µm at a repetition rate of 1 kHz in vacuum.

The variation of the threshold fluences F_{th} and F^*_{th} as a function of the repetition rate are reported in Fig. 3.8. As for vacuum irradiation, both threshold fluences for N=100 pulses seem to be independent of the repetition rate RR over the investigated range going from 0.1 kHz to 200 kHz. This observation, in turn, suggests that for the maximum repetition rate of 200 kHz available with our laser source, one can consider as negligible any effect of heat accumulation during laser irradiation in vacuum. The heat accumulation effect results from the progressive increase of the target temperature, pulse after pulse, during the laser irradiation sequence and the consequent transport of energy out of the irradiated region [25, 61]. This process is accompanied by a progressive damage in the surroundings of the irradiated area and an associated degradation of the generated craters, which become larger and rougher at higher repetition rates [61-63]. Instead, we observe a constancy of both the outer periphery and the inner transition region of the craters as well as a steadiness of the morphological features of the produced surface structures over the whole range of repetition rate investigated.

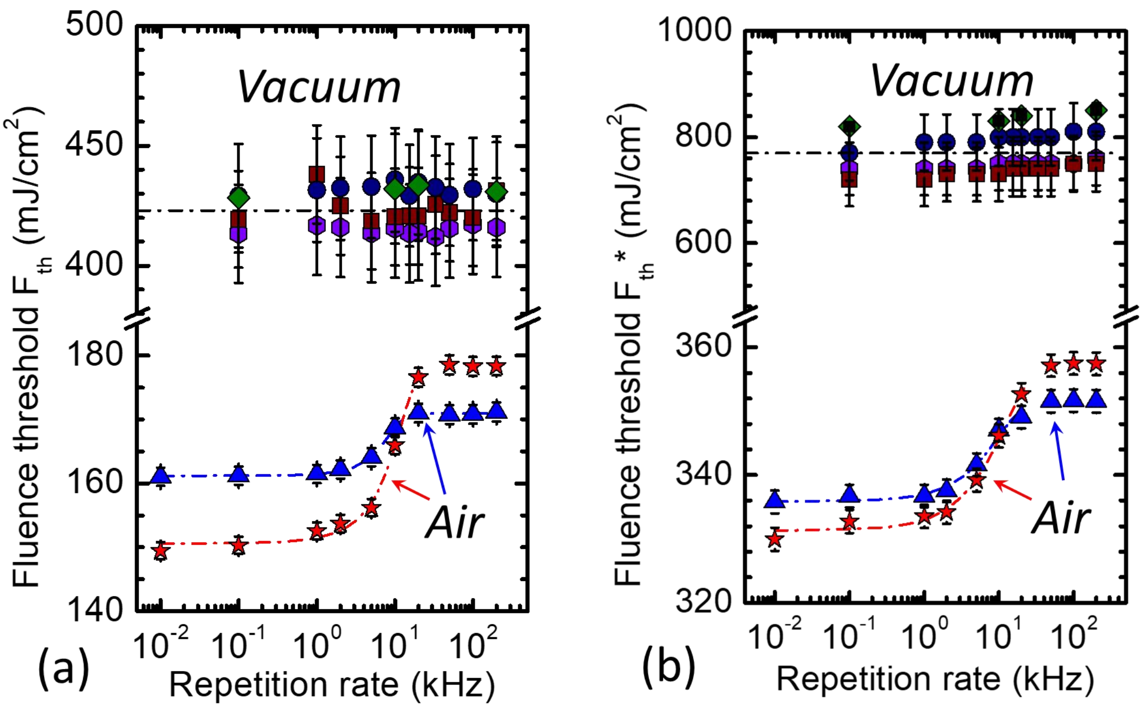

Fig. 3.8 Variation of the threshold fluences F_{th} (a) and F^*_{th} (b) as a function of the repetition rate for irradiation in air, with a sequence of N=100 (triangles) and N=200 (stars) at a laser peak fluence F_p = 0.84 J/cm^2, and in vacuum, for N=100 at four different values of the peak fluence, namely F_p of 0.78 (hexagons), 0.84 (squares), 0.91 (circles) and 0.97 (rhombuses) J/cm^2. The lines are guides to the eye.

The variation of the threshold fluences as a function of the repetition rate RR in air is reported in Fig. 3.8, both for N=100 and N=200 pulses. As for N=100 pulses, in air one can observe a consistent reduction, by a factor of ≈2, of both F_{th} and F^*_{th} with respect to vacuum at low values of RR. A rather similar correlation in the threshold of surface structuring is observed in the case of silicon irradiated with at 1055 nm and 900 fs laser pulses [51]. This aspect was already addressed above and can be associated to the increased absorption induced by the nanoparticles debris for irradiation in air. Interestingly, in air both F_{th} and F^*_{th} show a progressive rise with the repetition rate when RR reaches values of the order of tens of kHz, eventually approaching a plateau regime for RR≥50 kHz. Such a rise of the threshold fluences at the higher values of the repetition rates is still more pronounced for N=200 pulses.

The diverse behavior of the threshold fluences F_{th} and F^*_{th} in vacuum and air for repetition rates larger than few kHz observed in Fig. 3.8 can be clearly associated to the role played by the ablated material and the consequent nanoparticles debris decorating the target surface in air with respect to vacuum. In fact, the ablated material can be more effectively confined at atmospheric pressure than in vacuum. As evidenced by time-gated imaging and laser-beam transmission measurements of fs laser produced plasmas, at high pressure the cloud of ablated material can last in front of the irradiated target surface for longer delay after the laser ablation pulse with a backward flux of nanoparticles still persisting at a maximum time of measurement reaching values of the order of ≈50-60 μs [53-54]. Instead, in vacuum the ablated material follows a free expansion and its density suddenly decreases with time after the laser ablation pulse [54]. The typical values of permanence time of ablated material measured in air at atmospheric pressure seem to be coherent with the values of the repetition rates at which a rise of the threshold fluences is observed, thus suggesting a plume shielding effect as responsible for the observed behavior. The increase of the threshold fluences can be, therefore, related to a reduction of the effective laser energy reaching the target surface due to absorption and scattering of the incoming laser light by the cloud of ablated material.

3.3.3 The periods of ripples and groove: comparison between air and vacuum

As last issue, we illustrate the morphological features of the produced surface structures. Our experimental findings indicate that ripples are formed for values of the local fluence ranging between F_{th} and F^*_{th}, with $F^*_{th} \approx 2\ F_{th}$, both in vacuum and in air. Fig. 3.9(a) reports the ripples period observed in vacuum and in air as a function of the repetition rate *RR*, for *N*=100 pulses. For the sake of completeness, the period of the grooves observed in air for *RR*≤20 kHz is also shown. One can clearly observe that the period of the surface structures is independent of the repetition rate. However, the ripples period in vacuum results larger than in air. Such an aspect has been already addressed in our previous reports on laser surface texturing of Si by using ≈ 900 fs laser pulses at 1055 nm provided by a Nd:glass source operating at 33 Hz, in which the pressure variation of the ripples period was also addressed [51, 64].

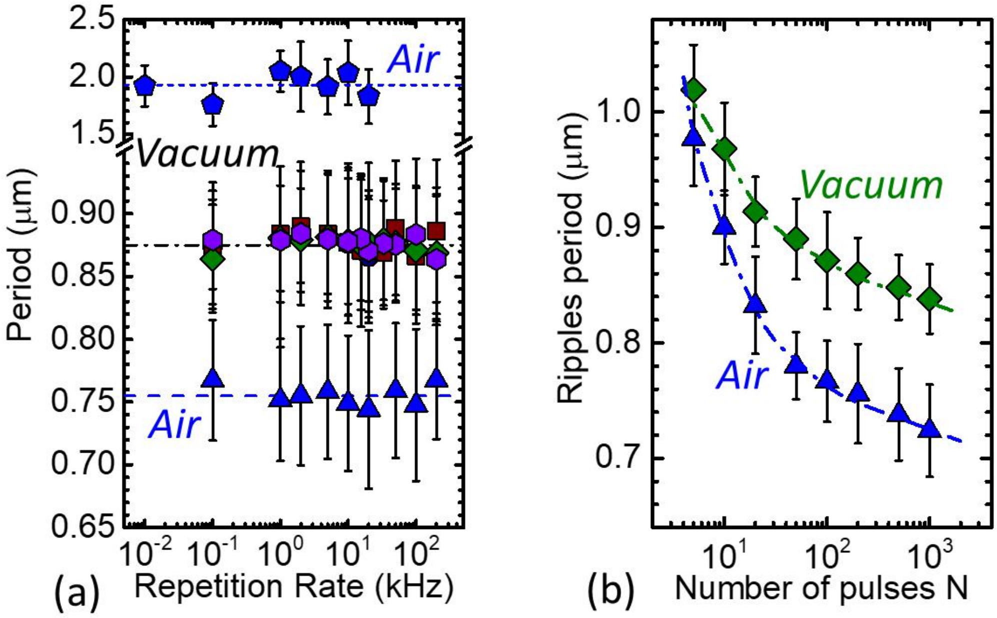

Fig. 3.9 (a) Variation of the period of the ripples as a function of the repetition rate after irradiation with a sequence of N=100 pulses in air (triangles) at a laser peak fluence F_p=0.84 J/cm^2 and in vacuum at four different values of the peak fluence F_p of 0.78 (hexagons), 0.84 (squares), 0.91 (circles) and 0.97 (rhombuses) J/cm^2. In the upper part of panel (a) the period of the grooves is also reported for the values of the repetition rate for which they are clearly discernible, i.e. *RR*≤20 kHz; (b) Variation of the ripples period on the number of pulses N for irradiation at a repetition rate of 200 kHz in air at a peak fluence F_p= 0.84 J/cm^2 (triangles) and in vacuum (rhombuses). The lines are guides to the eye.

Fig. 3.9(b) reports the variation of the ripples period as a function of the number of laser pulses *N* for *RR*= 200 kHz, in air at F_p≈ 0.8 J/cm^2 (triangles) and in vacuum (rhombuses). In both cases, the ripples period progressively decreases as a function of *N*. At few pulses, the ripples period only differs by few percent between vacuum and air, but the variation in air becomes much stronger than in vacuum by increasing *N*, until a similar rate of change seems to be approached above hundred pulses. Typically, the reduction of the ripples period with *N* is rationalized in terms of the progressive deepening of the surface modulation and the corresponding change in the incident angle [41]. It was already observed in an earlier work that lowering the pressure reduces the depth of modulation [64], which is coherent with the lower variation of the ripples period observed in air with respect to vacuum in Fig. 3.9(b).

Hence, the present observation suggests that the two experimental factors that seem to influence the ripple period in vacuum are the reduced depth of surface modulation and the significant decrease of nanoparticles back-deposition with respect to air.

The most common explanation of ripples formation is the spatial modulation of the absorbed fluence induced by interference between the incident laser light and surface scattered electromagnetic waves on a rough surface [5, 17]. In intrinsic semiconductors, the excitation of these scattered waves can occur also in form of surface plasmon polaritons due to the transition to a metallic state induced by the fs laser pulse irradiation [40, 58]. For linearly polarized light at normal incidence, the ripples period scales as $\Lambda_R = \lambda/Re[\eta]$, λ being the laser wavelength, $\eta = 1/\sqrt{\varepsilon_D^{-1} + \varepsilon_T^{-1}} \approx \sqrt{\varepsilon_T/(\varepsilon_T+1)}$ the effective refractive index of the interface formed by the dielectric ambient medium (dielectric constant $\varepsilon_D \approx 1$, for air or vacuum) and the excited target material (dielectric constant ε_T), and Re indicating the real part [1]. In this scenario, the lower period observed in air can be related to a larger effective refractive index of the interface in this condition likely induced by the more consistent decoration of the surface with nanoparticles due to the back-deposition of the ablated material [1, 17, 65], which can also explain the progressive difference between air and vacuum with the rise of the number of pulse *N* observed in Fig. 3.9(b).

The mechanisms for the formation of grooves are still not yet fully established, however it does seem that hydrodynamics and melt flow dynamics play key roles in their generation [17, 30-31, 66]. Moreover, simulation of multiple pulse irradiation with Finite Difference Time Domain (FDTD) methods seem to suggest that grooves can also result from electromagnetic processes related to scattering from surface defects, like nanoparticles [37, 46, 67-68]. In this respect, the experimental observations that both high repetition rate and vacuum ambient hamper the formation of grooves, that instead are generated for irradiation in air at repetition rates lower than 20 kHz, are particularly interesting. The latter observation concerning the observed differences between irradiation in air and vacuum at low repetition rates seems to support a possible influence of the nanoparticle debris on the formation of grooves. The former finding, instead, might be indicative of a possible variation of melt flow and hydrothermal waves dynamics with the laser pulse repetition rate, namely for RR approaching hundred kHz. Both these aspects will deserve further investigations to fully clarify their role in grooves formation.

3.4 Conclusions

In the present chapter two issues were addressed. In the first part of the chapter, an experimental investigation on the formation of ripples and grooves during fs laser surface irradiation of silicon in dynamic irradiation conditions was reported. The silicon target was irradiated by a ~180 fs laser beam at a central wavelength of 1030 nm forming shallow linear tracks at various values of the target scanning speed and laser pulse energy. The samples were analyzed by SEM and the main features of the process were addressed through analysis of the surface images by direct analysis and through the elaboration of 2D-FFT maps. Our experimental findings allow assessing the effective number of pulses as a reliable parameter to analyze the dependence of the threshold fluence for the formation of both ripples and grooves on the experimental conditions. In particular, the existence of an incubation behavior was clearly addressed with an incubation factor $\xi=(0.78\pm0.04)$ for both ripples and grooves at a wavelength of 1030 nm. Moreover, the influence of the effective number of laser pulses and accumulated fluence dose on the period of ripples and grooves was also addressed and compared with previous observations obtained in static irradiation conditions. Here as well the ripples period reduces with the effective pulse number, whereas an opposite trend is observed for the grooves. Finally, linear tracks were produced on the silicon sample at the same accumulated fluence dose but with different couple of values of the pulse energy and scanning speed. The 2D-FFT analysis of the corresponding SEM images show rather similar general features, but evidence interesting differences addressing a higher degree of regularity of the surface structures at lower values of the laser pulse energy and scanning speed.

In the second part of the chapter, an experimental investigation on the irradiation of a silicon target with fs laser pulses in vacuum and in air for repetition rates varying from 0.01 to 200 kHz, in static conditions was illustrated. Our findings provide further experimental data addressing clear differences for irradiation in vacuum and air, even at high repetition rate. The observation that grooves formation is hindered in high vacuum for repetition rates lower than 10 kHz further supports a possible role of the nanoparticles in their formation mechanisms. Instead, we observe ripples formation with a period independent of the repetition rate over the investigated range of 0.01-200 kHz. Moreover, our results confirm that irradiation in vacuum leads to a larger ripples period with respect to air even for repetition rates up to 200 kHz. This aspect was rationalized in terms of the different modulation of the surface depth as well as nanoparticles coverage in the two different experimental conditions. Another very interesting aspect is the influence of plume shielding, that is negligible in vacuum but becomes important in air at repetition rates larger than about 10 kHz. We also remark the three-fold decrease of the threshold fluence in air, with respect to vacuum, that is ascribed to the nanoparticle debris covering the target surface due to the material back-deposition. In conclusion, the absence of heat accumulation as well as the hindering of plume shielding in vacuum up to 200 kHz is particularly relevant, whereas irradiation in air should be limited to repetition rates below 10 kHz to avoid the latter effect.

The experimental findings discussed in this chapter provide a step forward in the assessment of the various experimental parameters towards a better understanding of the process of surface structures formation by fs laser irradiation, namely the role of the repetition rate, the processing ambient (air vs vacuum) and the scanning speed.

Bibliography

[1] A. Y. Vorobyev, C. Guo. Direct femtosecond laser surface nano/microstructuring and its applications. Laser Photonics Rev. 7 (2013) 385-407. https://doi.org/10.1002/lpor.201200017.

[2] J. Bonse, S. Hohm, S. V. Kirner, A. Rosenfeld, J. Kruger. Laser-Induced Periodic Surface Structures-A Scientific Evergreen. IEEE J. Sel. Top. Quantum Electron. 23 (2017) 9000615. https://doi.org/10.1109/JSTQE.2016.2614183.

[3] E. Stratakis, J. Bonse, J. Heitz, J. Siegel, G. D. Tsibidis, E. Skoulas, A. Papadopoulos, A. Mimidis, A. C. Joel, P. Comanns, J. Krüger, C. Florian, Y. Fuentes-Edfuf, J. Solis, W. Baumgartner. Laser engineering of biomimetic surfaces. Mater. Sci. Eng. R Rep. 141 (2020) 100562. https://doi.org/10.1016/j.mser.2020.100562.

[4] J. Bonse. Quo vadis LIPSS?—recent and future trends on laser-induced periodic surface structures. Nanomaterials 10 (2020) 1950. https://doi.org/10.3390/nano10101950.

[5] J. Bonse, S. V. Kirner, J. Krüger. Laser-Induced Periodic Surface Structures (LIPSS). Handbook of Laser Micro- and Nano-Engineering. Springer International Publishing, (2020) 1-59. https://doi.org/10.1007/978-3-319-69537-2_17-2.

[6] M. Malinauskas, A. Žukauskas, S. Hasegawa, Y. Hayasaki, V. Mizeikis, R. Buividas, S. Juodkazis. Ultrafast laser processing of materials: from science to industry. Light Sci. Appl. 5 (2016) e16133. https://doi.org/10.1038/lsa.2016.133.

[7] A. Ruiz de la Cruz, R. Lahoz, J. Siegel, G.F. de la Fuente, J. Solis. High speed inscription of uniform, large-area laser-induced periodic surface structures in Cr films using a high repetition rate fs laser. Opt. Lett. 39 (2014) 2491. https://doi.org/10.1364/ol.39.002491.

[8] Y. Fuentes-Edfuf, J. A. Sánchez-Gil, C. Florian, V. Giannini, J. Solis, J. Siegel. Surface Plasmon Polaritons on Rough Metal Surfaces: Role in the Formation of Laser-Induced Periodic Surface Structures. ACS Omega 4 (2019) 6939-6946. https://doi.org/10.1021/acsomega.9b00546.

[9] I. Gnilitskyi, T. J. Y. Derrien, Y. Levy, N. M. Bulgakova, T. Mocek, L. Orazi. High-speed manufacturing of highly regular femtosecond laser-induced periodic surface structures: physical origin of regularity. Sci. Rep. 7 (2017) 8485. https://doi.org/10.1038/s41598-017-08788-z.

[10] I. Gnilitskyi, V. Gruzdev, N. M. Bulgakova, T. Mocek, L. Orazi. Mechanisms of high-regularity periodic structuring of silicon surface by sub-MHz repetition rate ultrashort laser pulses. Appl. Phys. Lett. 109 (2016) 143101. https://doi.org/10.1063/1.4963784.

[11] J. JJ. Nivas, E. Allahyari, S. Amoruso. Direct femtosecond laser surface structuring with complex light beams generated by q-plates. Adv. Opt. Technol. 9 (2020) 53-56. https://doi.org/10.1515/aot-2019-0067.

[12] J. JJ. Nivas, S. He, Z. Song, A. Rubano, A. Vecchione, D. Paparo, L. Marrucci, R. Bruzzese, S. Amoruso. Femtosecond laser surface structuring of silicon with Gaussian and optical vortex beams. Appl. Surf. Sci. 418 (2017) 565-571. https://doi.org/10.1016/j.apsusc.2016.10.162.

[13] R. Buividas, M. Mikutis, S. Juodkazis. Surface and bulk structuring of materials by ripples with long and short laser pulses: Recent advances. Prog. Quantum. Electron. 38 (2014) 119-156. https://doi.org/10.1016/j.pquantelec.2014.03.002.

[14] K. Sugioka, Y. Cheng. Ultrafast lasers—reliable tools for advanced materials processing. Light Sci. Appl. 3 (2014) e149. https://doi.org/10.1038/lsa.2014.30.

[15] D. Zhang, L. C. Wu, M. Ueki, Y. Ito, K. Sugioka. Femtosecond laser shockwave peening ablation in liquids for hierarchical micro/nanostructuring of brittle silicon and its biological application. J. Extrem. Manuf. 2 (2020) 045001. https://doi.org/10.1088/2631-7990/abb5f3.

[16] F. Fraggelakis, G. D. Tsibidis, E. Stratakis. Ultrashort pulsed laser induced complex surface structures generated by tailoring the melt hydrodynamics. Opto-Electron. Adv. 5 (2022) 210052. https://doi.org/10.29026/oea.2022.210052.

[17] J. Bonse, S. Gräf. Maxwell Meets Marangoni—A Review of Theories on Laser-Induced Periodic Surface Structures. Laser Photonics Rev. 14 (2020) 2000215. https://doi.org/10.1002/lpor.202000215.

[18] J. Bonse, S. Gräf. Ten Open Questions about Laser-Induced Periodic Surface Structures. Nanomaterials 11 (2021) 3326. https://doi.org/10.3390/nano11123326.

[19] F. Fraggelakis, G. Mincuzzi, J. Lopez, I. Manek-hönninger, R. Kling, D. H. Kam, S. Bhattacharya, J. Mazumder. Texturing metal surface with MHz ultra-short laser pulses. Opt. Express 25 (2017) 18131-18139. https://doi.org/10.1364/OE.25.018131.

[20] R. Le Harzic, D. Dörr, D. Sauer, M. Neumeier, M. Epple, H. Zimmermann, F. Stracke. Large-area, uniform, high-spatial-frequency ripples generated on silicon using a nanojoule-femtosecond laser at high repetition rate. Opt. Lett. 36 (2011) 229. https://doi.org/10.1364/ol.36.000229.

[21] R. Le Harzic, F. Stracke, H. Zimmermann. Formation mechanism of femtosecond laser-induced high spatial frequency ripples on semiconductors at low fluence and high repetition rate. J. Appl. Phys. 113 (2013) 183503. https://doi.org/10.1063/1.4803895.

[22] X. Sedao, M. Lenci, A. Rudenko, N. Faure, A. Pascale-Hamri, J. P. Colombier, C. Mauclair. Influence of pulse repetition rate on morphology and material removal rate of ultrafast laser ablated metallic surfaces. Opt. Lasers Eng. 116 (2019) 68-74. https://doi.org/10.1016/J.OPTLASENG.2018.12.009.

[23] E. Allahyari, J. JJ. Nivas, M. Valadan, R. Fittipaldi, A. Vecchione, L. Parlato, R. Bruzzese, C. Altucci, S. Amoruso. Plume shielding effects in ultrafast laser surface texturing of silicon at high repetition rate in air. Appl. Surf. Sci. 488 (2019) 128-133. https://doi.org/10.1016/j.apsusc.2019.05.219.

[24] E. Allahyari, J. JJ. Nivas, G. Avallone, M. Valadan, M. Singh, V. Granata, C. Cirillo, A. Vecchione, R. Bruzzese, C. Altucci, S. Amoruso. Femtosecond laser surface irradiation of silicon in air: Pulse repetition rate influence on crater features and surface texture. Opt. Laser Technol. 126 (2020) 106073. https://doi.org/10.1016/j.optlastec.2020.106073.

[25] F. Nyenhuis, A. Michalowski, J. L'Huillier. Ultrashort pulse surface melting and smoothing: The impact of pulse spacing on heat accumulation and structure formation. J. Appl. Phys. 130 (2021) 053106. https://doi.org/10.1063/5.0049987.

[26] X. Sedao, M. Lenci, A. Rudenko, A. P. Hamri, J. P. Colombier, C. Mauclair. Additive and Substractive Surface Structuring by Femtosecond Laser Induced Material Ejection and Redistribution. Materials 11 (2018) 2456. https://doi.org/10.3390/ma11122456.

[27] J. Bonse, J. Krüger, S. Höhm, A. Rosenfeld. Femtosecond laser-induced periodic surface structures. J. Laser Appl. 24 (2012) 042006. https://doi.org/10.2351/1.4712658.

[28] J. M. Liu. Simple technique for measurements of pulsed Gaussian-beam spot sizes. Opt. Lett. 7 (1982) 196-198. https://doi.org/10.1364/OL.7.000196.

[29] S. He, J. JJ. Nivas, A. Vecchione, M. Hu, S. Amoruso. On the generation of grooves on crystalline silicon irradiated by femtosecond laser pulses. Opt. Express. 24 (2016) 3238-3247. https://doi.org/10.1364/oe.24.003238.

[30] J. JJ. Nivas, S. Amoruso. Generation of Supra-Wavelength Grooves in Femtosecond Laser Surface Structuring of Silicon. Nanomaterials 11 (2021) 174. https://doi.org/10.3390/NANO11010174.

[31] E. Allahyari, J. JJ. Nivas, E. Skoulas, R. Bruzzese, G.D. Tsibidis, E. Stratakis, S. Amoruso. On the formation and features of the supra-wavelength grooves generated during femtosecond laser surface structuring of silicon. Appl. Surf. Sci. 528 (2020) 146607. https://doi.org/10.1016/j.apsusc.2020.146607.

[32] J. Eichstädt, G. R. B. E. Römer, A. J. Huis In'T Veld. Determination of irradiation parameters for laser-induced periodic surface structures. Appl. Surf. Sci. 264 (2013) 79-87. https://doi.org/10.1016/j.apsusc.2012.09.120.

[33] G. R. B. E. Römer, M. Mezera. Model based optimization of process parameters to produce large homogeneous areas of laser-induced periodic surface structures, Opt. Express 27 (2019) 6012-6029. https://doi.org/10.1364/oe.27.006012.

[34] J. B. Nielsen, J. M. Savolainen, M. S. Christensen, P. Balling. Ultra-short pulse laser ablation of metals: threshold fluence, incubation coefficient and ablation rates. Appl. Phys. A 101 (2010) 97-101. https://doi.org/10.1007/s00339-010-5766-1.

[35] J. Bonse, S. Baudach, J. Krüger, W. Kautek, M. Lenzner. Femtosecond laser ablation of silicon-modification thresholds and morphology. Appl. Phys. A 74 (2002) 19-25. https://doi.org/10.1007/s003390100893.

[36] J. Bonse, J. Krüger. Pulse number dependence of laser-induced periodic surface structures for femtosecond laser irradiation of silicon. J. Appl. Phys. 108 (2010) 34903. https://doi.org/10.1063/1.3456501.

[37] J. Z. P. Skolski, G. R. B. E. Römer, J. Vincenc Obona, A. J. Huis In'T Veld. Modeling laser-induced periodic surface structures: Finite-difference time-domain feedback simulations. J. Appl. Phys. 115 (2014) 103102. https://doi.org/10.1063/1.4867759.

[38] G. D. Tsibidis, C. Fotakis, E. Stratakis. From ripples to spikes: A hydrodynamical mechanism to interpret femtosecond laser-induced self-assembled structures. Phys. Rev. B 92 (2015) 041405. https://doi.org/10.1103/PhysRevB.92.041405.

[39] J. JJ. Nivas, S. He, A. Rubano, A. Vecchione, D. Paparo, L. Marrucci, R. Bruzzese, S. Amoruso. Direct Femtosecond Laser Surface Structuring with Optical Vortex Beams Generated by a q-plate. Sci. Rep. 5 (2015) 17929. https://doi.org/10.1038/srep17929.

[40] G. D. Tsibidis, M. Barberoglou, P. A. Loukakos, E. Stratakis, C. Fotakis. Dynamics of ripple formation on silicon surfaces by ultrashort laser pulses in subablation conditions. Phys. Rev. B 86 (2012) 115316. https://doi.org/10.1103/PhysRevB.86.115316.

[41] M. Huang, F. Zhao, Y. Cheng, N. Xu, Z. Xu. Origin of laser-induced near-subwavelength ripples: interference between surface plasmons and incident laser. ACS Nano. 3 (2009) 4062-4070. https://doi.org/10.1021/nn900654v.

[42] J. JJ. Nivas, K. K. Anoop, R. Bruzzese, R. Philip, S. Amoruso. Direct femtosecond laser surface structuring of crystalline silicon at 400 nm. Appl. Phys. Lett. 112 (2018) 121601. https://doi.org/10.1063/1.5011134.

[43] G. D. Tsibidis, E. Stratakis. Ripple formation on silver after irradiation with radially polarised ultrashort-pulsed lasers. J. Appl. Phys. 121 (2017) 163106. https://doi.org/10.1063/1.4982071.

[44] G. D. Tsibidis, A. Mimidis, E. Skoulas, S. V. Kirner, J. Krüger, J. Bonse, E. Stratakis. Modelling periodic structure formation on 100Cr6 steel after irradiation with femtosecond-pulsed laser beams. Appl. Phys. A 124 (2018) 27. https://doi.org/10.1007/s00339-017-1443-y.

[45] Gwyddion - A modular program for SPM (scanning probe microscopy) data visualization and analysis. http://gwyddion.net/.

[46] J. Z. P. Skolski, G. R. B. E. Römer, J. V. Obona, V. Ocelik, A. J. Huis In't Veld, J. T. M. De Hosson. Laser-induced periodic surface structures: Fingerprints of light localization. Phys. Rev. B 85 (2012) 1-9. https://doi.org/10.1103/PhysRevB.85.075320.

[47] J. Lehr, A. M. Kietzig. Production of homogenous micro-structures by femtosecond laser micro-machining. Opt. Lasers Eng. 57 (2014) 121-129. https://doi.org/10.1016/j.optlaseng.2014.01.012.

[48] J. Bonse, S. Gräf. Ten Open Questions about Laser-Induced Periodic Surface Structures. Nanomaterials 11 (2021) 3326. https://doi.org/10.3390/nano11123326.

[49] P. Dominic, F. Bourquard, S. Reynaud, A. Weck, J. P. Colombier, F. Garrelie. On the Insignificant Role of the Oxidation Process on Ultrafast High-Spatial-Frequency LIPSS Formation on Tungsten. Nanomaterials 11 (2021) 1069. https://doi.org/10.3390/nano11051069.

[50] M. G. Lechuga, D. Puerto, Y. F. Edfuf, J. Solis, J. Siegel. Ultrafast Moving-Spot Microscopy: Birth and Growth of Laser-Induced Periodic Surface Structures. ACS Photonics 3 (2016) 1961-1967. https://doi.org/10.1021/acsphotonics.6b00514.

[51] J. JJ. Nivas, Z. Song, R. Fittipaldi, A. Vecchione, R. Bruzzese, S. Amoruso. Direct ultrashort laser surface structuring of silicon in air and vacuum at 1055 nm. Appl. Surf. Sci. 417 (2017) 149-154. https://doi.org/10.1016/J.APSUSC.2017.03.158.

[52] J. JJ. Nivas, E. Allahyari, F. Gesuele, P. Maddalena, R. Fittipaldi, A. Vecchione, R. Bruzzese, S. Amoruso. Influence of ambient pressure on surface structures generated by ultrashort laser pulse irradiation. Appl. Phys. A 124 (2018) 198. https://doi.org/10.1007/s00339-018-1621-6.

[53] A. Pereira, P. Delaporte, M. Sentis, W. Marine, A. L. Thomann, C. Boulmer-Leborgne. Optical and morphological investigation of backward-deposited layer induced by laser ablation of steel in ambient air. J. Appl. Phys. 98 (2005) 064902. https://doi.org/10.1063/1.2058193.

[54] S. Amoruso, R. Bruzzese, X. Wang, J. Xia. Propagation of a femtosecond pulsed laser ablation plume into a background atmosphere. Appl. Phys. Lett. 92 (2008) 041503. https://doi.org/10.1063/1.2839582.

[55] J. Bonse, M. Munz, H. Sturm. Structure formation on the surface of indium phosphide irradiated by femtosecond laser pulses. J. Appl. Phys. 97 (2005) 013538. https://doi.org/10.1063/1.1827919.

[56] A. Y. Vorobyev, C. Guo. Enhanced absorptance of gold following multipulse femtosecond laser ablation. Phys. Rev. B 72 (2005) 195422. https://doi.org/10.1103/PhysRevB.72.195422.

[57] A. Y. Vorobyev, C. Guo. Direct creation of black silicon using femtosecond laser pulses. Appl. Surf. Sci. 257 (2011) 7291-7294. https://doi.org/10.1016/j.apsusc.2011.03.106.

[58] J. Bonse, M. Munz, H. Sturm. Structure formation on the surface of indium phosphide irradiated by femtosecond laser pulses. J. Appl. Phys. 97 (2005) 013538. https://doi.org/10.1063/1.1827919.

[59] D. Bouilly, D. Perez, L. J. Lewis. Damage in materials following ablation by ultrashort laser pulses: A molecular-dynamics study. Phys. Rev. B 76 (2007) 184119. https://doi.org/10.1103/PhysRevB.76.184119.

[60] E. Allahyari, J. JJ. Nivas, F. Cardano, R. Bruzzese, R. Fittipaldi, L. Marrucci, D. Paparo, A. Rubano, A. Vecchione, S. Amoruso. Simple method for the characterization of intense Laguerre-Gauss vector vortex beams. Appl. Phys. Lett. 112 (2018) 211103. https://doi.org/10.1063/1.5027661.

[61] R. Weber, T. Graf, P. Berger, V. Onuseit, M. Wiedenmann, C. Freitag, A. Feuer, J.-P. Negel, A. Voss, M. A. Ahmed, D. Bauer, D. Sutter, A. Killi, T. Graf. Heat accumulation during pulsed laser materials processing. Opt. Express 22 (2014) 11312-11324. https://doi.org/10.1364/OE.22.011312.

[62] T. Kramer, S. Remund, B. Jäggi, M. Schmid, B. Neuenschwander. Ablation dynamics-from absorption to heat accumulation/ultra-fast laser matter interaction. Adv. Opt. Technol. 7 (2018) 129-144. https://doi.org/10.1515/aot-2018-0010

[63] A. Ancona, A. Tünnermann, F. Röser, J. Limpert, K. Rademaker, S. Nolte. High speed laser drilling of metals using a high repetition rate, high average power ultrafast fiber CPA system. Opt. Express 16 (2008) 8958-8968. https://doi.org/10.1364/OE.16.008958.

[64] J. JJ. Nivas, F. Gesuele, E. Allahyari, S. L. Oscurato, R. Fittipaldi, A. Vecchione, R. Bruzzese, S. Amoruso. Effects of ambient air pressure on surface structures produced by ultrashort laser pulse irradiation. Opt. Lett. 42 (2017) 2710. https://doi.org/10.1364/OL.42.002710.

[65] A. Y. Vorobyev, V. S. Makin, C. Guo. Periodic ordering of random surface nanostructures induced by femtosecond laser pulses on metals. J. Appl. Phys. 101 (2007) 034903. https://doi.org/10.1063/1.2432288.

[66] G. D. Tsibidis, E. Skoulas, A. Papadopoulos, E. Stratakis. Convection roll-driven generation of supra-wavelength periodic surface structures on dielectrics upon irradiation with femtosecond pulsed lasers. Phys. Rev. B 94 (2016) 081305. https://doi.org/10.1103/PhysRevB.94.081305.

[67] H. Zhang, J. P. Colombier, C. Li, N. Faure, G. Cheng, R. Stoian. Coherence in ultrafast laser-induced periodic surface structures. Phys. Rev. B 92 (2015) 174109. https://doi.org/10.1103/PhysRevB.92.174109.

[68] H. Zhang, J. P. Colombier, S. Witte. Laser-induced periodic surface structures: Arbitrary angles of incidence and polarization states. Phys. Rev. B 101 (2020) 245430. https://doi.org/10.1103/PhysRevB.101.245430.

Chapter 4

Laser surface structuring of copper over large areas

This chapter mainly reports on the femtosecond laser processing of a copper target surface over large areas exploring in detail the dependence of the generated morphological features on scanning parameters as the beam scanning velocity and the hatch distance (i.e. the distance between the centers of two consecutive laser scans), the laser wavelength and the ambient gas. In particular, the influence of the scanning velocity V_s, i.e of the effective number of pulses N_{eff}, on the ripples period by means of 2D-FFT, $\Lambda_{2D-FFT,}$ is investigated observing that Λ_{2D-FFT} decreases with the increment of N_{eff}, in agreement with the expected behaviour. The chapter contains the description of surface structures emerging in different zones processed by the laser beam irradiation that are characterized by a different overlay of the scanned regions during the large area processing. It was observed that both well-defined ripples and other morphological features develop depending on the beam overlap. Moreover, the influence of the ambient conditions at different scanning speeds and wavelengths during the femtosecond laser processing of copper to form laser-induced periodic surface structures (LIPSS) on the surface is also investigated.

4.1 Introduction

Copper is a material widely used in electric devices thanks to its thermal and electrical properties. In particular, the research group in which my thesis work has been carried out is currently involved in a collaborative project aiming at reducing the secondary electron emission from copper surfaces irradiated by primary electrons [1]. In fact, the request to modify the surface of a cooper sample relies on the demand to mitigate the generation of secondary electrons in particle accelerators [2]. In the high energy colliders, photoemission and secondary emission phenomena cause multiplication processes within the beam chambers, whose walls are typically made of copper. These effects lead to the formation of an electron cloud causing instability of the particle beams [3-5]. The striking role of fs laser processing of copper surfaces on the Secondary Electron Yield (SEY) has been verified in many previous studies by generating engineered surfaces with micrometer size tracks [6-10]. Recently, the influence of LIPSS on a copper surface on the SEY has also been verified addressing a promising effect [1]. The generated surface microstructures greatly depend on experimental parameters, such as laser wavelength, polarization, pulse energy, number of pulses, repetition rate, scan velocity and hatch distance [11-13]. Therefore, in this chapter the effects of various laser parameters and processing conditions on the features of the LIPSS generated on copper samples during large area processing are analyzed.

Section 4.2 illustrates the use of a cylindrical lens for the focusing of the laser beam on the sample to form periodic surface structures over a millimeter size area in a reduced processing time. From this point of view, this work is devoted to the morphological characterization of the induced surface structures on copper by means of laser beams with an elliptical profile at two different laser wavelengths(1030 nm and 515 nm), in order to clarify the possible merits and drawbacks of such an approach.

In section 4.3, by exploiting the more common approach based on the use of a spherical lens for laser beam focusing over the target surface, the influence of three important laser processing parameters, namely the laser wavelength, the ambient gas, and the beam scanning velocity on the induced morphological modifications at the surface will be addressed.

4.2 Morphological features induced by using a cylindrical lens

This section focuses on the surface structures formed by laser raster scanning of copper surfaces on millimeter-sized regions. Large area surface processing of copper samples was carried out using the chirped pulse amplification Yb:KGW laser system described in Chapter 2. The laser source delivers pulses at $\lambda \approx 515\text{nm}$ with a duration of ≈ 180 fs produced through second harmonic generation in a BBO crystal. The laser beam is focused by using a cylindrical lens with a focal length of 150 mm, and hits the sample surface at normal incidence. In this experiment, the laser was operated at a repetition rate of RR = 5 kHz and at the power of 880 mW (pulse energy of ≈180 μJ).

The spot radius of the elliptical Gaussian laser beam on the target surface was estimated adapting the method proposed by Liu [14-17] and presented in the Section 2.3.2 of Chapter 2, obtaining $\omega_{0,x} = (8.7 \pm 0.1)$ μm and $\omega_{0,y} = (3.1 \pm 0.1)$ mm. For the analysis, the typical parameter N_{eff} is used to quantify the equivalent pulse number under dynamic irradiation of the sample in a configuration with laser scanning along the x direction (see Fig. 4.1), namely

$N_{eff} = 2\omega_{0x}\frac{RR}{V_s}$, V_s being the scanning velocity. Therefore, the corresponding number N_{eff} of overlapping pulses can be estimated for each scanning velocity V_s.

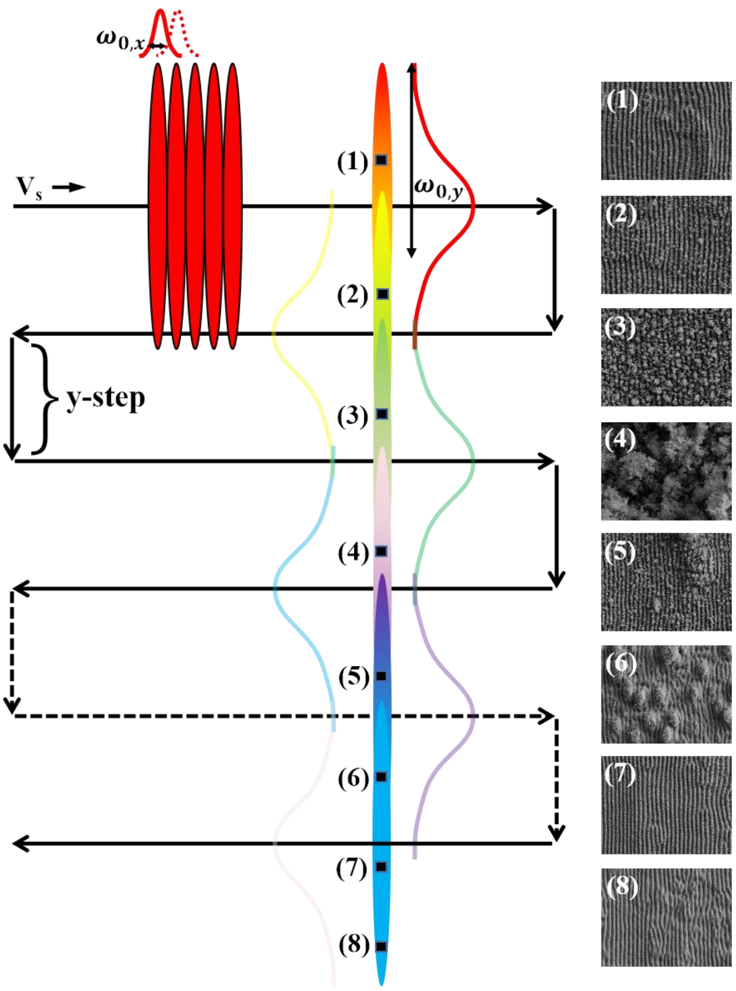

Fig. 4.1 The scanning path of the beam in the raster scan method with the spatial intensity distribution.

A schematic diagram of the scanning path is shown in Fig. 4.1: large area processing is obtained through a bidirectional scan along the horizontal (*x*) and vertical (*y*) directions by moving the sample at velocity V_s. The first line scan is to the right along the *x*-axis, then the beam moves down shifting a y-step along the *y*-axis and continuing to scan towards the left along the x-axis in the opposite direction to form a large-area scan of the copper sample. Since the y-step is less than the Gaussian spot $\omega_{0,y} = (3.1 \pm 0.1)$ mm, the spatial distribution of the laser intensity, is a superposition between the Gaussian spatial intensity distributions along the vertical direction. Hence, the zones numbered (1) to (9) have a different degree of overlap of the Gaussian laser distribution, resulting in different morphological characteristics of each zone as will be discussed in detail in the following analysis.

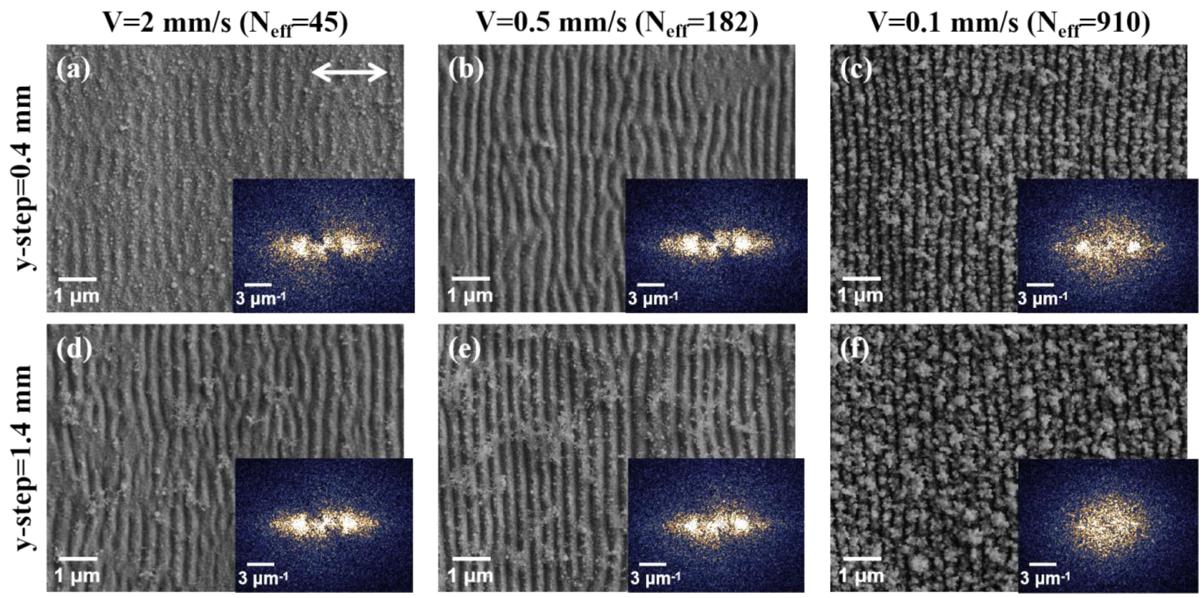

Fig. 4.2 SEM images of the upper edge of different areas processed with two different y-steps (0.4 mm and 1.4 mm) and different scanning velocity V_s. The double-headed arrow in panel (a) indicates the direction of the laser beam polarization. 2D-FFT of the SEM images are reported in the lower right corner of each panel.

Fig. 4.2 reports exemplificative scanning electron microscopy (SEM) micrographs of the upper edge of the processed area corresponding to region (1) of Fig. 4.1 for two different values of the hatch distance, namely 0.4 and 1.4 mm, and three different scan velocities (2, 0.5 and 0.1 mm/s). All the SEM images show the formation of ripples perpendicular to the laser beam polarization as well as the decoration nanoparticles back-deposited on the sample surface due to the air confinement.

As for surface morphological analysis, considering the scanning path and the two-dimensional (2D) Gaussian spatial distribution along the copper surface, we can obtain that the investigated region is exposed to the weaker part of the beam, that is, the part corresponding to the Gaussian tail. From a qualitative point of view, the amount of nanoparticles increases with the reduction of the scanning velocity (i.e. the increment of the number of effective pulses N_{eff}). This result is consistent with many other studies reporting that back-deposited nanoparticles depend not only on the laser energy but also on the number of pulses [18-20]. Panels (c) and (f) of Fig. 4.2 evidence nanoparticle clumps aligned along a typical ripples periodic pattern obtained at $N_{eff} = 910$ $(V_s = 0.1mm/s)$. In several papers [20-21], nanoparticle aggregation has been reported to produce ripples: as the number of pulses increases, the nanoparticles tend to align in periodic ripples. However, the mechanism of the formation of ordered aggregates of nanoparticles remains controversial. It can also be seen from Fig. 4.2 that as the scanning speed decreases or the number of effective pulses increases, the ripples are deeper and more regular. This effect may be ascribed to the lower intensity in the Gaussian beam tail, resulting in a local laser fluence that cannot induce substantial removal of material from the sample surface. Therefore, if the number of overlapping pulses is small, the resulting surface exhibits shallower ripples and less defined patterns, whereas if N_{eff} is increased, ablation of the sample surface is more consistent, resulting in well-defined ripples.

Table 4.1 Ripples spatial periods Λ_{2D-FFT} calculated from the 2D-FFT maps for the SEM images of Fig. 4.2.

$\mathrm{y-step}$	$\Lambda_{2D-FFT}(\mathrm{nm})$		
	$V_s = 2\mathrm{mm/s}$	$V_s = 0.5\mathrm{mm/s}$	$V_s = 0.1\mathrm{mm/s}$
0.4mm	353±20	349±15	345±23
1.4mm	358±22	352±10	323±25

Another observation derived from the qualitative analysis of the SEM images is the effect of N_{eff} on the period of ripples, Λ_{2D-FFT}. In fact, an increase in N_{eff} leads to a decrease in Λ_{2D-FFT}. To study the periodic structures in detail, two-dimensional fast Fourier transform (2D-FFT) mapping was performed on the SEM images. The 2D-FFT map generated by the *Gwyddion* software are reported in the lower right corner of the corresponding SEM image. In the 2D-FFT images, a pair of intense peaks can be identified along the propagation direction of the periodic pattern in real space due to ripples and a diffused signal related to the spread spatial frequencies ascribed to nanoparticles. The spatial frequency k of the two peaks is related to the period of the ripples, which can be derived from the formula $\Lambda_{2D-FFT} = 2/k$. Table 4.1 summarizes the values of the period Λ_{2D-FFT} obtained from the 2D-FFT images for the three cases reported in Fig. 4.2.

The data of Table 4.1 show that the period values are basically consistent, within the uncertainty, at each scanning speed independently of the hatch distance. In addition, it can be seen from the data that a decrease in scanning speed V_s (an increase in N_{eff}) results in a reduction of the spatial period of the ripples. This observation is consistent with some experimental results reported in the literature for both dynamic [5] and static [22-23] irradiation conditions. One of the most common interpretation of such an effect is that the target surface changes its optical properties pulse by pulse, which is thought to be due to a coupling mechanism between the incident laser beam and the grating formed by the previous sequence of incident pulses. So that the resonant wavelength of the surface plasmon polaritons (SPP) wave is shifted, resulting in a shortening of the spatial period of the interference pattern. Consequently, the modulation of the spatial energy distribution changes, producing morphological changes characterized by a progressively shorter period [22, 24]. However, other mechanisms such as local variation of the incident angle corresponding to the ablated region or accumulation of defects inside the material cannot be ignored either [21].

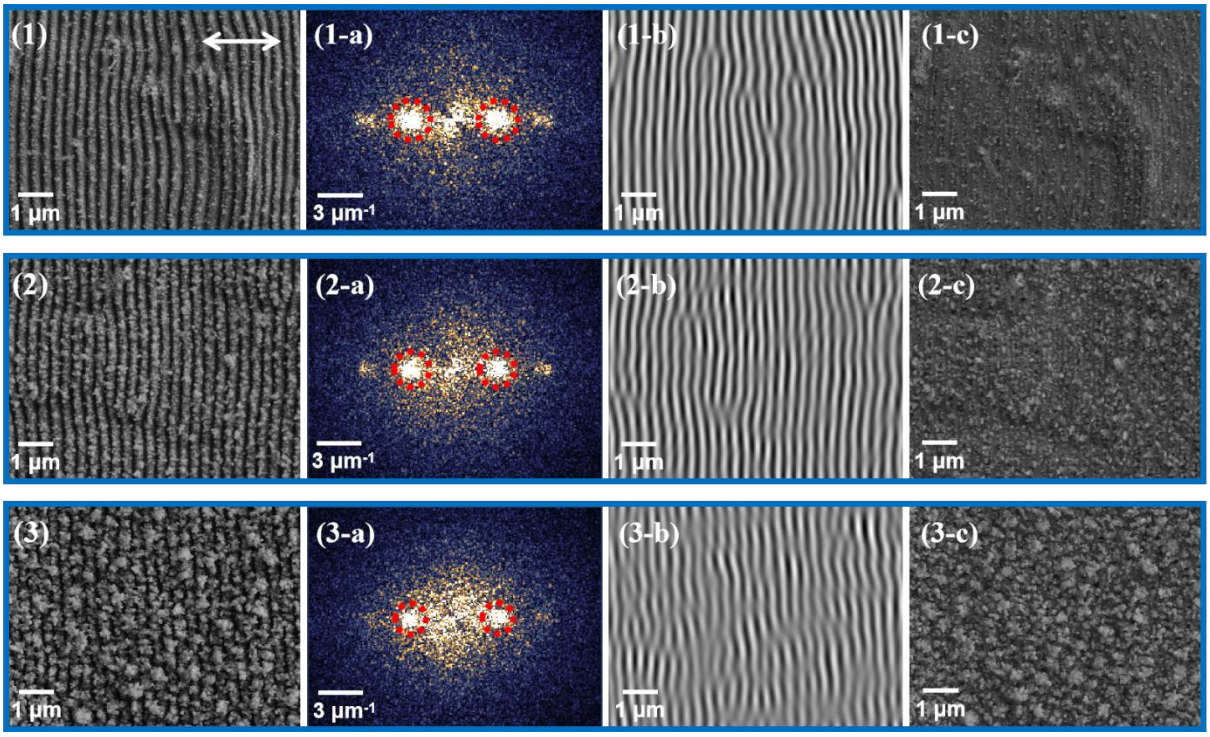

Fig. 4.3 Specific morphological analysis of different scanning parts (zones (1), (2) and (3) of Fig. 4.1) in copper samples over large area with $F_p = 0.45\ J/cm^2, V_s = 0.1mm/s$ and y-step=1.4mm. (1) SEM micrograph exemplifying the upper edge of the copper surface. (2) SEM image that identifies the surface structure below that illustrated in zone (1). (3) Periodic structures fully covered by nanoparticles. The second column are the 2D-FFT maps evidencing the two bright peaks associated to the ripples. The third column are 2D-IFFT maps corresponding to the intense coupled peaks in the dashed circles of 2D-FFT images. Whereas the fourth column are 2D-IFFT maps obtained considering the signals out of the dashed circles of the 2D-FFT maps. The white arrow in panel (1) indicates the laser beam polarization.

Fig. 4.3 reports a comparative analysis of the morphological features observed in the zones (1), (2) and (3) of Fig. 4.1. For large area scanning, the first row moving from left to right shows the area where the weaker part of the beam impinges on the sample surface. As shown in panel (1) of Fig. 4.3, this SEM image shows a wrinkled surface with well-defined ripples, the period of which is $\Lambda_{2D-FFT} = (323 \pm 25)$ nm as measured from the bright spots in the 2D-FFT map shown in panel (1-a).

After the first line is scanned, the beam moves down by a y-step=1.4 mm and scans from right to left to form the zone (2). Its SEM image (panel (2) of Fig. 4.3) shows a periodic pattern similar to that of zone (1): it is composed of ripples arranged perpendicular to the laser beam polarization decorated with nanoparticles. In this case, the period of the ripples measured by the 2D-FFT map in panel (2-a) is about (307$\pm$13) nm. We therefore find that the spatial period Λ_{2D-FFT} decreases with increasing N_{eff} that a similar trend can be observed: as the ripples period of zone (2) is slightly smaller than the ripples space period connected to zone (1). A possible explanation for the transition from clear ripples (zone (1)) to ripples moderately covered with nanoparticles (zone (2)) could rely on the superposition of the successive Gaussian spatial distributions of the laser beam. By moving the sample along the first line, the most intense part of the laser beam is stuck in zone (2), causing the surface to eject nanoparticles and change its optical properties.

The SEM micrograph in panel (3) of Fig. 4.3 shows periodic structures completely covered by nanoparticles, which appear to be assembled in a periodic fashion in the same way as ripples. The 2D-FFT map in panel (3-a) shows two weak intensity peaks (Λ_{2D-FFT}=(311 ± 34) nm) that is more heavily surrounded by the diffused signal due to a distribution of spatial frequencies induced by the larger coverage of nanoparticles than zones (1) and (2). For a better visualization of the ripples' features, the filtering method provided by the *Gwyddion* software is used to separate the contributions evidenced in the 2D-FFT maps corresponding to the strongly coupled peaks and the surrounding diffused signal and calculate the corresponding 2D-inverse FFT maps. The panels in the third column show the spatial modulation of ripples in real space obtained by a two-dimensional inverse fast Fourier transform (2D-IFFT), while panels of the latter column demonstrates the contribution to the observed morphological features of the nanoparticles in the real space.

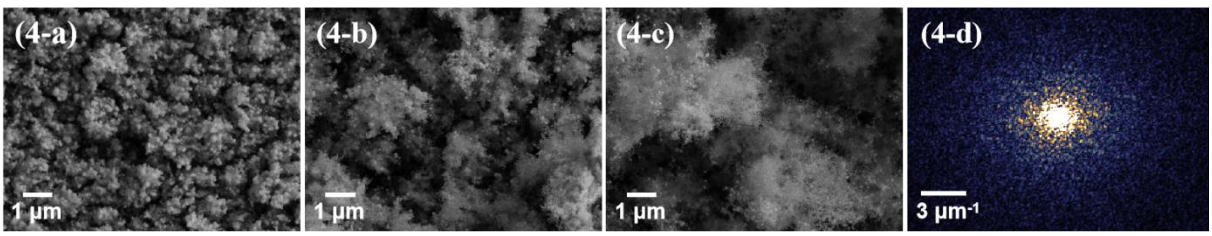

Fig. 4.4 Panels (4-a)-(4-c) display the copper surface entirely covered by nanoparticles observed in zone (4) of Fig. 4.1. Panel (4-d) exhibits the archetypal 2D-FFT for the regions fully covered by assemblies of nanoparticles.

From zones (1) to (3) of Fig. 4.3, it can be found that more nanoparticles are generated in the zones characterized by a larger overlap between the Gaussian spatial distributions of the scanning beam. Fig. 4.4 report SEM images in the next processed zone (4) of Fig. 4.1, showing nanoparticles randomly distributed on the target surface. In particular, panels (4-a) to (4-c) of Fig. 4.4 report some exemplificative SEM images of such assembly of nanoparticles decorating the sample surface in such a zone. Panel (4-d) represents the spectra obtained by calculating the 2D-FFT of the panel (4-c). The distribution of spatial frequencies is inherent to the presence of nanoparticles, and it is not possible to identify the formation of any characteristic peak pairs associated with ripples patterns.

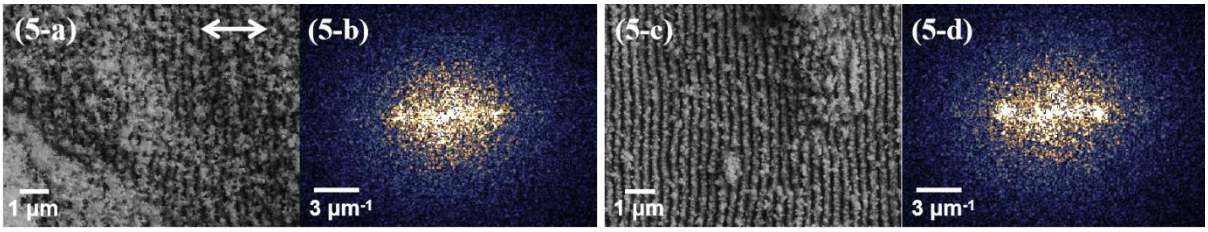

Fig. 4.5 two SEM images of copper surface in zone (5) together with their 2D-FFT maps. The white arrow in panel (5-a) indicates the laser beam polarization.

In the following scan, the formation of regular ripples starts to reappear at zone (5) as the superposition of the Gaussian laser intensity distribution begins to decrease (Fig. 4.5). In fact, in the 2D-FFT plot in panel (5-b) it is possible to recognize two weak peaks inherent to the periodic structure located under a carpet of nanoparticles and whose period was found to be (310±11) nm. Panel (5-c) is a successor to (5-a), showing the morphological features of (5-a). In this case, the overlap between Gaussian fluence distributions translates into periodic ripples patterns decorated by nanoparticle agglomerations. Correspondingly, the 2D-FFT map in panel (5-d) shows a period of (320±18) nm. Furthermore, the upper right corner of panel (5-c) represents the incoming of micro-bump formation.

Zone (6) has a periodic structure interrupted by the growth of raised circular reliefs identified as bumps, as shown in panel (6-a) in Fig. 4.6. This kind of surface structures have been observed in Al, Ti, gold, steel, copper [25-26] and other materials. It has been demonstrated that these structures can be replicated into a series of ordered arrays by exploiting the interference between multiple beams [27]. However, the mechanism underlying their formation remains controversial. Some authors believe that the bumps arise from plastic deformation caused by thermoelastic forces associated with the heating of the irradiated material. In particular, the stress confines the hot material to a small part of the surface, causing it to reach high temperatures and pressures, leading to possible phase explosions that form circular bumps [28]. Others believe that bump formation is related to rapid cooling and redistribution of molten material after fs laser treatment. Other possible explanations include shock waves and the Marangoni effect due to the excitation of the plasma plume located above the material [25, 28].

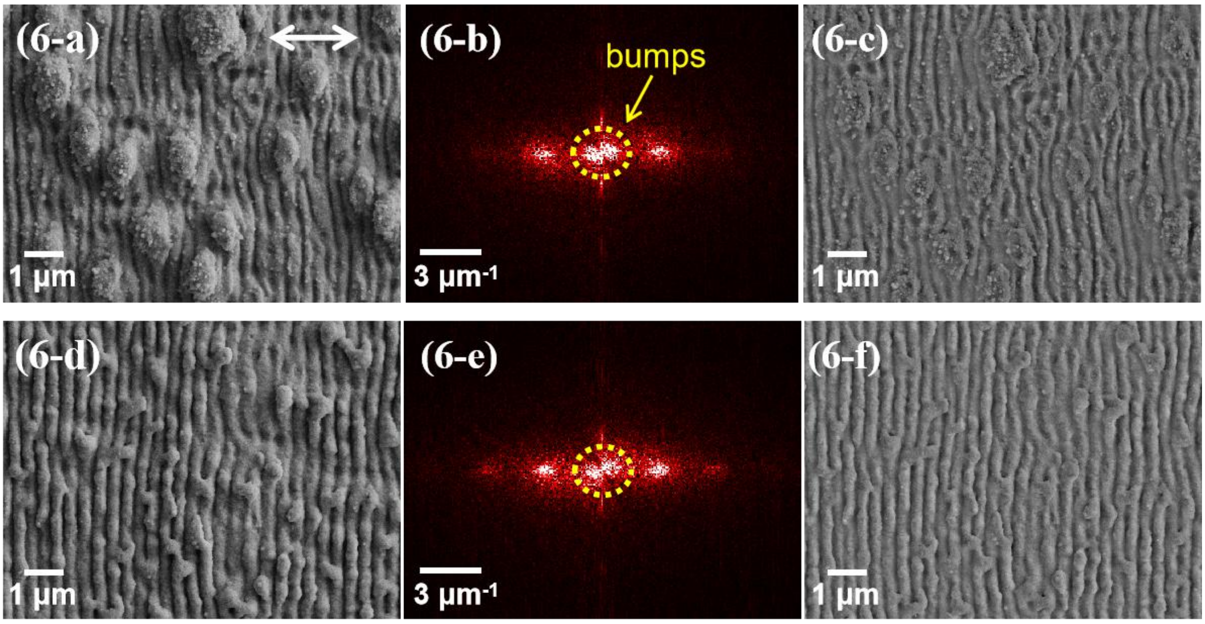

Fig. 4.6 Panel (6-a) presents structured copper surface characterized by bumps and ripples. Panel (6-d) is Rippled area resulting from the solidification of the irradiated structure. Panel (6-b) and (6-e) indicates the presence of ripples and bumps in 2D-FFT maps. Panel (6-c) and (6-f) is inherent to ripples in the real space.

Panel (6-b) of Fig. 4.6 reports the 2D-FFT plot of the SEM image in panel (6-a), from which we estimate Λ_{2D-FFT}= (330$\pm$16) nm. In addition, the graph identifies two bright spatial frequencies (marked by dashed yellow circles) that appear to be associated with bumps. To determine this correspondence, a 2D-IFFT mapping is performed by filtering the spatial frequencies in the center of the image. The results of this process are shown in panel (6-c), confirming our hypothesis, as the graph replicates the surface structure of panel (6-a) without the bumps. The SEM micrograph in panel (6-d) below shows the evolution of the bumps to periodic straight lines, which appears to be the result of rapid solidification in the irradiated region. The 2D-FFT plot in panel (6-e) displays the characteristic intensity peaks associated with the ripples, which we measured as Λ_{2D-FFT} = (355±45) nm. Note that this value for the ripple spatial period is the highest of all values found in all these zones.

Finally, Fig. 4.7 depicts the last two regions labeled as (7) and (8) in Fig. 4.1, in which the laser coverage is similar to zones (1) and (2): zone (7) coverage results in the same way as zone (2), whereas zone (8) coverage occurs in the same way as zone (1). From the 2D-FFT maps, we evaluate the ripples spatial period Λ_{2D-FFT} for the two SEM images as (312±20) nm for zone (7) and (335±31) nm for zone (8). It can be noted that the period of the ripples in zone (7) is almost identical to that of zone (2), while the period of zone (8) is in turn consistent with that obtained in zone (1). The fact that the ripples period obtained in region (7) is smaller suggests that the mechanisms behind their formation in the zones (7) and (8) are consistent with those of zones (2) and (1), respectively.

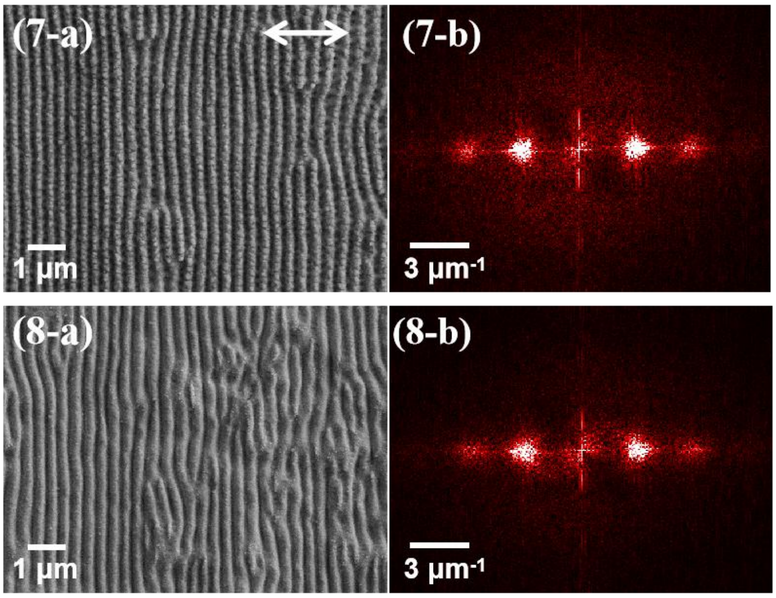

Fig. 4.7 SEM images of the structures formed in the zones (7) and (8) of the irradiated copper surface with their 2D-FFT maps. Panel (7-a) is the SEM image that identifies the upper edge of the zone (7), whereas panel (8-a) is the SEM micrograph exemplifying the surface structure below that illustrated in panel (7-a), that is zone (8).

Table 4.2 summarizes the ripples period for the eight different zones of Fig. 4.1. Our analysis evidences the effects of the superposition between the Gaussian beam intensity profiles pertaining to each laser beam passage during the rastering process. In particular, when the overlap is too high a great amount of nanoparticles appears on the irradiated surface. All the obtained results provide a clear picture of the various effects coming into play during large area structuring with elliptical beams and lay the foundation to investigate the best experimental conditions in order to form well defined ripples on copper.

Table 4.2 Ripples spatial periods Λ_{2D-FFT} in different zones.

Zones in Fig.4.1	(1)	(2)	(3)	(4)	(5)	(6)	(7)	(8)
$\Lambda_{2D-FFT}(nm)$	323±25	307±13	311±34	NO	310±11 320±18	330±16 355±45	312±20	335±31

4.3 LIPSS on copper at different wavelengths and ambient gases

In this Section, the results of experiments on LIPSS formed on copper at two different wavelengths and in three different environments are summarized. The Yb:KGW laser was used (pulse duration of ≈180 fs) at a repetition rate RR = 5 kHz, both at λ≈1030 nm (fundamental wavelength) and at λ≈515 nm (second harmonic generated by a BBO crystal). The laser beam was focused onto the copper surface through a plano-convex lens with a focal length of 200 mm, at normal incidence.The copper sample was held into a vacuum chamber equipped with a computer controlled XY translation stage working synchronously with the laser source.

The copper samples were pieces of polycrystalline copper oxygen-free electronic grade (OFE) with 1 mm thickness and 20×20 mm^2 dimensions cleaned by a standard procedure for ultra-high voltage (UHV) cleaning including a wet-chemical detergent-based degreasing process followed by rinsing in deionized water. Laser processing was done several weeks after the cleaning procedure.

Table 4.3 Laser processing parameters (E - pulse energy, ω_0 - Gaussian spot radius, F_{th} - ablation threshold).

λ	E	Y-step	ω_0	F_{th}
515 nm	16 µJ	30 µm	35 µm	0.14±0.04 J/cm^2
1030 nm	84 µJ	40 µm	91 µm	0.24±0.03 J/cm^2

The values of the estimated beam radius ω_0 and the corresponding threshold fluence F_{th} are reported in Table 4.3, for both wavelengths. The peak fluence for the Gaussian beam can be calculated using $\mathrm{F_p} = (2\mathrm{E})/(\pi \mathrm{w}_0^2)$, where E is the pulse energy.

The experiments were carried out at both wavelengths in three different ambient conditions: ambient air, rough vacuum (p ≈ 4×10^{-3} mbar) and nitrogen at 1000 mbar. In each copper plate of 20 × 20 mm^2 laser surface structuring was carried out across an area of 8×8mm^2 with continuous bidirectional raster scan of the laser beam on the sample along the horizontal direction and a y-step distance along the vertical direction, at three selected scanning velocities V_s=1 mm/s, 1.5 mm/s and 2 mm/s. The corresponding effective number of overlapped pulse is estimated by $\mathrm{N_{eff}} = (2\omega_0 * \mathrm{RR})/V_s)$ [29], and the pulse overlap $(1 - \frac{1}{\mathrm{N_{eff}}})$ is set to be larger than 99%. The laser and processing parameters used in the surface structuring process are reported in Table 4.3. In all cases, the scanning direction was set parallel to laser polarization direction.

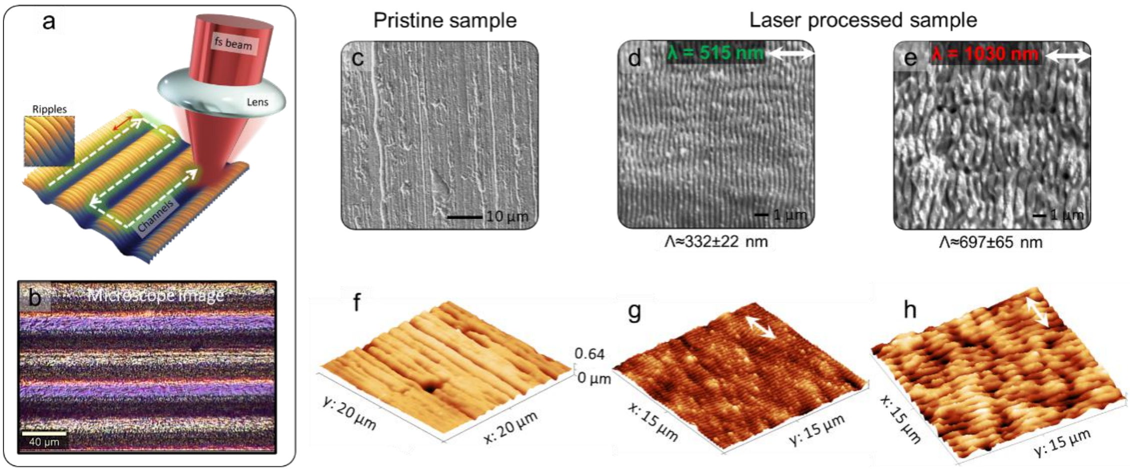

Fig.4.8 (a) Simple sketch of beam scanning over the target material and (b) microscope image of processed sample at V_s= 1 mm/s with fs pulses at 515 nm. SEM images of the copper surface before laser processing (c) and after irradiation in ambient air with fs pulses at (d) 515 nm and (e) 1030 nm, for V_s= 1 mm/s. AFM (3D view) images of the copper surface (f) before and after laser processing with fs pulses at (g) 515 nm and (h) 1030 nm. The double headed arrow indicates the direction of laser polarization.

To evaluate the change in the surface morphology, SEM and atomic force microscope (AFM) images of the copper surface before and after processing with fs pulses were acquired (see Fig. 4.8). A simple sketch of laser processing with bidirectional scanning is shown in Fig. 4.8(a). This process may generate two typical modulations on the irradiated surface, i.e. subwavelength ripples with preferential alignment perpendicular to the laser polarization as well as the larger order modulation or 'channels' along the scanning lines generated as a result of the Gaussian spatial distribution of the laser beam intensity, as sketched in the panel (a) of Fig. 4.8. The images of the structured surface corresponding to the sample treated in ambient air and at a beam scanning velocity of V_s = 1 mm/s are displayed in Fig. 4.8. A microscope image of the copper surface after dynamically irradiating with fs pulses 515 nm at a scanning speed V_s = 1 mm/s is reported in panel (b). The panel (c) shows the pristine condition of the Cu sample. As can be seen from the SEM image of the panel (c), the original rolled copper surface is rough with micron-sized non-uniformities. Panel (d) represents the sample surface processed with λ ≈ 515 nm generating LIPSS with an average spatial period of Λ ≈ (332 ± 22) nm. Panel(e) shows the LIPSS generated after irradiation with λ ≈ 1030 nm, whose spatial period is measured to be Λ ≈ (697 ± 65) nm. Likewise, panels (f-h) reveal the 3D representation of the copper surface obtained from AFM analysis, clearly showing the presence of sub-micron periodic ripples whose spatial period depends on the irradiation laser wavelength.

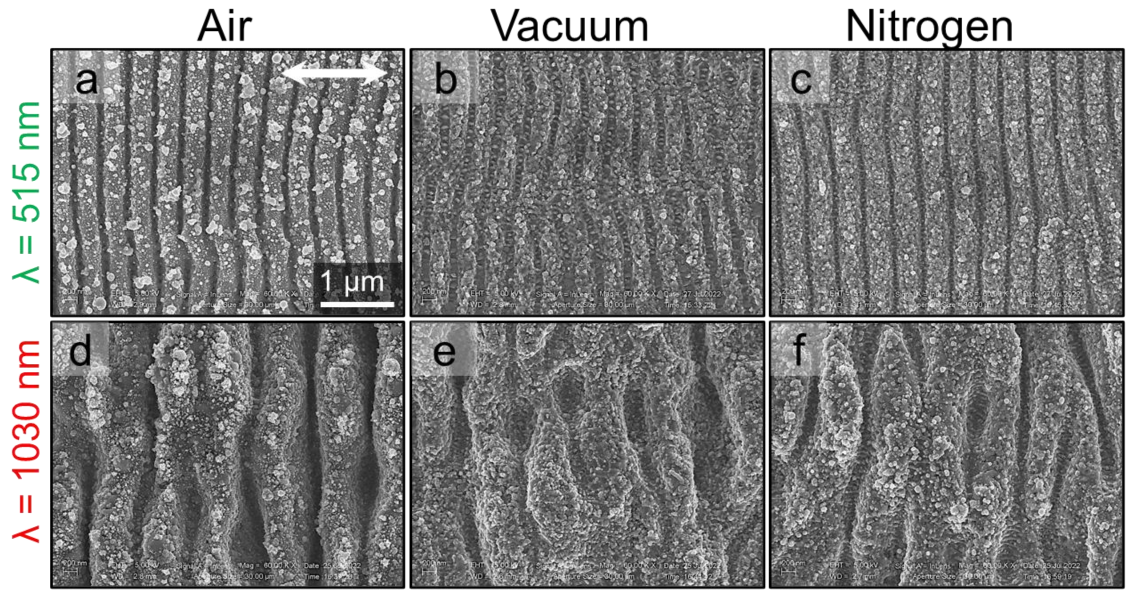

Fig. 4.9 SEM images including a comparison between LIPSS structuring generated with two different laser wavelengths (515 nm and 1030 nm), and in three different environments (air, vacuum, and nitrogen ambient). The structuring process was carried out with a scanning speed V_s = 1.5 mm/s. The double headed arrow in (a) indicates the laser beam polarization direction.

The influence of the processing environment is characterized for two irradiation wavelengths, while the laser processing was performed at three different scanning speeds, i.e. V_s = 1 mm/s, 1.5 mm/s and 2 mm/s. As the other processing parameters (pulse energy, repetition rate and spot size, see Table 4.3) are fixed, varying the beam scanning speed resulted in a change of the number of overlapping pulses. Fig. 4.9 reports SEM images of the sample surfaces for laser processing at 515 nm and 1030 nm, for ambient air, rough vacuum and nitrogen, for a scanning speed of 1.5 mm/s. The generation of ripples is more evident in the case of the sample processed in air.

In the case of λ ≈515 nm, besides ripples, SEM images seem to evidence a rougher surface in the case of air processing conditions. This can be ascribed to nanoparticle re-deposition, which is an obvious phenomenon in the case of fs laser ablation in air. In that sense, the rippled surface processed in vacuum and nitrogen environments look free from deposits of nanoparticles. However, in the case of vacuum and nitrogen ambient the ripples appear to be very shallow. Moreover, the SEM images evidenced other random modulations on the surface that could be due to the surface non-uniformities present on the original sample and the shallow ripples appeared to be generated over this rough surface. In the case of irradiation at λ ≈ 1030 nm, SEM images show a sample surface that in all three ambient conditions is rather free from nanoparticle debris.

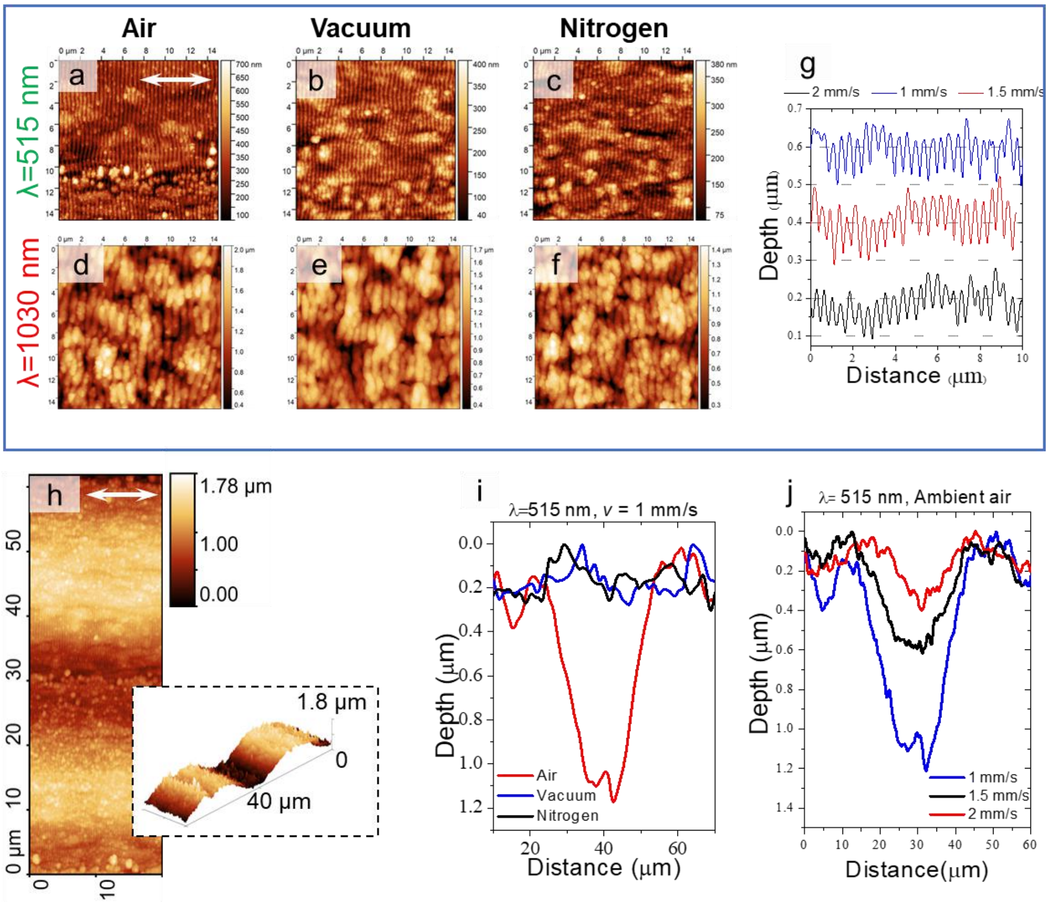

Fig. 4.10 Panels (a-f) show high-resolution AFM images of the copper surface after processing with 515 nm (a-c) and 1030 nm (d-f) laser light at V_s = 1.5 mm/s, for three ambient conditions. The double headed arrow indicates the direction of polarization of the incident laser beam. For the sample corresponding to λ = 515 nm and processed in ambient air, panel (g) shows the depth profile of surface ripples at three scanning velocities. The profiles are vertically shifted to facilitate the readiness. As an example, the low-resolution AFM image after processing with λ = 515 nm in ambient air at V_s = 1mm/s is given in (h) to showcase the surface waviness due to the large-scale modulation or channels from the laser raster scan lines. The inset shown in (h) represents the 3D view of the large-scale surface modulation. The depth profiles of this modulation are reported in panels (i-j) as function of the ambient conditions and of the scanning speed, respectively.

The AFM analyses give further information about the surface morphology. The analyses primarily show that there are two types of modulation on the copper surface. The first one is a fine modulation that covers the whole irradiated surface because of the generation of subwavelength ripples perpendicular to the laser polarization. Fig. 4.10 (a-f) report the high-resolution AFM images of the ripples obtained after irradiating with λ ≈ 515 nm and 1030 nm in three different ambient conditions at V_s= 1.5 mm/s. In all cases, the images evidence the presence of surface ripples.

The low-resolution AFM image reported in Fig. 4.10 (h), corresponding to copper processed with λ ≈ 515 nm in air at a scanning speed of 1 mm/s, shows the large-scale periodic modulation generated along the laser beam scan line. This shape is usually generated as a result of raster scanning with a Gaussian beam that leads to the formation of parallel channels along the scanning direction. These channels are comparatively deep at the region where the beam intensity is maximum and shallow near the edges, creating an overall waviness of the copper surface with a period equal to the distance of y-step. The inset shown in panel (h) displays the 3D view of the processed surface with trough and crest parts of the channel formed after beam scanning at 1 mm/s. As already mentioned, for all the samples the beam scanning direction is set along the direction of the laser beam polarization. So, these two different modulations, i.e. ripples and channels, are orthogonal to each other.

The depth profiles of the fine ripples for the case of $\lambda \approx 515$ nm and ambient air are reported in Fig. 4.10 (g) as function of the three examined scanning velocities. For the sake of convenience, the profiles are vertically shifted. There is no clear evidence of defined trends with respect to the scanning speed. Fig. 4.10 (i) and (j) exemplify the depth profile of the large-scale channels due to the laser beam Gaussian intensity profile for the case $\lambda \approx 515$ nm for the various the scanning velocities and ambient conditions. As the beam scanning velocity reduces from 2 to 1 mm/s, there is a clear increase in the groove depth from 0.38 μm to 1.1 μm when measured at the centre, where the laser beam intensity is maximum. Looking at Fig. 4.10 (j), it can be noted that the channels are very shallow for irradiation carried out in vacuum and in nitrogen ambient, even though the laser parameters are identical to that of irradiation in air ($\lambda \approx 515$ nm and 1 mm/s beam scanning velocity). This behaviour suggests a comparatively reduced ablation and material removal when the laser treatment is carried out in vacuum and nitrogen environments. So, an accurate depth of the channels can be measured only for the sample processed in air.

The spatial period of the surface ripples Λ has been measured both by SEM and AFM for all samples. In Table 4.4 the values obtained from SEM analyses of Fig. 4.9 are summarized for the different ambient conditions and scanning speeds. These reported values of ripples period agree with those obtained from AFM, within the uncertainties. As for the ripples, the period shows no trend with respect to the scanning speed and ambient conditions.

As mentioned before, the two orthogonal modulations present on the surface, i.e. the large-scale modulation or coarser channels along beam scan direction and the sub-wavelength ripples, should be analysed separately. For the channels, depth profiles obtained by AFM are reported in panels (i-j) of Fig. 4.10 and their depth values are listed in Table 4.4. Moreover, the surface roughness contribution due to the sub-wavelength ripples is estimated by calculating the RMS roughness parameter S_q from the AFM images. The parameter S_q is selected since the values are close to the actual measured peak-to-valley height of the ripples over any local selected area.

Table 4.4 The spatial period Λ of ripples generated on copper surface after irradiating with laser pulses at 515 and 1030 nm for different ambient conditions and scanning speeds as measured from the SEM images. The channel depth and surface roughness due to the sub-wavelength ripples generated by surface structuring with laser beam were extracted from the related AFM measurements. The surface roughness is determined by estimating an RMS value of the roughness parameter Sq for a scan area of 15×15 μm^2 using the *Gwyddion* software.

λ (nm)	V_s (mm/s)	Λ (nm)			Channel depth(μm)	RMS roughness S_q (nm)		
		Air	Vacuum	Nitrogen	Air	Air	Vacuum	Nitrogen
515	1	350±24	364±34	332±27	1.1±0.05	83±10	43±6	49±5
	1.5	341±23	375±24	361±25	0.51±0.02	73±6	49±6	41±4
	2	344±20	389±23	384±29	0.36±0.02	48±5	48±4	42±4
1030	1	697±65	647±49	622±66	0.61±0.03	334±19	202±10	218±17
	1.5	785±50	678±47	669±68	0.52±0.04	262±21	219±8	172±17
	2	809±42	707±43	674±59	0.30±0.03	185±11	259±18	181±11

The aspect ratio of these two surface modulations can be estimated separately by taking the ratio of the depth and the corresponding spatial period between two troughs or crust part of the modulations. For the channels, the aspect ratio is evaluated taking into account the y-step=30 μm for 515 nm and y-step=40 μm for 1030 nm, while for the ripples, the aspect ratio is defined as S_q/Λ.

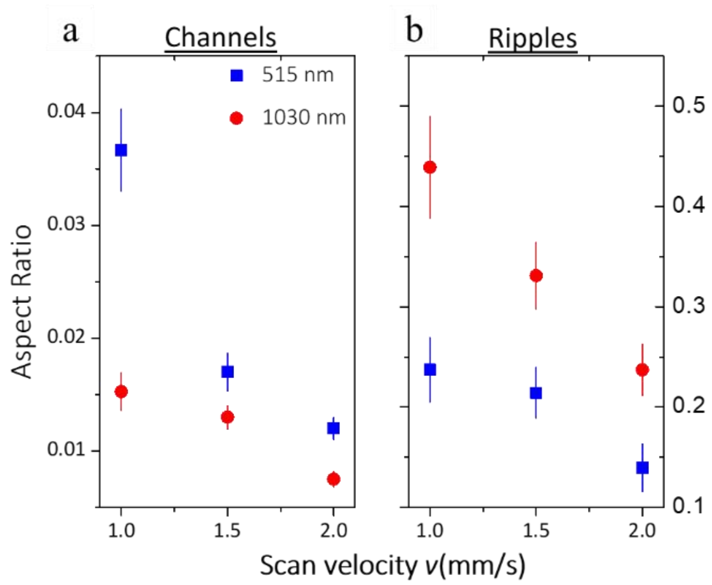

Fig. 4.11 Aspect ratio of (a) channels generated by the raster scanning with Gaussian beam and of (b) sub-wavelength ripples as a function of scanning velocity for the cases of irradiation at 515 nm and 1030 nm in ambient air.

The estimated aspect ratios for processing in air as a function of laser wavelength and scanning velocity are reported in Fig. 4.11. Fig. 4.11(a) shows a clear drop in the aspect ratio of the channels as the scanning velocity increases, especially for the case of λ ≈ 515 nm. For ripples, a decreasing trend of aspect ratio is found when the scan velocity increases from 1 to 2 mm/s. At both wavelengths and for the processing in either vacuum or nitrogen, no common trend in the aspect ratio is found, as can be seen from Table 4.5. Most notably, the number are much lower compared to the structures formed in air.

Table 4.5 The aspect ratio of the ripples generated on copper surface after irradiating with laser pulses at λ = 515 nm and 1030 nm in rough vacuum and nitrogen, for different scanning speeds.

Velocity (mm/s)	Aspect Ratio of ripples			
	515 nm		1030 nm	
	Vacuum	Nitrogen	Vacuum	Nitrogen
1	0.11±0.02	0.15±0.03	0.32±0.04	0.28±0.04
1.5	0.13±0.02	0.11±0.02	0.28±0.03	0.23±0.03
2	0.14±0.02	0.11±0.02	0.32±0.03	0.23±0.03

4.4 Conclusions

In this chapter the formation of LIPSS over a large area of a copper target was explored in experiments using a cylindrical and a spherical lens for the laser beam focusing. Moreover, the influence of the laser wavelength and ambient conditions were also analyzed in the latter case.

Our findings clearly evidence that the different degree of overlap of the Gaussian laser fluence distribution influence the final surface morphology and the features of the ripples spatial periods in the different zones. In addition, the analyses revealed that processing Cu with different ambient gas, laser wavelength and beam scanning velocity results in different values of spatial periods and RMS roughness. The experimental findings address interesting features related to the different processing strategies for large area evidencing a significant coverage of nanoparticles for the processing with cylindrical lens in the region of larger beam overlap during the scanning and the presence of two surface modulations, ripples and channels, for the processing with a spherical lens. Both aspects are relevant for large area processing of copper in view of exploitation of its functional properties.

Bibliography

[1] J. JJ. Nivas, M. Valadan, M. Salvatore, R. Fittipaldi, M. Himmerlich, M. Rimoldi, A. Passarelli, E. Allahyari, S. L. Oscurato, A. Vecchione, C. Altuccia, S. Amoruso, A. Andreone, S. Calatroni, M. R. Masullo. Secondary electron yield reduction by femtosecond pulse laser-induced periodic surface structuring. Surf. Interfaces 25 (2021) 101179. doi: https://doi.org/10.1016/j.surfin.2021.101179.

[2] O. Domínguez, K. Li, G. Arduini, E. Métral, G. Rumolo, F. Zimmermann, H. Maury Cuna. First electron-cloud studies at the Large Hadron Collider. Phys. Rev. Accel. Beams 16 (2013) 011033. https://doi.org/10.1103/PhysRevSTAB.16.011003.

[3] V. Shiltsev, F. Zimmermann. Modern and future colliders. Rev. Mod. Phys. 93 (2021) 015006. https://doi.org/10.1103/RevModPhys.93.015006.

[4] R. Cimino, T. Demma. Electron cloud in accelerators. Int. J. Mod. Phys. A 29 (2014) 1430023. https://doi.org/10.1142/S0217751X14300233.

[5] F. Zimmermann. Review of single bunch instabilities driven by an electron cloud. Phys. Rev. Accel. Beams 7 (2004) 121-156. https://doi.org/10.1103/PhysRevSTAB.7.124801.

[6] R. Valizadeh, O. B. Malyshev, S. Wang, S. A. Zolotovskaya, W. A. Gillespie, A. Abdolvand. Low secondary electron yield engineered surface for electron cloud mitigation. Appl. Phys. Lett. 105 (2014) 231605. https://doi.org/10.1063/1.4902993.

[7] S. Calatroni, E. G. Valdivieso, H. Neupert, V. Nistor, A. T. P. Fontenla, M. Taborelli, P. Chiggiato, O. Malyshev, R. Valizadeh, S. Wackerow, S. A. Zolotovskaya, W. A. Gillespie, A. Abdolvand. First accelerator test of vacuum components with laser-engineered surfaces for electron-cloud mitigation. Phys. Rev. Accel. Beams 20 (2017) 113201. https://doi.org/10.1103/PhysRevAccelBeams.20.113201.

[8] S. Calatroni, E. G. Valdivieso, A. T. P. Fontenla, M. Taborelli, H. Neupert, M. Himmerlich, P. Chiggiato, D. Bajek, S. Wackerow, A. Abdolvand. Optimization of the secondary electron yield of laser-structured copper surfaces at room and cryogenic temperature. Phys. Rev. Accel. Beams 23 (2020) 033101. https://doi.org/10.1103/PhysRevAccelBeams.23.033101.

[9] R. Valizadeh, O. B. Malyshev, S. Wang, T. Sian, M. D. Cropper, N. Sykes. Reduction of secondary electron yield for E-cloud mitigation by laser ablation surface engineering. Appl. Surf. Sci. 404 (2017) 370-379. https://doi.org/10.1016/j.apsusc.2017.02.013.

[10] R. Valizadeh, O. B. Malyshev, T. Sian, J. S. Colligon, Q. Li, W. Perrie. Laser Ablated Surface Engineerin : From Discovery to Machine Application. ECLOUD'18 Proceedings 7 (2020) 209-216. https://doi.org/10.23732/CYRCP-2020-007.209.

[11] J. Bonse, S. Hohm, S. V. Kirner, A. Rosenfeld, J. Krüger. Laser-Induced Periodic Surface Structures-A Scientific Evergreen. IEEE J. Sel. Top. Quantum Electron. 23 (2017) 9000615. https://doi.org/10.1109/JSTQE.2016.2614183.

[12] J. JJ. Nivas, K. K. Anoop, R. Bruzzese, R. Philip, S. Amoruso. Direct femtosecond laser surface structuring of crystalline silicon at 400 nm. Appl. Phys. Lett. 112 (2018) 121601. https://doi.org/10.1063/1.5011134.

[13] J. JJ. Nivas, E. Allahyari, F. Cardano, A. Rubano, R. Fittipaldi, A. Vecchione, D. Paparo, L. Marrucci, R. Bruzzese, S. Amoruso. Surface structures with unconventional patterns and shapes generated by femtosecond structured light fields. Sci. Rep. 8 (2018) 13613, https://doi.org/10.1038/s41598-018-31768-w.

[14] J. M. Liu. Simple technique for measurements of pulsed Gaussian-beam spot sizes. Opt. Lett. 7 (1982) 196-198. https://doi.org/10.1364/OL.7.000196.

[15] P. Gecys, E. Markauskas, M. Gedvilas, G. Raciukaitis, I. Repins, C. Beall. Ultrashort pulsed laser induced material lift-off processing of CZTSe thin-film solar cells. Sol. Energy 102 (2014) 82-90. https://doi.org/10.1016/j.solener.2014.01.013.

[16] J. Krüger, W. Kautek. Ultrashort Pulse Laser Interaction with Dielectrics and Polymers. Adv. Polym. Sci.168 (2004) 247-290. https://doi: 10.1007/b12683.

[17] D. Bouilly, D. Perez, L. J. Lewis. Damage in materials following ablation by ultrashort laser pulses: A molecular-dynamics study. Phys. Rev. B 76 (2007) 184119. https://doi.org/10.1103/PhysRevB.76.184119.

[18] J. C. Alonso, R. Diamant, P. Castillo, M. C. Acosta-García, N. Batina, E. Haro-Poniatowski. Thin films of silver nanoparticles deposited in vacuum by pulsed laser ablation using a yag: Nd laser. Appl. Surf. Sci. 255 (2009) 4933-4937. https://doi.org/10.1016/j.apsusc.2008.12.040.

[19] M. Quintana, E. Haro-Poniatowski, J. Morales, N. Batina. Synthesis of selenium nanoparticles by pulsed laser ablation. Appl. Surf. Sci. 195 (2002) 175-186, https://doi.org/10.1016/S0169-4332(02)00549-4.

[20] A. Talbi, A. Petit, A. Melhem, A. Stolz, C. B. Leborgne, G. Gautier, T. Defforge, N. Semmar. Nanoparticles based laserinduced surface structures formation on mesoporous silicon by picosecond laser beam interaction. Appl. Surf. Sci. 374 (2016) 31-35. https://doi.org/10.1016/j.apsusc.2015.09.003.

[21] A. Talbi, S. Kaya-Boussougou, A. Sauldubois, A. Stolz, C. B. Leborgne, Nadjib Semmar. Laser-induced periodic surface structures formation on mesoporous silicon from nanoparticles produced by picosecond and femtosecond laser shots. Appl. Phys. A 123 (2017) 463. https://doi.org/10.1007/s00339-017-1075-2.

[22] J. Bonse, J. Krüger. Pulse number dependence of laser-induced periodic surface structures for femtosecond laser irradiation of silicon. J Appl. Phys. 108 (2010) 034903. https://doi.org/10.1063/1.3456501.

[23] G. D. Tsibidis, A. Mimidis, E. Skoulas, S. V. Kirner, J. Krüger, J. Bonse, E. Stratakis. Modelling periodic structure formation on 100cr6 steel after irradiation with femtosecond-pulsed laser beams. Appl. Phys. A 124 (2017) 27. https://doi.org/10.1007/s00339-017-1443-y.

[24] M. Huang, F. Zhao, Y. Cheng, N. Xu, Z. Xu. Origin of laser-induced near-subwavelength ripples: interference between surface plasmons and incident laser. ACS nano. 3 (2009) 4062-4070. https://doi.org/10.1021/nn900654v.

[25] A. Naghilou, M. He, J. S. Schubert, L. V. Zhigilei, W. Kautek. Femtosecond laser generation of microbumps and nanojets on single and bilayer Cu/Ag thin films. Phys. Chem. Chem. Phys. 21 (2019) 11846-11860. https://doi: 10.1039/c9cp02174d.

[26] B. K. Nayak, M. C. Gupta. Self-organized micro/nano structures in metal surfaces by ultrafast laser irradiation. Opt. Lasers Eng. 48 (2010) 940-949. https://doi.org/10.1016/j.optlaseng.2010.04.010.

[27] Y. Nakata, T. Okada, M. Maeda. Nano-sized hollow bump array generated by single femtosecond laser pulse. Jap. J. Appl. Phys. 42 (2003) L1452-L1454. https://doi: 10.1143/JJAP.42.L1452.

[28] M. S. Rafique, S. Bashir, A. Ajami, W. Husinsky. Nonlinear absorption properties correlated with the surface and structural changes of ultrashort pulse laser irradiated cr-39. Appl. Phys. A 100 (2010) 1183-1189. https://doi.org/10.1007/s00339-010-5741-x.

[29] C. A. Zuhlke, G. D. Tsibidis, T. Anderson, E. Stratakis, G. Gogos, D. R. Alexander. Investigation of femtosecond laser induced ripple formation on copper for varying incident angle. AIP Adv. 8 (2018) 015212. https://doi.org/10.1063/1.5020029.

Chapter 5

Laser induced periodic surfaces structures in organic semiconductive films

This chapter reports some experimental results on the formation of laser induced periodic surface structures (LIPSS) on the surface of thin films of a semiconductor polymer by means of nanosecond (ns) laser vector vortex beams. The investigated polymers are poly(3-hexylthiophene) (P3HT) and a fullerene derivative [6,6]-phenyl C_{71}-butyric acid methyl ester ($PC_{71}BM$) deposited on a n-silicon[100], doped with arsenic, substrate. The work was carried out in the frame of a collaboration with Instituto de Química Física Rocasolano, CSIC (Madrid, Spain) aiming at addressing the LIPSS formation of polymer films with nanosecond and femtosecond laser pulses by vector vortex beams (VVBs). The first experiments reported here concerns the characterization of the periods and depth of the surface structures generated by ns pulses comparing the ones produced by VVBs to those generated for standard Gaussian beams.

5.1 Introduction

The interest in the study of organic materials such as semiconducting polymers and fullerenes has risen due to their potential applications in various fields, like optics, electronics, photovoltaics and so forth [1]. In particular, a semicrystalline polymer, poly(3-hexylthiophene) (P3HT), and a fullerene [6,6]-phenyl C_{71}-butyric acid methyl ester ($PC_{71}BM$), have been brought into the limelight for their possible use as the active layer in organic field-effect transistors (OFET) [2-4] and organic solar cells [5], due to their optical absorption in the visible range. On the other hand, a known method to improve the device performance of solar cells is the increase of the contact area between electron donor and acceptor. This is achieved by increasing the surface/volume ratio by creating nanostructures on the surface of the material. The most used methods for surface nanostructuring are lithographic techniques [6] that have great reproducibility and reliability, but usually need big infrastructures like clean rooms and complicated processes.

Laser-based techniques offer an alternative way and laser induced periodic surface structures (LIPSS) generation can be particularly attractive for their simplicity of fabrication in a one step process and simpler equipment requirements. As illustrated in Chapter 1, LIPSS are ripples that form when irradiating any material at a particular energy range, which were originally observed by Birnbaum [7] in 1965 using the ruby laser. The most accepted explanation for LIPSS generation by ns laser pulses was provided by Sipe theory [8-10] showing that, at normal incidence, LIPSS period is similar to the laser wavelength. Differently from other materials, for polymers the LIPSS show an orientation parallel to the laser polarization and for their formation the laser beam has to be enough energetic to heat the polymer above a temperature at which the polymer chains can flow [11], i.e. the glass or melting temperature for amorphous or crystalline polymers, respectively.

In previous works, the group at CSIC showed the possibility of LIPSS formation in P3HT [12] and $PC_{71}BM$ [13] with ns laser pulse irradiation, and how LIPSS also induced a modulation in the conductivity of the samples following the topography. The conductivity of the hills diminished due to a loss of crystallinity while the one of the valleys stayed intact.

The aim of the experiment, carried out at the Department of Physics Ettore Pancini of the University of Naples Federico II, was to investigate the formation of spatially variant LIPSS orientation induced by ns vector vortex beams (VVBs). VVBs also called beams carrying spin, are beams where the phase behaves like that of a Gaussian beam, but the polarization varies azimuthally. This variation in polarization induces a zero intensity at the center of the beam to avoid a singularity, giving an annular intensity spatial profile that can be described by a Laguerre-Gauss polynomial. Given that LIPSS follow the polarization of the beam, by using these beams with more complex polarization states more complex LIPSS can be produced, as has been shown in materials such as metals [14], semiconductors [15] and dielectrics [16].

In the following, Section 5.2 will summarize the polymer properties as well as the methods of experiments. In section 5.3, LIPSS on the surface of thin films of a semiconductor polymer P3HT are discussed. Then in section 5.4, we will address the LIPSS on the surface of thin films of a fullerene derivative $PC_{71}BM$.

5.2 Material characterization and experimental setup

$PC_{71}BM$ (Ossila UK) and P3HT (Ossila UK. M_w = 34 100 g/mol, PDI = 1.7, regioregularity = 94.7%) films were produced at CSIC and provided for the experiments. They were obtained by dissolving the pristine material in chlorobenzene and depositing thin films by spin coating over doped silicon substrates. A spinning rate of 2380 rpm for 120s in a Laurell WS-650 spin processor was used. The concentrations used were 20g/l for P3HT and

40g/l for $PC_{71}BM$. Table 5.1 summarizes the properties, measured by AFM, of the samples created this way and used in the experiments.

Table 5.1 Properties of the samples created by spin coating. The average of two measurements is shown as the result and their statistic deviation as the indetermination.

Material	P3HT	$PC_{71}BM$
Initial roughness Ra (nm)	3.65±0.07	0.45±0.07
Thin film Thickness (nm)	275±20	65±7
Substrate	Doped Si	Doped Si

The samples were irradiated with VVBs in ambient air under normal incidence. The laser source was a Quantel Brilliant-b Nd:YAG laser at 1064nm, frequency doubled to 532 nm, providing pulses with 5 ns duration (FWHM), at a repetition rate (RR) of 20 Hz. The pulse energy was controlled by a half-waveplate and a polarizer. Then, a commercial m=1 zero order vortex half-wave plate from Thorlabs was used to generate VVBs. The vortex wave plate turns linearly polarized Gaussian beams into different vector beams according to the angle of the incident polarization and the 0º fast axis of the vortex plate. We used vector beams with radial, azimuthal, and spiral polarization, which were generated with angles between the polarization of the input beam and the 0° fast axis of 0°, 90° and 45°, respectively. This plate also turns circularly polarized Gaussian beams into optical vortex beams. Therefore for the sake of completeness, we also carried out some irradiation with an optical vortex beam, which is an annular beam with a spatially uniform circular polarization and an azimuthally variant phase. Since the energy of the beam was more than enough to induce changes to the polymer films, the beam was non focused and a spot diameter of about 1 mm was selected by an appropriate iris. The characterization of the fluence of the vector beam was done measuring the power of the laser beam with a Gentec-e Maestro power meter and calculating the laser beam area with the method shown by Allahyari *et al.* [17].

The topography of the processed samples was characterized preliminary by optical miscroscopy at University of Naples and then by AFM at CSIC. A conductive AFM was used to measure the conductivity of the samples simultaneously to the topography. The tips were conductive tips Pt-Ir covered Si probes with a low spring constant, k = 0.2 N/m, SCM-PIC by Bruker. In C-AFM a voltage is applied between the sample holder and the AFM tip, and it measures the current that passes through. That is why we need a conductive substrate, and the samples were fixed to the holder with conductive tape.

5.3 LIPSS on the surface of thin films of a semiconductor polymer P3HT

This part is mainly for the LIPSS study of material P3HT with different laser polarization. The polymer P3HT was irradiated by VVBs with 1200 to 8400 pulses and 11 to 42 mJ/cm^2 for peak fluence (F_p). Given the size of our spots, to measure the period, depth and orientation of the structures, five 10x10μm^2 AFM images distributed along the spot as shown in Fig. 5.1, where selected. The AFM images of different areas of the spots and the orientation of the ripples with 6000 pulses at 23 mJ/cm^2 are displayed in Fig. 5.1. The structures formed by VVBs were parallel to the local orientation of the polarization of the laser beam creating wheel spokes-like structures for a radially polarized (Fig. 5.1(a)) VVBs, concentrical structures for an azimuthally polarized (Fig. 5.1(b)) VVBs, and whirlwind-like structures for a spirally polarized (Fig. 5.1(c)) VVBs. Regarding the influence of the fluence and number of pulses, we found that it is independent of the polarization of the VVB, and it is similar to the one with Gaussian beams found in previous papers [12].

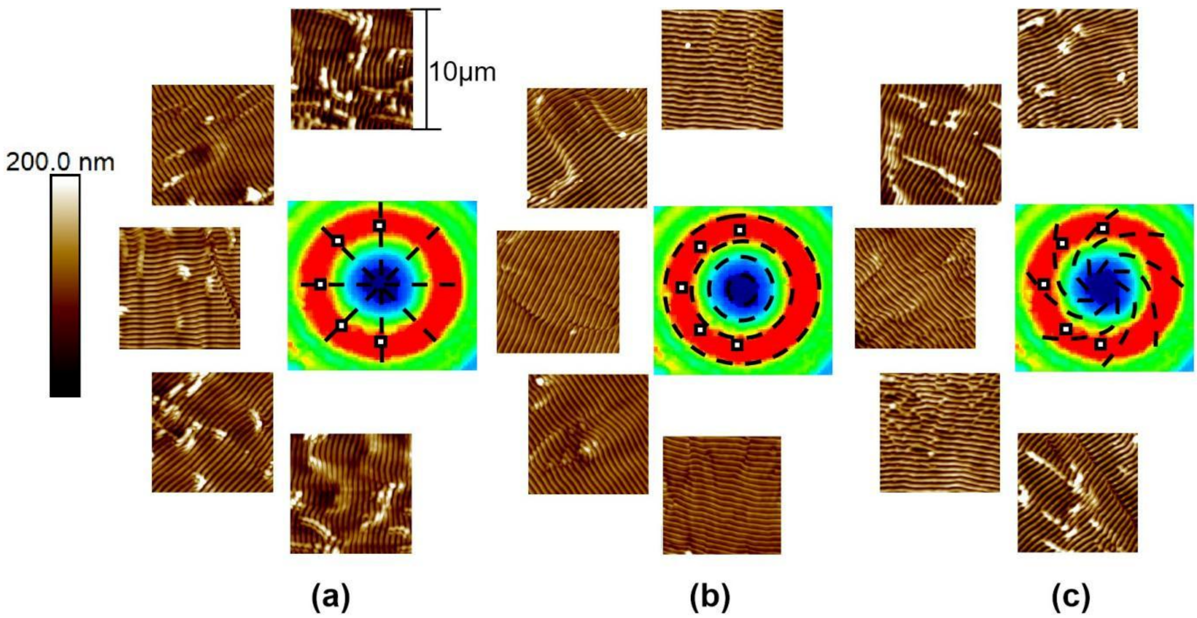

Fig. 5.1 Orientation of the structures in P3HT at different areas of the spot for radial (a), azimuthal (b) and spiral (c) vector beams for 6000 pulses at 23 mJ/cm^2.

In Fig. 5.2, LIPSS appeared in P3HT from 1200 to 8400 pulses with peak fluence from 11 to 42 mJ/cm^2. For the lowest number of pulses (N=1200), a fluence above 30 mJ/cm^2 was needed for LIPSS formation (green squares in the Fig. 5.2). For a number of pulses above 6000, the structures lost their periodicity above a fluence of 42 mJ/cm^2. This interplay between number of pulses and fluence is a consequence of the well-known accumulation effects involved in LIPSS formation. Their period grows from around 400 nm at lower fluences until it reaches a plateau around 475 nm at 30 mJ/cm^2, and their depth grows from 20 nm for lower fluence until it reaches a plateau that depends on the number of pulses at 30 mJ/cm^2, as seen in Fig. 5.2.

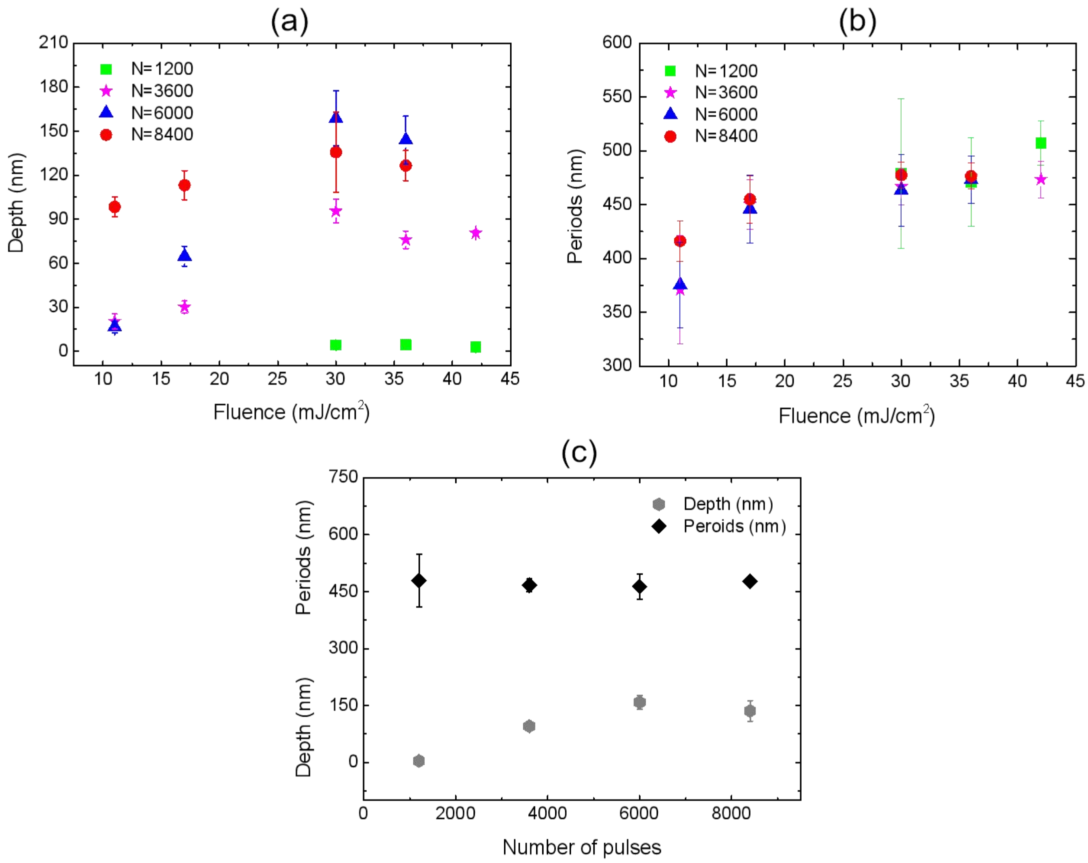

Fig. 5.2 Dependence of the depth (a) and periods (b) of the structures in P3HT with the fluence for different number of pulses. Panel (c) is the trend of structure periods and depth under different number of pulses at a fluence of 30 mJ/cm^2. All the polarization here are radial vector beams.

The structures generated by VVBs can be seen in Fig. 5.3 having honeycomb-like structures with a periodicity and depth close to that of the structures generated with vector beams in P3HT. For this fluences and number of pulses that corresponds to a period of 462$\pm$66 nm and a depth of 35$\pm$5 nm for P3HT, which seem to need a slightly higher fluence or pulse number for the formation of surface structures with VVBs.

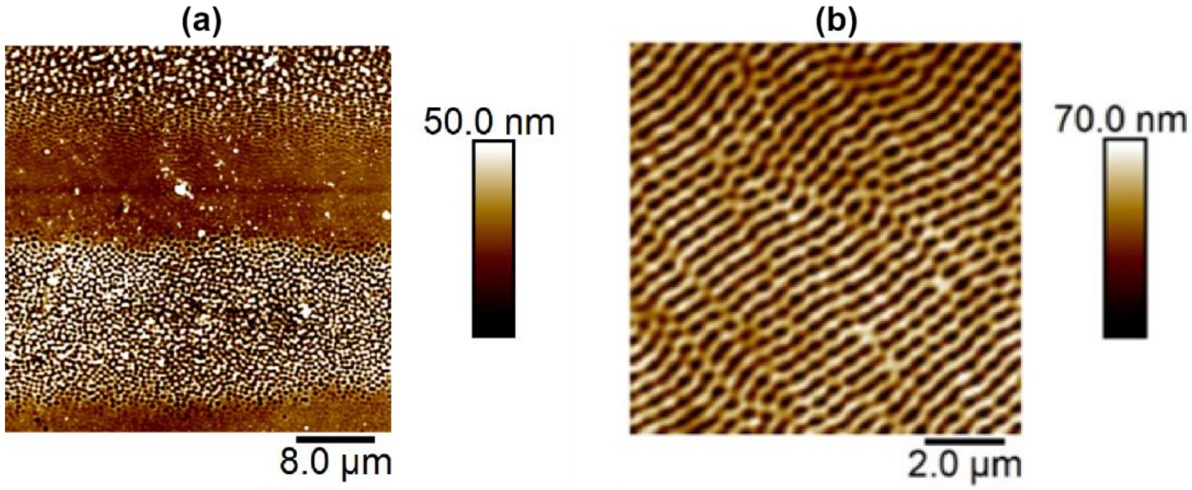

Fig. 5.3 Structures in P3HT for vortex beams for 6000 pulses at 42 mJ/cm^2.

5.4 LIPSS on the surface of thin films of a fullerene derivative PC$_{71}$BM

The main purpose of this section is to illustrate the features of the structures formed on the PC$_{71}$BM film after laser irradiation with VVBs and optical vortex beams. Firstly, we irradiated the fullerene derivative PC$_{71}$BM from 17 to 19 mJ/cm^2 for F_p with 1200 to 8400 pulses, since this is around the range where LIPSS appears. Similarly, for each polarized VVB, five 10 × 10 μm^2 AFM images are used to illustrate the orientations and characteristics of ripples generated in different areas. An example is shown in Fig. 5.4 for 6000 pulses at a laser peak fluence of 17 mJ/cm^2. It can be seen that also in this case the ripples morphological characteristics are similar to those reported above in Fig. 5.1: the ripples orientation follows the local direction of the laser polarization.

In PC$_{71}$BM LIPSS appeared from 1200 to 8400 pulses with a peak fluence from 17 to 19 mJ/cm^2. Their period is around 340 nm, and their depth grows from 55 nm at lower number of pulses until it plateaus at 100 nm for 6000 pulses, as seen in Fig. 5.5. In previous experiments with Gaussian beams, the LIPSS were observed in the same fluence and pulse number ranges, with similar depths and periods.

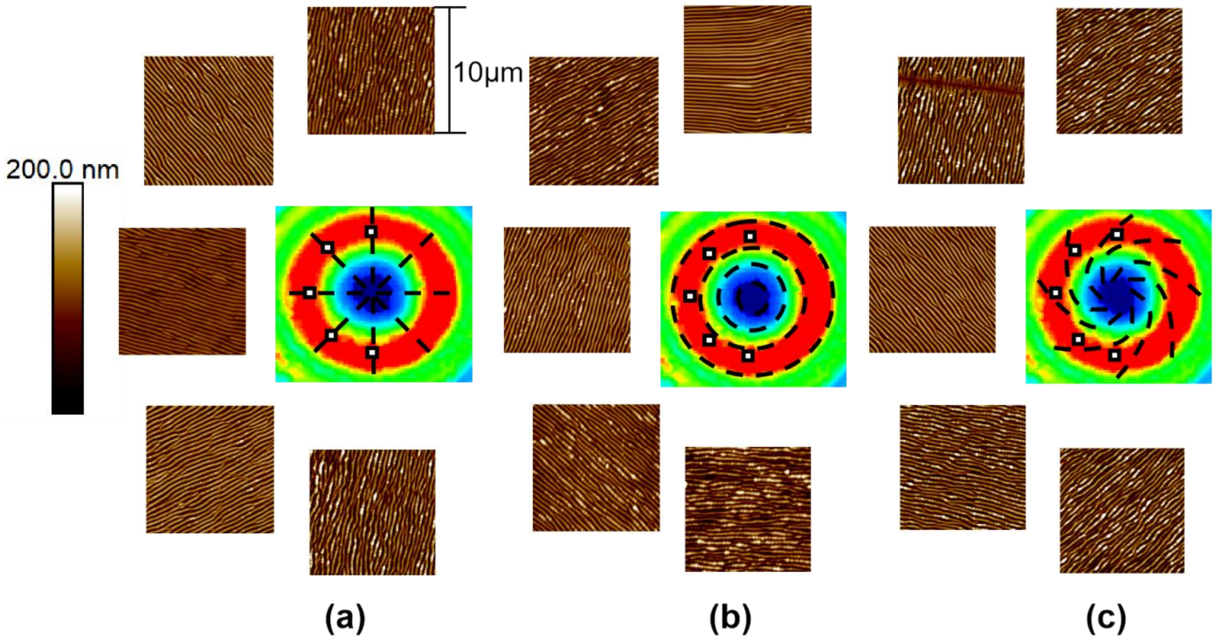

Fig. 5.4 Orientation of the structures in $PC_{71}BM$ at different areas of the spot for radial (a), azimuthal (b) and spiral (c) vector beams for 6000 pulses at 17 mJ/cm^2.

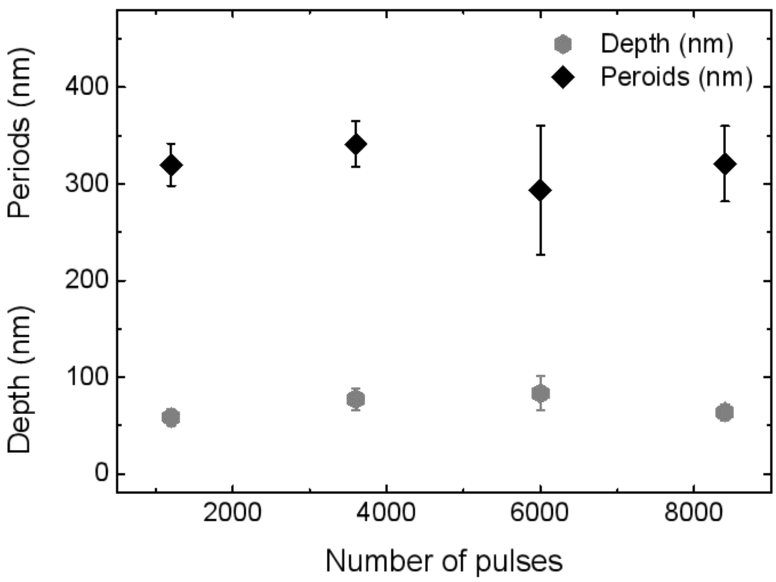

Fig. 5.5 Dependence of the depth and period of the structures in $PC_{71}BM$ with the number of pulses at a fluence of 17 mJ/cm^2.

In the end of this chapter, as depicted in Fig. 5.6, the structural characteristics of sample $PC_{71}BM$ generated by an optical vortex beam are discussed. Likewise the Gaussian case [13], they are honeycomb-like structures with a periodicity and depth close to that of the structures generated with vector beams. For these fluences and number of pulses the observed values are

390±50 nm for the periods and 70±15 nm for the depth. Compared with P3HT, the structures for $PC_{71}BM$ form for the same fluence and number of pulses as with VVBs, but for P3HT they seem to need a slightly higher fluence or pulse number.

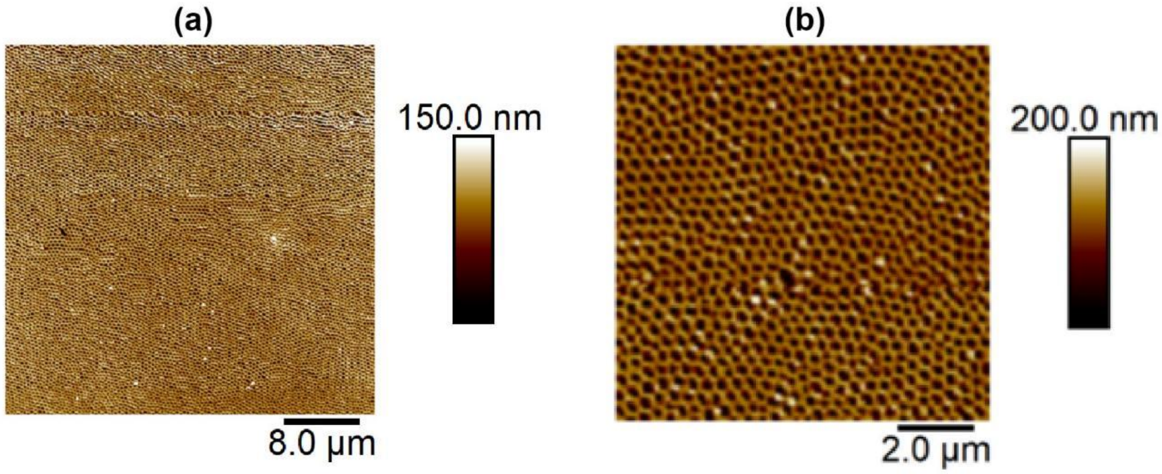

Fig. 5.6 Structures in $PC_{71}BM$ for vortex beams for 8400 pulses at 17 mJ/cm^2.

5.5 Conclusions

In this chapter, a preliminary investigation on LIPSS generation on thin films of a semiconductor polymer PH3T and a fullerene derivative $PC_{71}BM$ with VVBs with ns pulse duration were illustrated. Our findings show that the ripples orientation follows the local direction of the laser polarization so that spatially varying ripples can be produced on the sample surface. Moreover, the dependence of the LIPSS features for the two materials on the fluence and number of pulses is similar to that observed for the Gaussian case. Future investigation will be carried out to elucidate the effects of fs pulse duration comparing it with the more standard case of ns pulses.

Bibliography

[1] M. C. Scharber, N. S. Sariciftci. Low Band Gap Conjugated Semiconducting Polymers. Adv. Mater. Technol. 6 (2021) 2000857. https://doi.org/10.1002/ADMT.202000857.

[2] P. Lin, F. Yan. Organic Thin-Film Transistors for Chemical and Biological Sensing. Adv. Mater. 24 (2012) 34-51. https://doi.org/10.1002/ADMA.201103334.

[3] M. Yasin, T. Tauqeer, K. S. Karimov, S. E. San, A. Kösemen, Y. Yerli, A. V. Tunc. P3HT:PCBM blend based photo organic field effect transistor. Microelectron. Eng. 130 (2014) 13-17. https://doi.org/10.1016/J.MEE.2014.08.010.

[4] A. N. Aleshin, I. P. Shcherbakov, I. N. Trapeznikova, V. N. Petrov. Field-effect transistor structures on the basis of poly(3-hexylthiophene), fullerene derivatives [60]PCBM, [70]PCBM, and nickel nanoparticles. Phys. Solid State 58 (2016) 1882-1890. https://doi.org/10.1134/S1063783416090043.

[5] P. R. Berger, M. Kim. Polymer solar cells: P3HT:PCBM and beyond. J. Renew. Sustain. Energy. 10 (2018) 013508. https://doi.org/10.1063/1.5012992.

[6] A. Pimpin, W. Srituravanich. Review on Micro- and Nanolithography Techniques and Their Applications. Eng. J. 16 (2011) 37-56. https://doi.org/10.4186/ej.2012.16.1.37.

[7] M. Birnbaum. Semiconductor Surface Damage Produced by Ruby Lasers. J. Appl. Phys. 36 (1965) 3688-3689. https://doi.org/10.1063/1.1703071.

[8] J. E. Sipe, J. F. Young, J. S. Preston, H. M. Van Driel. Laser-induced periodic surface structure. I. Theory. Phys. Rev. B 27 (1983) 1141-1154. https://doi.org/10.1103/PhysRevB.27.1141.

[9] J. F. Young, J. S. Preston, H. M. Van Driel, J. E. Sipe. Laser induced periodic surface structure. II. Experimens on Ge, Si, Al and brass. Phys. Rev. B 27 (1983) 1155-1172. https://doi.org/10.1103/PhysRevB.27.1155.

[10] J. F. Young, J. E. Sipe, H. M. Van Driel. Laser-induced periodic surface structure. III. Fluence regimes, the role of feedback, and details of the induced topography in germanium. Phys. Rev. B 30 (1984) 2001-2015. https://doi.org/10.1103/PhysRevB.30.2001.

[11] E. Rebollar, T. A. Ezquerra, A. Nogales. Laser-induced periodic surface structures (LIPSS) on polymer surfaces. Wrinkled Polymer Surfaces-Strategies, Methods and Applications. Springer (2019) 143-155. https://doi.org/10.1007/978-3-030-05123-5_6.

[12] Á. Rodríguez-Rodríguez, E. Rebollar, M. Soccio, T. A. Ezquerra, D. R. Rueda, J. V. Garcia-Ramos, M. Castillejo, M. C. Garcia-Gutierrez. Laser-Induced Periodic Surface Structures on Conjugated Polymers: Poly(3-hexylthiophene). Macromolecules 48 (2015) 4024-4031. https://doi.org/10.1021/acs.macromol.5b00804.

[13] E. Gutiérrez-Fernández, Á. Rodríguez-Rodríguez, M. C. García-Gutiérrez, A. Nogales, T. A. Ezquerra, E. Rebollar. Functional nanostructured surfaces induced by laser on fullerene thin films. Appl. Surf. Sci. 476 (2019) 668-675. https://doi.org/10.1016/j.apsusc.2019.01.141.

[14] O. J. Allegre, W. Perrie, S. P. Edwardson, G. Dearden, K. G. Watkins. Laser microprocessing of steel with radially and azimuthally polarized femtosecond vortex pulses. J. Opt. 14 (2012) 085601. https://doi.org/10.1088/2040-8978/14/8/085601.

[15] J. JJ. Nivas, E. Allahyari, F. Cardano, A. Rubano, R. Fittipaldi, A. Vecchione, D. Paparo, L. Marrucci, R. Bruzzese, S. Amoruso. Vector vortex beams generated by q-plates as a versatile route to direct fs laser surface structuring. Appl. Surf. Sci. 471 (2019) 1028-1033. https://doi.org/10.1016/j.apsusc.2018.12.091.

[16] A. Papadopoulos, E. Skoulas, G. D. Tsibidis, E. Stratakis. Formation of periodic surface structures on dielectrics after irradiation with laser beams of spatially variant polarisation: a comparative study. Appl. Phys. A 124 (2018) 1-12. https://doi.org/10.1007/S00339-018-1573-X/FIGURES/9.

[17] E. Allahyari, J. JJ. Nivas, F. Cardano, R. Bruzzese, R. Fittipaldi, L. Marrucci, D. Paparo, A. Rubano, A. Vecchione, S. Amoruso. Simple method for the characterization of intense Laguerre-Gauss vector vortex beams. Appl. Phys. Lett. 112 (2018) 211103. https://doi.org/10.1063/1.5027661.

Chapter 6

Femtosecond laser surface structuring of Bi_2Te_3

In this chapter, we mainly illustrate the surface structuring induced by femtosecond laser ablation of a topological insulator (TI), namely a sample of Bismuth Telluride (Bi_2Te_3). The experiments are carried out at various peak fluence F_p and number of laser pulses N, and the morphology of the irradiated target area is analyzed. In normal parameters of fluence and pulses number, a regular ablation crater is formed on the surface of the Bi_2Te_3 sample. At specific fluences and number of pulses, the formation of ripples and surface structures is also observed also for this material that has not yet been investigated earlier.

6.1 Introduction

The generation of laser induced periodic surface structures (LIPSS) seems to be a rather ubiquitous phenomenon [1-10], however not yet investigated on every kind of material. It is well known that the material bandgap has an influential role in the formation of the surface structures generated by irradiation with fs laser pulses, especially at sub-ablation conditions [11-13]. In that perspective the laser irradiation of materials with special bandgap structure such as topological insulators (TI) are particularly exciting, but still poorly investigated. TI are fascinating materials with insulating bulk states and topologically protected metallic surface states characterized by Dirac dispersion and spin-momentum locking of carriers [14]. They are attractive materials for their peculiar properties when at low dimension and for thermoelectrics, and are mainly attractive for electronic, spintronic and photonic applications, where coupling of light to the topologically protected surface carriers may unveil several exotic phenomena [15-16]. Moreover, the distinct saturable absorption properties of layered TI open up their use in mode locked fiber lasers for fs pulse generation across the visible, near-infrared, and mid-infrared wavelengths by tuning the layer thickness [17].

Investigation of the effects of irradiation of topological insulator with fs laser pulses is particularly interesting to exploit the possibilities offered by laser patterning and direct writing approaches for the modification of target surface and development of functional materials. However, this topic remains still scarcely investigated. There are only very few reports on laser irradiation of Bismuth Telluride (Bi_2Te_3) or other TI. The selective ablation and direct writing on thick films of n-type Bi_2Te_3 and p-type Sb_2Te_3 using laser pulses at $\lambda =$ 343 nm and 290 fs has been reported by Zhou *et al*., who analyzed the threshold fluence and optimization for selective etching [18]. In another investigation, Yue *et al*. reported result on laser induced photoexcitation of thin film of Bi_2Te_3 with 100 fs pulses at 800 nm [19].

In this chapter, section 6.2 discusses the experimental setup used for the experiments on fs laser surface structuring of TI. Then, the preliminary results on the generation of periodic surface structures on a topological insulator material, Bi_2Te_3, are illustrated in section 6.3.

6.2 Experimental set up

Laser irradiation and surface structuring of a Bi_2Te_3 is carried out by different sequences of N pulses ($1 \leq \mathrm{N} \leq 1000$) at different peak fluences F_p ($0.08\ \mathrm{J/cm^2} < F_p < 1.01\ \mathrm{J/cm^2}$) , at a repetition rate (RR) of 100 Hz. The experimental setup was illustrated in Chapter 3, and for the experiments reported here the laser source used is the Ti:Sapphire laser (Legend, Coherent Inc.) delivering linearly polarized ≈ 35 fs pulses at a central wavelength around 800 nm. The target was a piece of Bi_2Te_3 cleaved from a single crystal grown in a floating zone image furnace. A Gaussian beam is focused on the target surface at normal incidence in air, by means of a plano-convex lens with a nominal focal length of 75 mm. The laser pulse energy (peak fluence) is varied by means of a system of half-wave plate and polarizer. The sample is mounted on the computer controlled two-axis motorized piezo stage, which is synchronized with the electromechanical shutter and controlled by a custom software in order to provide the required number of pulses N at any selected target location.

The crater generated on the sample surface is characterized by field emission scanning electron microscopy (FE-SEM). SEM images are typically acquired by registering secondary electrons (SE) with an Everhart-Thornley (ET) type detector. In some cases, also the In-Lens (IL) detector is used. The SEM images are analyzed using the software *Gwyddion* [20] and the periodic features of surface modulations are ascertained both visually and through 2-dimensional Fast Fourier transform (2D-FFT).

6.3 Result and discussion

Hereafter, we will illustrate the specific characteristics of ripples formed on Bi_2Te_3 as well as the influence of peak fluence F_p and pulse number N on their morphological features. Finally, the variation trend of ripples periods and annular regions will be also discussed.

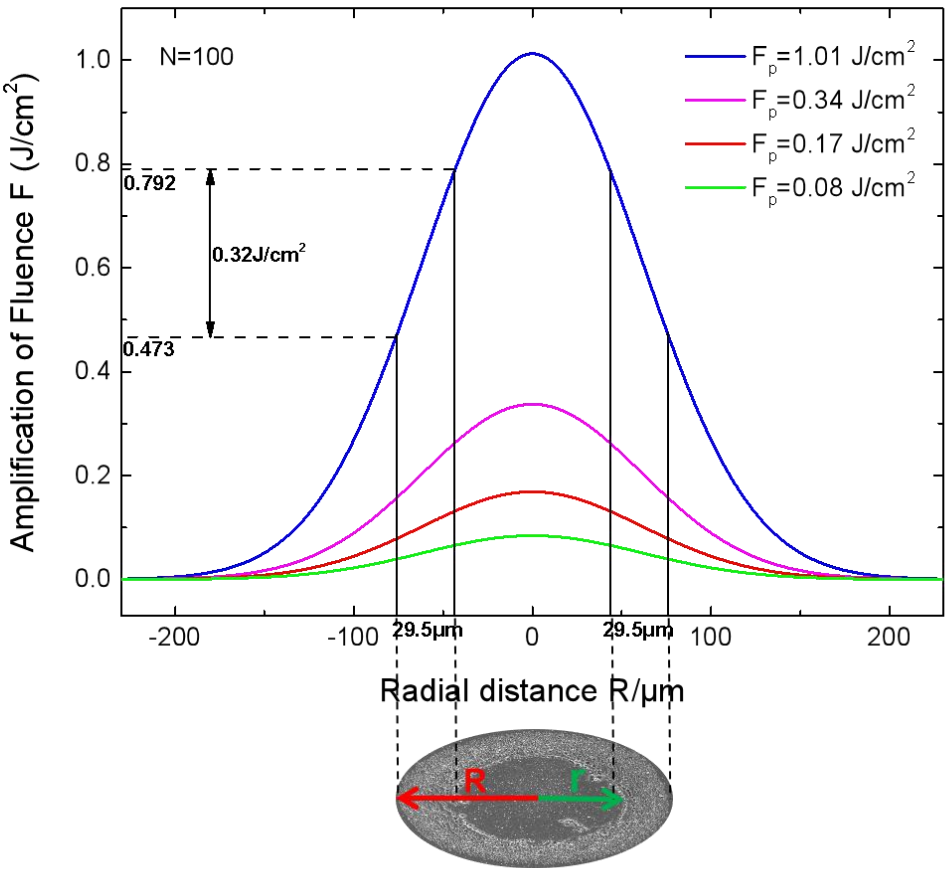

Fig. 6.1 Gaussian spatial profiles of the laser pulse fluence at four different peak fluence values, and expemplificative SEM image of the Bi_2Te_3 target registered for F_p=1.01 J/cm^2 and N=100.

Fig. 6.1 reports a graph of the Gaussian profiles of the laser pulse fluence at four different peak fluence. The exemplificative SEM image in the bottom part, referring to N=100 and F_p=1.0 J/cm^2 shows the formation of two regions with different morphological features with a central part surrounded by an annulus. The width of the annular region can be obtained as $\mathrm{R} - \mathrm{r} = 29.5\ \mu\mathrm{m}$, where R and r represent the radius of the crater and of the central region, respectively. As indicated in Fig. 6.1, the laser fluence value at R is $\approx$0.47 J/cm^2, while the laser fluence corresponding to the central region r is $\approx$0.79 J/cm^2. Their difference of 0.32 J/cm^2 is the range of laser fluence values associated to the annular region. Interestingly, for such experimental parameters, the ripples only forms in the annular region, whereas at lower laser pulse energy they cover the central part of the shallow crater. The variation of the crater morphology with the experimental parameters F_p and N will be illustrated below.

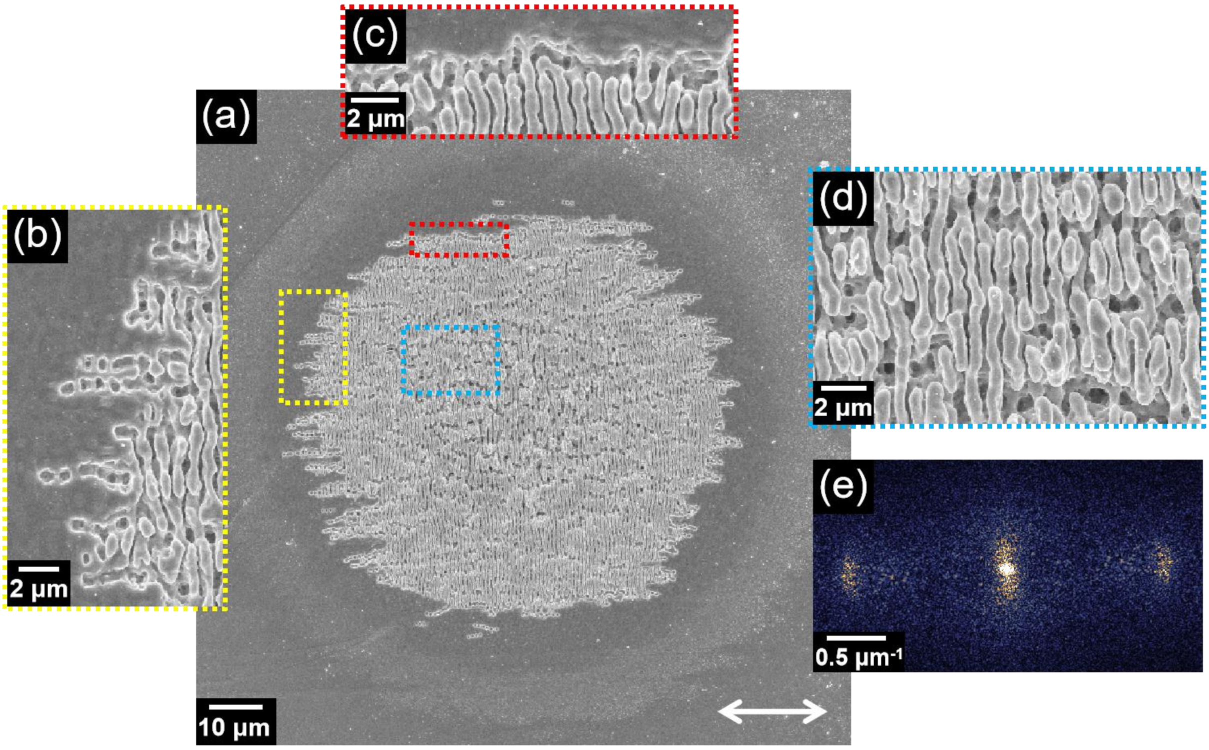

Fig. 6.2 The SEM images of the Bi_2Te_3 after irradiation with N=1000 with a pulse energy $F_p = 0.084$ J/cm^2 showing the formation of subwavelength LIPSS in the central part of the shallow crater. Panels (b), (c) and (d) display zoomed SEM images of the surface ripples. Panel (e) reports 2D-FFT of the structured spot. The double headed arrow in panel (a) indicates the direction of laser polarization.

Fig. 6.2 reports the SEM image of the Bi_2Te_3 surface after irradiation with N=1000 laser pulses at a peak fluence of F_p=0.084 J/cm^2. The formation of subwavelength LIPSS in the central part of the irradiated area is clearly evidenced. Even though the incident beam has a Gaussian intensity profile, the crater appears to be slightly more elongated along the horizontal direction with a comparatively rougher edge in comparison to that of the vertical direction. This is clearly discerned by the zoomed views of the crater edge and periodic ripples presented in panels (b) and (c). A shallow ring is found to be present around the actual crater coming from the redeposition of nanoparticles. In the presented irradiation condition, the period of the ripples obtained from the SEM image by the direct measurement is found to be 714±75 nm. The 2D-FFT analysis of the structured spot is given in panel (e) of Fig. 6.2. The period of ripples estimated from the 2D-FFT is 735±42 nm, consistent with the direct measurement. From the high-resolution SEM image, the ripples appear to be well developed without any significant decoration of nanoparticles over the ‘rippled’ area. Furthermore, around the centre of the crater, where the local fluence is maximum, the ripples appear to be thicker and more disconnected into individual units of short ripples, as can be seen from panel (d) of Fig. 6.2.

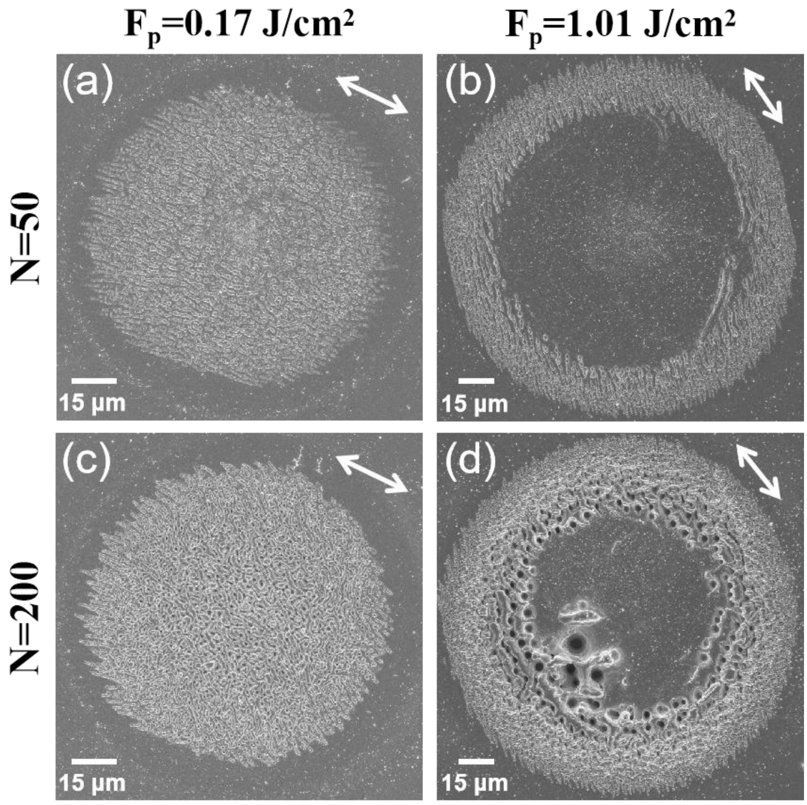

Fig. 6.3 SEM images at two different peak fluences and number of laser pulses demonstrating the annular formation of surface features as the peak fluence of laser increases (see panels (b) & (d)), whereas more regular craters are generated at low fluence, as depicted in panels (a) & (c). The double headed arrow indicates the direction of linear polarization of the laser beam.

The morphology of the Bi_2Te_3 surface after irradiation with two different number of pulses N and peak fluences F_p are shown in Fig. 6.3. Panels (a) and (c) report the case in which the surface is irradiated with a low peak fluence of 0.17 J/cm^2 for N=50 and N=200. Instead, panels (b) and (d) show the SEM images corresponding to the same values of N at peak fluence of 1.0 J/cm^2. In the former case at 0.17 J/cm^2, an almost circular crater with periodic ripples is observed for both irradiation conditions depicted in panels (a) and (c) of Fig. 6.3. Instead, at F_p=1.0 J/cm^2, the SEM images evidence the formation of an annular rippled region surrounding a central area without significant formation of LIPSS, even though the beam has a Gaussian intensity profile.

More evidence on the unusual evolution of the morphological features of the Bi_2Te_3 target surface with the experimental parameters N and F_p is summarized in Fig. 6.4. Here, panels (a-d) report SEM images of the surface irradiated with a peak fluence of F_p=1.0 J/cm^2 with different number of pulses from N=10 to N=500. It is evident that the annular rippled region is formed in all conditions except when N reaches rather high values, as for example N=500 in Fig. 6.4. As shown in panel (i), the width of the annular rippled area progressively increases with N. At this peak fluence, width of the rippled region shown in panel (i) tends to level off for N>200. Moreover, the crater takes the shape of a regular circular spot generally produced by strong laser ablation, following irradiation with a beam characterized by a Gaussian intensity profile at N=500.

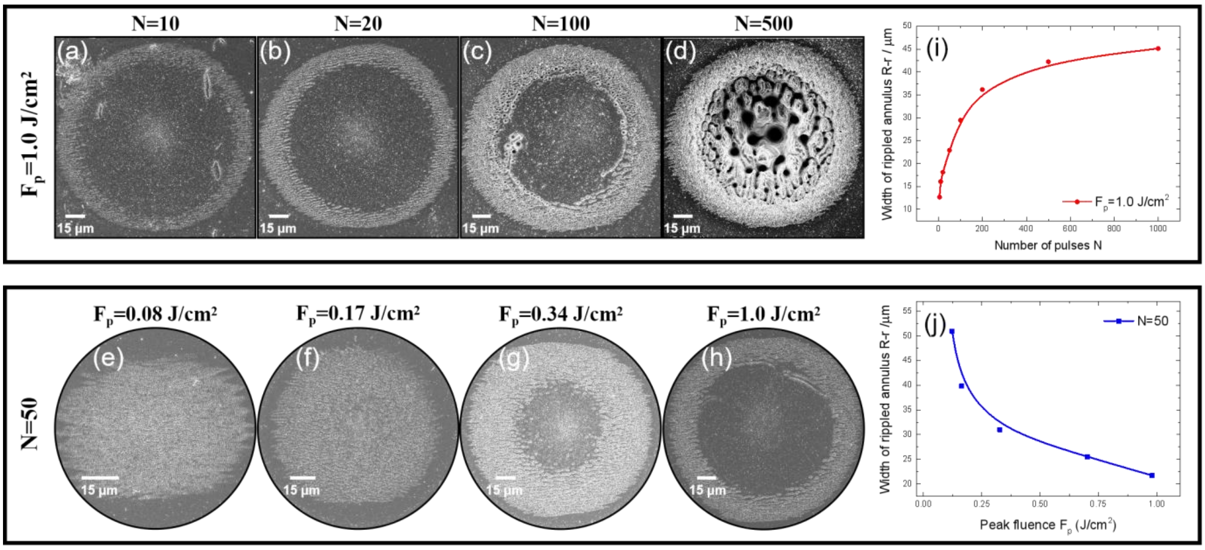

Fig. 6.4 SEM images of the Bi_2Te_3 target surface at different peak fluence F_p and number of laser pulses N showing the evolution of the morphological changes with the experimental parameters. In the upper part, the peak fluence is fixed at 1.0 J/cm^2 and the number of pulses varies from N=10 to N=500. The lower part shows the variation as a function of the peak fluence, from 0.08 J/cm^2 to 1.0 J/cm^2, at a fixed number of pulses N=50. The panels on the right display the variation of the width of the annular rippled area (R-r) with respect to number of irradiated pulses at F_p=1.0 J/cm^2 (i) and the peak fluence at N=50 (j), respectively. The variation of the width (R-r) of the rippled annulus was obtained by measuring the inner and outer circles delimiting the two regions.

The lower part of Fig. 6.4 illustrates the variation of the crater formed at different peak fluences, ranging from 0.08 J/cm^2 to 1.0 J/cm^2, for irradiation with 50 laser pulses. At relatively lower number of pulses the ripples are formed over an area with an elliptical shape due to the increased formation of ripples along horizontal direction. This effect gradually reduces as the peak fluence increases, resulting already into an almost circular crater with subwavelength ripples at F_p=0.17 J/cm^2, as can be seen in panel (f). However, further increase in the peak fluence results in the formation of ripples over an annular region, as displayed in panels (g-h). In this case, the SEM images show a circular centre region decorated by nanoparticles but without any ripples. Another noticeable change is the reduction of the width of the rippled annular region as the peak fluence increases, in the investigated range of peak fluences. This indicates that in Bi_2Te_3 ripple formation is supported only within a limited region of excitation; however, as it goes beyond a limit, a deep crater representing the intensity distribution is formed. The evolution of the annular spot width as a function of the pulse energy for N=50 is shown in panel (j) of Fig. 6.4. It clearly shows a reducing trend in the width of the annular rippled area, i.e., the region marked in between internal and external regions, as the peak fluence increases.

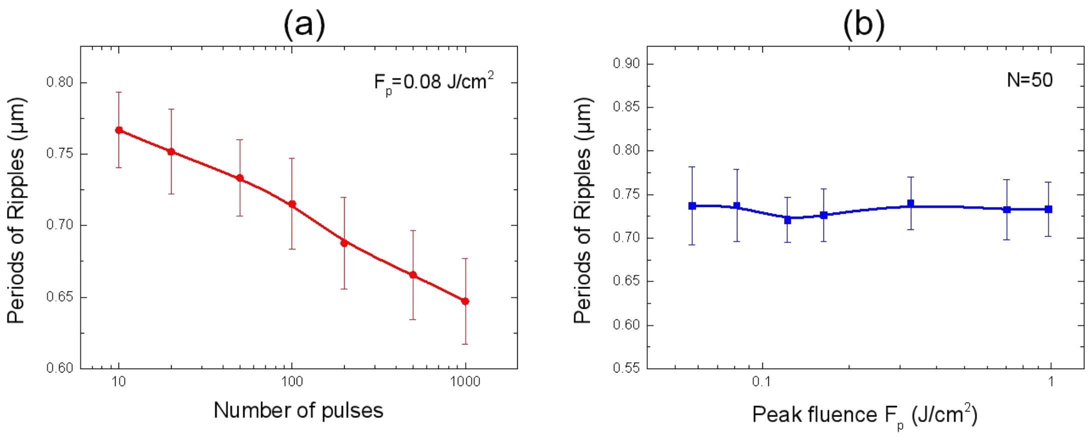

Fig. 6.5 The variation in ripples period with respect to number of pulses (a) and fluence (b), respectively.

Panels (a) and (b) in Fig. 6.5 report the variation of the ripples period as a function of number of pulses N and peak fluence F_p, respectively. In panel (a), the selected peak fluence is F_p=0.08 J/cm^2, corresponding to a condition where ripples cover the central part of the irradiated area. One can clearly observe a decrease of the ripples period on N also for the case of a topological insulator. Meanwhile there are no considerable change in the ripple period with respect to the peak fluence of laser. These characteristics are consistent with the general trends of ripples generated in semiconductors after irradiation with fs pulses.

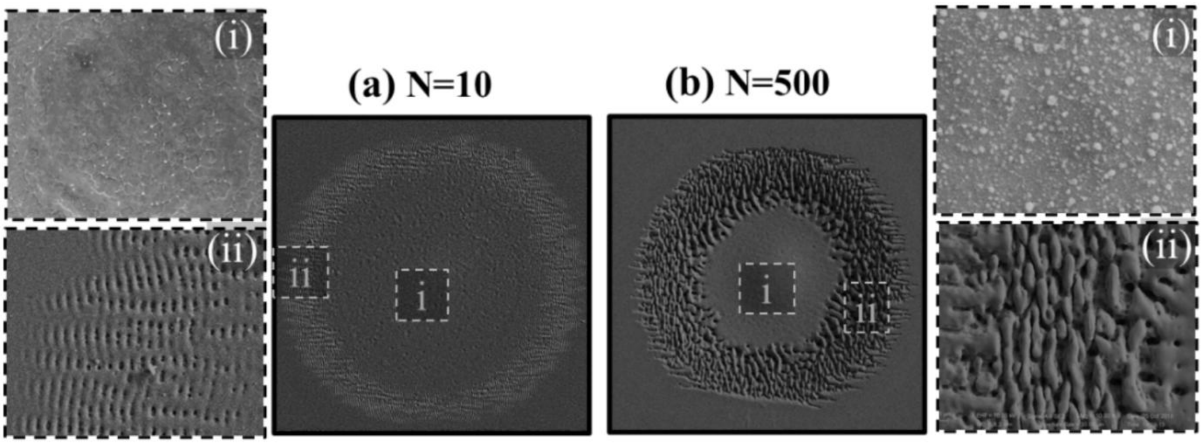

Fig. 6.6 SEM images after irradiation with (a) N=10 and (b) N=500 at the peak fluence of F_p=0.25 J/cm^2. The inset panels show the zoomed view of the annular crater at the (i) centre and (ii) edge of the respective spot.

Fig. 6.6 report the SEM images of the surface after irradiation with N=10 and N=500, at a peak fluence of F_p=0.25 J/cm^2, demonstrating the annular formation of the ripples. Zoomed views of the two different regions are displayed: (i) centre of the annular region without any periodic surface structure formation; (ii) edge region, consisting of periodic ripples. We find that when N is as large as 500, the ripples in the annular area are deeper and have a smaller period. Moreover, the ripples regularity becomes lower at higher values of the pulse number.

6.4 Conclusions

This chapter mainly summarizes the formation of periodic ripples on TI (Bi_2Te_3) induced by fs laser ablation. After analysis, the shallow crater appears to be more elongated in the direction of the laser polarization. Interestingly, annular rippled areas form in a given range of number of laser pulses and laser peak fluence. The width of rippled annular region shows an increasing trend on the laser pulse number, and a behaviour almost independent on the peak fluence.

The formation of subwavelength periodic surface structures on Bi_2Te_3 or in any other topological insulators has not been reported yet in the literature. Our preliminary investigation, carried out in the course of this thesis, clearly shows the formation of periodic ripples on topological insulator oriented along the direction perpendicular to the laser polarization, but evidence novel features at higher excitation as the absence of well-defined structures in an intermediate region of the (F_p , N) parameters values before reaching the usual deep ablation crater formed by strong ablation after multipulse irradiation at high pulse energy conditions. This aspect will deserve further future investigations.

Bibliography

[1] J. Bonse, S. Höhm, S. V. Kirner, A. Rosenfeld and J. Krüger. Laser-Induced Periodic Surface Structures-A Scientific Evergreen. IEEE J. Sel. Top. Quantum Electron. 23 (2017) 9000615. https://doi.org/10.1109/JSTQE.2016.2614183.

[2] K. Sugioka, Y. Cheng. Ultrafast Lasers-Reliable Tools for Advanced Materials Processing. Light Sci. Appl. 3 (2014) e149. https://doi.org/10.1038/lsa.2014.30.

[3] A. Y. Vorobyev, C. Guo. Direct Femtosecond Laser Surface Nano/Microstructuring and Its Applications. Laser Photonics Rev. 7 (2013) 385-407. https://doi.org/10.1002/lpor.201200017.

[4] M. Hu, J. JJ. Nivas, R. Fittipaldi, S. Amoruso. Femtosecond laser surface structuring of silicon in dynamic irradiation conditions. Opt. Laser Technol. 156 (2022) 108594. https://doi.org/10.1016/j.optlastec.2022.108594.

[5] M. Hu, J. JJ. Nivas, M. Valadan, R. Fittipaldi, A. Vecchione, R. Bruzzese, C. Altucci, S. Amoruso. Ultrafast laser surface irradiation of silicon: effects of repetition rate in vacuum and air. Appl. Surf. Sci. (2022) 154869. https://doi.org/10.1016/j.apsusc.2022.154869.

[6] E. Stratakis, J. Bonse, J. Heitz, J. Siegel, G. D. Tsibidis, E. Skoulas, A. Papadopoulos, A. Mimidis, A. C. Joel, P. Comanns, J. Krüger, C. Florian, Y. Fuentes-Edfuf, J. Solis, W. Baumgartner. Laser Engineering of Biomimetic Surfaces. Mater. Sci. Eng. R Rep. 141 (2020) 100562. https://doi.org/10.1016/j.mser.2020.100562.

[7] J. Bonse, S. Gräf. Maxwell Meets Marangoni-A Review of Theories on Laser-Induced Periodic Surface Structures. Laser Photon. Rev. 14 (2020) 2000215. https://doi.org/10.1002/lpor.202000215.

[8] J. JJ. Nivas, E. Allahyari, S. Amoruso. Direct femtosecond laser surface structuring with complex light beams generated by q-plates. Adv. Opt. Technol. 9 (2020) 53-56. https://doi.org/10.1515/aot-2019-0067.

[9] K. C. Phillips, H. H. Gandhi, E. Mazur, S. K. Sundaram. Ultrafast Laser Processing of Materials: A Review. Adv. Opt. Photonics 7 (2015) 684-712. https://doi.org/10.1364/AOP.7.000684.

[10] F. A. Müller, C. Kunz, S. Gräf. Bio-Inspired Functional Surfaces Based on Laser-Induced Periodic Surface Structures. Materials 9 (2016) 476. https://doi.org/10.3390/ma9060476.

[11] A. Okano, J. Kanasaki, Y. Nakai, N. Itoh. Electronic processes in laser-induced Ga0 emission and laser ablation of the GaP(110) and GaAs(110) surfaces. J. Phys.: Condens. Matter 6 (1994) 2697-2712. https://doi.org/10.1088/0953-8984/6/14/008.

[12] S. Höhm, A. Rosenfeld, J. Krüger, J. Bonse. Laser-induced periodic surface structures on zinc oxide crystals upon two-colour femtosecond double-pulse irradiation. Phys. Scr. 92 (2017) 034003. https://doi.org/10.1088/1402-4896/aa5578

[13] D. Puerto, W. Gawelda, J. Siegel, J. Bonse, G. Bachelier, J. Solis. Transient reflectivity and transmission changes during plasma formation and ablation in fused silica induced by femtosecond laser pulses. Appl. Phys. A 92 (2008) 803-808. https://doi.org/10.1007/s00339-008-4586-z.

[14] M. Z. Hasan, C. L. Kane. Colloquium: Topological Insulators. Rev. Mod. Phys. 82 (2010) 3045-3067. https://doi.org/10.1103/REVMODPHYS.82.3045/FIGURES/20/MEDIUM.

[15] Y. Chen, L. Xu, J. Li, Y. Li, H. Wang , C. Zhang, H. Li, Y. Wu, A. Liang, C. Chen, S. Jung, C. Cacho, Y. Mao, S. Liu, M. Wang, Y. Guo, Y. Xu, Z. Liu, L. Yang, Y. Chen. Topological Electronic Structure and Its Temperature Evolution in Antiferromagnetic Topological Insulator MnBi2Te4. Phys. Rev. X 9 (2019) 041040. https://doi.org/10.1103/PhysRevX.9.041040.

[16] A. B. Khanikaev, S. H. Mousavi, W. Tse, M. Kargarian, A. H. MacDonald, G. Shvets. Photonic topological insulators. Nat. Mate 12 (2013) 233-239. https://doi.org/10.1038/nmat3520.

[17] S. Mondal, R. Ganguly, K. Mondal. Topological Insulators: An In-Depth Review of Their Use in Modelocked Fiber Lasers. Ann. Phys. 533 (2021) 2000564. https://doi.org/10.1002/ANDP.202000564.

[18] J. Zhou, W. Zhu, Y. Xie, Y. Yu, Z. Guo, Q. Zhang, Y. Liu, Y. Deng. Rapid Selective Ablation and High-Precision Patterning for Micro-Thermoelectric Devices Using Femtosecond Laser Directing Writing. ACS Appl. Mater. Interfaces 14 (2022) 3066-3075. https://doi.org/10.1021/ACSAMI.1C21326/SUPPL_FILE/AM1C21326_SI_002.MP4.

[19] Z. Yue, Q .Chen, A. Sahu, X. Wang, M. Gu. Photo-Oxidation-Modulated Refractive Index in Bi2Te3 Thin Films. Mater. Res. Express 4 (2017) 126403. https://doi.org/10.1088/2053-1591/AA9C94.

[20] Gwyddion - A modular program for SPM (scanning probe microscopy) data visualization and analysis. http://gwyddion.net/.

Conclusions

The main topic of this thesis is fs and ns laser surface texturing of various materials, namely silicon, copper, conductive polymer films and a topological insulator. These materials have been selected as case study, as for Si or topological insulators, or because they are of particular interest for some specific applications. The features of the surface structures formed by laser irradiation where also analyzed in different experimental conditions, i.e. for static spots and large area processing according to the specific aims of the experiments.

For silicon, the study was mainly devoted to static and dynamic irradiation at various laser pulse repetition rates and to evidence differences between processing in air and in vacuum. The analysis was devoted to the features of both subwavelength ripples and suprawavelength grooves that are typically formed on silicon. One interesting result is the different dependence of the period of ripples and grooves on the effective pulse number evidencing that different mechanics are in place for these two structures besides the underlying influence of the electromagnetic effects. Another very interesting aspect is the influence of plume shielding, that is negligible in vacuum but becomes important in air at repetition rates larger than about 10 kHz. In conclusion, the absence of heat accumulation as well as the hindering of plume shielding in vacuum up to 200 kHz is particularly relevant, whereas irradiation in air should be limited to repetition rates below 10 kHz to avoid the latter effect.

For copper, the analysis was mainly focused on fs laser processing over large area with various laser parameters, such as the beam scanning velocity, hatch distance, ambient condition and laser wavelength. The differences in laser processing with laser beams focused by a spherical and a cylindrical lens on the features of the surface structures were investigated and discussed. The main findings were in the clear formation of ripples in both cases and a presence of a secondary long-range modulation with formation of shallow channels in the case of the spherical lens focusing. The results are of interest for application of copper structured surface, in particular in the frame of a collaboration aiming at elucidating the merits of copper surfaces decorated with fs LIPSS on secondary electron emission.

For the experiments on polymers, namely a semiconductor polymer PH3T and a fullerene derivative $PC_{71}BM$, the main goal was exploring the formation of ripples with a spatially varying orientation by using vector vortex beams. The experiments were carried out in the frame of a collaboration addressing first the results with ns laser pulse irradiation, that is mostly applied for such materials, showing very promising results. It will be completed in the future with results of fs laser irradiation and a comparison between the two regimes will be eventually achieved.

Finally, the formation of periodic ripples on topological insulator (Bi_2Te_3) induced by fs laser irradiation was investigated. The objective in this case is to clarify the process of fs LIPSS formation in material characterized by peculiar surface properties and not investigated yet. Our first experimental analysis evidenced striking features with ripples spatially localized in an annular region of the shallow crater formed on the material, which will deserve further experiments and theoretical interpretation of the mechanisms. Moreover, the width of the rippled annular region rises as a function of the laser pulse number but shows a negligible dependence on the peak fluence of laser.

In conclusion, in my thesis work the process of LIPSS formation in various experimental conditions and different materials of interest for fundamental studies and possible applications was investigated varying the processing parameters and addressing their role. The experimental findings provide a step forward in the assessment of the influence of the various experimental parameters (i.e. number of pulses, laser wavelength, ambient conditions, polarization state, processing configurations) in the various cases with the aim of increasing the understanding of the process of surface structures formation by fs laser irradiation. This, in turn, can provide useful insights for their use in tailoring the surface structures for specific applications.

Acknowledgments

It is great pleasure to express my sincere gratitude here to those who have provided help and kindness to my life and study.

First of all, I would like to sincerely thank **University of Naples Federico II** for giving me this opportunity to pursue my PhD degree, and also thank the **China Scholarship Council** for providing me with the scholarship.

The most important person to thank is my mentor and supervisor, **Prof. Salvatore Amoruso**, who is a man of great character, refinement and gentlemanly manner. He is very professional with our research, which I think benefits from his rich knowledge and talent. He writes and revises manuscripts very quickly, and with remarkable effect. Every time I got the revised manuscript from him, I make up my mind to write the next draft well and make it less revised, but it seems that I never succeed. He never criticized me, even if I made some mistakes sometimes. He would not strongly ask me to do something and give me a lot of space to learn freely. I always feel that I am a lucky person, and it is a strong proof of my luck that I can complete my PhD study under the guidance of Prof. Salvatore Amoruso.

The senior postdoc in our group, **Dr. Jijil JJ Nivas**, is my best friend in Naples, and I kept forcing him to admit that I am his best friend in Naples all the time. Oh, by the way, he has now become researcher at University of Naples Federico II. Since we met in 2017, he has helped me a lot in my life and work. Especially during my PhD from 2019 to 2022, as another supervisor of mine, he taught me a lot and let me know how to be a qualified PhD student.

Mr. Guido Celentano is the best PhD secretary I have ever met, and even the best words cannot describe how lovely he is. He changed my values: a job, if you put your heart into it, can be respected by everyone.

I also take this opportunity to thank **Prof. Domenico Paparo**, **Dr. Andrea Rubano** and **Dr. Sen Mou** for their support and help during my joint training. **Prof. Riccardo Bruzzese** is a professor who is about to retire. He often comes to my lab to see my research condition, and also helped me to read papers. Thanks for his attention and encouragement. **Dr. Alessia Sannino** in my office is a great beauty, warm and kind. She gave me my first New Year's gift in Italy, which made me feel the warmth of living in a foreign land.

In terms of courses, I would like to thank **Prof. Paolo Russo**, **Dr. Andrea Rubano**, **Dr. Antigone Marino**, **Prof. Salvatore Amoruso** and **Dr. Liliana Lisia** for providing me with high-quality courses, which allowed me to successfully obtain my credits and also learn a lot of knowledge and skills.

In terms of life, I would like to extend my thank to my landlord, **Mr. Salvatore Chiaiese**, for the stable house. He is fluent in English. I often call him when I go out and ask him to help me communicate with others. He helps me very patiently, although he also took me a lot of money.

Finally, I would like to express my special appreciation and thanks my daughter **QingQing**, for her thriving growth, no disease and no disaster, which allowed me to stay in Naples for three years without any worries to complete my PhD study. I would also like to thank my husband, **Mr. Qiucheng Yu**, for his support in my studies. He accompanied me all the way, patiently and gently.

Published articles

1. **Meilin Hu**, Jijil JJ Nivas, Rosalba Fittipaldi, Salvatore Amoruso. Femtosecond laser surface structuring of silicon in dynamic irradiation conditions. Optical Laser Technology. 156 (2022) 108594. https://doi.org/10.1016/j.optlastec.2022.108594.

2. **Meilin Hu**, Jijil JJ Nivas, Mohammadhassan Valadan, Rosalba Fittipaldi, Antonio Vecchione, Rriccardo Bruzzese, Caltucci Altucci, Salvatore Amoruso. Ultrafast laser surface irradiation of silicon: effects of repetition rate in vacuum and air. Applied Surface Science. (2022) 154869. https://doi.org/10.1016/j.apsusc.2022.154869.

Abbreviations

AFM	Atomic Force Microscope
CPA	Chirped Pulse Amplification
ET	Everhart - Thornley
fs	femtosecond
FFT	Fast Fourier Transform
FE-SEM	Field Emission Scanning Electron Microscope
HR	High Regular
HSFL	High Spatial Frequency LIPSS
IL	In-Lens
LIPSS	Laser induced periodic surface structures
LSFL	Low Spatial Frequency LIPSS
ns	nanosecond
OM	Optical Microscope
OFE	oxygen-free electronic grade
OFET	organic field-effect transistors
P3HT	poly(3-hexylthiophene)
$PC_{71}BM$	phenyl C71-butyric acid methyl ester
RR	repetition rate
RA	regenerative amplifier
SEM	Scanning Electron Microscopy
SEW	Surface Electromagnetic Wave
SPP	Surface Plasmon Polariton
SE	secondary electrons
SEY	Secondary Electron Yield
TI	topological insulator
UHV	ultra-high voltage
VVBs	vector vortex beams
2D	two-dimensional
2D-FFT	two-Dimension Fast Fourier Transform
2D-IFFT	two-Dimensional Inverse Fast Fourier Transform